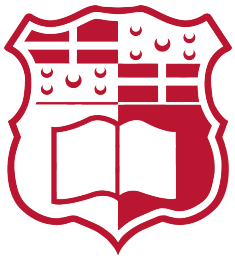

Testing New Physics with Precision Observations

Kathleen Sammut

Supervised by Prof Jackson Levi Said

Co-supervised by Dr Jurgen Mifsud

Institute of Space Sciences and Astrophysics

Faculty of Science

University of Malta

January, 2025

A dissertation submitted in partial fulfilment of the requirements for the degree of Master of Science in Space Sciences and Astronomy.

L-Università ta' Malta

WWW.UM.EDU.MT

First edition, March 10, 2025

The research work disclosed in this publication is partially funded by the Endeavour II Scholarships Scheme. The project may be co-funded by the ESF+ 2021-2027

Acknowledgements

I would like to express my deepest gratitude to all those who have supported me throughout this journey. My family and friends but most importantly, my partner Glenn Wallace, for his constant support and for always being there for me. For his patience, encouragement, motivation and for always believing in me.

Abstract

There are persisting tensions in the Hubble constant and in the σ_8 parameter that have yet to be resolved. Different models have been used throughout the years in an attempt to lessen these tensions and gain more knowledge about the Universe. ΛCDM is the theoretical framework that describes the origin, structure and evolution of the Universe. However, there are several tensions between the predictions of standard cosmology and the observations of various cosmological probes, such as the Hubble constant (H_0) and the σ_8 parameter. By investigating a reparametrisation of the ΛCDM, more information can be obtained on these tensions and new physics can be uncovered. The main objective of this research is to examine the viability of wCDM as a solution to the observed tensions within the standard cosmological model. The Cosmic Microwave Background (CMB) radiation, a powerful probe of the early universe, plays a central role in this study by analysing CMB anisotropies and temperature fluctuations in conjunction with high-precision data from Planck data. This project also takes the opportunity to examine the new Planck likelihood (Planck 2020) with the previous one (Planck 2018) and examine the new data of Dark Energy Spectroscopic Instrument (DESI) with the previously released data set of Baryon Acoustic Oscillations (BAO). The late-time data of Pantheon + SH0ES (SN+SH0ES) and Cosmic Chronometers (CC) data will also be used to serve as a way to add tighter constraints and, therefore, more accurate values with less uncertainties. In this project, the wCDM models showed that the newer datasets of Planck and BAO contained the models better than the previously released datasets. However, the wCDM model still favoured Planck 2018 and the older BAO data. Also, the tested models all had large uncertainties and degeneracies when only early-time data was taken, but the addition of the late-time data generally decreased the degeneracies and uncertainties. These key findings are discussed in further detail in Chapter 4.

Contents

List of Figures

List of Tables

1

Introduction

The ΛCDM model is taken as the standard model in cosmology [5, 33], where Λ [32] is the cosmological constant which results in an observable acceleration on large scales during the dark energy domination regime [89, 83]. CDM [19] refers to the cold dark matter which stabilises the structure of galaxies. This model was taken as the standard model due to the successes that it has in explaining the history and evolution of the Universe and explaining observational data. Some of the key successes of the ΛCDM model are that it can predict the temperature fluctuations in the CMB observed by missions like COBE [105], Planck [5, 110] and WMAP [17]. It predicts the Big Bang nucleosynthesis and the distribution of dark matter which is corroborated by the observation of gravitational lensing. Despite, these successes, there are still unresolved issues [82, 34] such as the true value of the Hubble constant (H_0) and this model also has a higher value of σ_8 than found in observational data.

H_0 essentially, represents the rate at which the Universe is expanding. When H_0 was calculated by different collaborations, the value was found to be inconsistent. Some of these collaborations include the SH0ES collaboration [90] which uses Cepheid variable stars and Type Ia supernovas [103] to measure distances in the Universe since they are considered to be standard candles. From these distance measurements, H_0 was determined as $73.2 \pm 1.3\ \mathrm{kms}^{-1}\mathrm{Mpc}^{-1}$. Another collaboration was the H0LiCOW collaboration [117] which used strong gravitational lensing to measure H_0. Gravitational lensing [116] is when a big astronomical object, such as a galaxy cluster, bends space-time to the point that light is visibly warped, as though through a lens. H0LiCOW used light from distant quasars which was bent by the gravity of an intervening galaxy. By measuring the time delays between multiple images of the quasar caused by the lensing effect, and knowing the mass distribution of the lensing galaxy, H_0 was estimated

as 67.4 ± 0.5 km s^{-1} Mpc^{-1}. TDCOSMO [118] is another collaboration that measured H_0 to be $67.4^{+4.1}_{-3.2}$ km s^{-1} Mpc^{-1}; this value was found by using a similar method to H0LiCOW of strong gravitational lensing and measuring the time delays. The disparity in the values of H_0 indicates an inconsistency [18, 35].

σ_8 refers to the quantity of density fluctuations in the matter distribution at a specific scale and is directly related to the cosmic web. This parameter can be inferred from the early universe, for instance from CMB observations and also from the late universe such as from weak lensing. Similar to the H_0 parameter, different values of σ_8 were obtained either late-time data or early-time data were used. Large-scale structure surveys such as KiDS [88] found slightly lower values of σ_8, around $0.75 - 0.80$ while higher values were found in the DESI survey [2] varying between $0.80 - 0.84$. Planck 2018 [5] obtained a value for σ_8 of 0.811 ± 0.006. The value of σ_8 is a reflection of the evolution of the primordial density perturbations meaning that larger values of σ_8 indicate stronger clustering and denser regions, while smaller values imply smoother distributions [84]. Therefore, this uncertainty with the value of this parameter signifies tensions that need to be resolved or at least lessened.

The equation of state parameter (w) is the ratio of the pressure and energy density. The value of w signifies the behaviour of dark energy so it directly influences H_0, and determines whether the expansion of the Universe is accelerating, decelerating or a constant. Hence, it determines the fate of the Universe. From the inclusion of Λ in the ΛCDM model, the standard model makes the assumption that $w = -1$ and that it is a constant throughout the history of the Universe.

To help solve the tensions that ΛCDM has with respect to H_0 and σ_8, a parameterization of extensions of ΛCDM can be tested. The wCDM model is an extension of the standard model [123, 101] where it defines w as a dynamical variable. By allowing w to vary, one accounts for the possibility of the emergence of phantom energy or it accounts for the possible deceleration of the expansion of the Universe [38]. It is also important to note that w also influences the dynamics and the geometry of the Universe, particularly its curvature. This idea has been explored by various cosmologists and researchers over the years. However, it became more prominent in the early 2000s when research emerged, increasing the possibility that wCDM could be a solution to the tensions [4, 15]. Over the years more research has been done on it, showing more and more evidence for this model [2, 42, 111]. The wCDM model can vary in its definition of w depending on the epoch of the Universe in question. For some variants of the wCDM model, there may be epochs where w does not vary, while other variants may have w varying for every epoch [123, 78].

Since wCDM is a reparametrisation of the ΛCDM [123], it does not affect the perturbation equations. However, w changes the values of the pressure, P, and density, ρ, of the Universe hence, it does affect the background equations. The background equations are important as they provide a foundational understanding of the Universe. They explain the homogeneous and isotropic expansion of the Universe depending on the model taken into consideration [37]. These equations incorporate the matter, radiation and dark energy, and energy densities and describe how each of them influences the Hubble constant [12, 111]. They also explain the state and evolution of the Universe from the Big Bang to current times.

Since the Universe is not homogeneous and isotropic on small scales, the perturbation equations account for the small deviations that are found in the Universe, which grow over time to form galaxies, clusters, and the cosmic web. These equations describe the evolution of small fluctuations found in the density, velocity and gravitational potential [37]. The wCDM model has the advantage of not changing the perturbations from the ΛCDM model. This is due to it being a reparametrisation of the standard model. This simplifies the calculations as no modifications need to be made regarding perturbations to test this model.

To be able to test the wCDM model, observational data is needed. Planck data will be used as well as 2D Baryonic Acoustic Oscillations data (BAO) [53], DESI 2024 (DESI) [2], Pantheon + SH0ES (SN+SH0ES) [99] and Cosmic Chronometers (CC) [43]. Planck data is Cosmic Microwave Background (CMB) radiation data obtained from the Planck telescope [26], which is the remnant radiation of the Big Bang and gives a snapshot of the Universe when it was only 380,000 years old. Both Planck 2018 (PR3) [5] and Planck 2020 (PR4) [110] will be used for the likelihood. This gives the opportunity to compare both likelihoods so that the recently released PR4 can be tested for any inconsistencies.

Local time data are added to the early time data as they help constrain the data and, therefore, should help achieve better results. The BAO data was chosen as it contains data on large-scale structures [53]. This data set involves analysing the angular distribution of galaxies and focuses on the angular separation of objects. A newer 2D BAO data was released from the Dark Energy Spectroscopic Instrument (DESI) [2] and this newer BAO was used to test the new likelihood and compare it to the previous BAO data. CC is a sample of 31 model-independent measurements and is primarily based on measurements of the age difference between two passively evolving [43]. SN+SH0ES on the other hand, is the combination of two separate sets of cosmological measurements that use Type Ia supernovae and Cepheid variables [90, 23], the latter being periodically pulsating stars.

To be able to get results from the wCDM model with the chosen data, a simulator to calculate the theoretical predictions of the model together with a simulator to plot the results are needed. Cosmic Linear Anisotropy Solving System (CLASS) [62] and MontePython [22] were used to generate corner plots using phenomenological dark energy models of wCDM and then compared to ΛCDM. For the computation of the theoretical predictions, CLASS was chosen [62]. This choice was due to the fact that it supports a wide range of cosmological models like the ΛCDM model, modified theories of gravity and reparametrisations of the ΛCDM model. Additionally, it is efficient as it is optimized for speed and accuracy, making it a powerful tool for large-scale parameter estimation.

After the theoretical predictions are computed, MontePython comes in to plot the results in the form of a corner plot so that they can be analysed. MontePython uses Monte Carlo Markov Chain (MCMC), specifically Metropolis-Hastings algorithm and Bayesian statistics to explore the parameter space of the given cosmological model, and derive constraints from the observational data [22]. The results produced are shown as corner plots by using GetDist. From MontePython, the parameters of the wCDM model can be estimated by comparing the theoretical prediction, in this case calculated by CLASS, with the observational data which in this case are the PR3, PR4, BAO, DESI, CC and SN+SH0ES. So, CLASS computes the theoretical predictions for the given parameter sets while MonthePython assesses the likelihood of these predictions given the observational data.

This dissertation will be divided as follows: Chapter 2 will go over the technical specifications of wCDM as well as introduce and explain the six different models of wCDM that were tested in this project, showing the calculations that were done for these models; Chapter 3 will go through simulations of CLASS and MontePython, the data sets that were used both early time data for the likelihoods and local time data used to help constrain parameters; Chapter 4 will discuss the results achieved from the six tested models of wCDM, the important findings and how they compare to the standard model; Finally, Chapter 5 will be a summary of the results and they are compared to past research.

2

wCDM parameterisation

In the late 1990s and early 2000s researchers were exploring the idea of a varying equation of state parameter, w, for a more dynamical form of dark energy [24] as a possible idea to solving the tensions found in cosmology. The wCDM model is an extension of the ΛCDM model. It incorporates a more general form of dark energy by a reparametrisation that moves away from a constant w to a dynamical one. The wCDM model can accommodate a wider range of dark energy behaviours, providing a better fit to observational data in some cases. This new model had reemerged as a response to quantifying deviations from the standard model. By adding more parameters, the model becomes more general when compared to the ΛCDM model since more parameters are taken into consideration. Therefore, it relaxes assumptions meaning that it removes some assumptions and parameterises them.

2.1 | ΛCDM

The ΛCDM model [37, 33] is the standard model in cosmology as it encapsulates the most comprehensive understanding of the Universe's structure, composition, and evolution. This model, which has a cosmological constant (Λ) [32], that represents dark energy, and Cold Dark Matter (CDM) [19], successfully explains a broad range of astronomical observations and underpins the theoretical framework of contemporary cosmology. It provides a cohesive explanation for the universe's large-scale structure, the anisotropies in the Cosmic Microwave Background (CMB) [109], and the observed accelerated expansion. By encompassing the essential components of dark energy, dark matter, baryonic matter, and radiation, the ΛCDM model serves as a comprehensive theory that aligns with both historical data and current observational evidence.

Despite its successes, the ΛCDM model faces challenges, particularly concerning the value of the Hubble constant (H_0) [18, 35]. The concept of the Hubble constant dates back to the 1920s with the work of Edwin Hubble and Georges Lemaître. There are disagreements in the value of H_0 that was calculated from early time data, such as CMB and BBN, and from late-time data. There are measurements from Planck 2018 that calculated $H_0 = 67.4 \pm 0.5$ kms^{-1}Mpc^{-1} [5], from ACT DR6 [87] which calculate H_0 as 68.3 ± 1.1 km s^{-1} Mpc^{-1}, from The TRGB collaboration [47] which uses measurements from the tip of the red giant stars and calculated H_0 to be 69.8 ± 0.8 kms^{-1}Mpc^{-1} and many more shown in Fig. 2.1.

Fig. 2.1 shows a whisker plot of the different values of H_0 found, measured both directly and indirectly throughout the years by many astronomical missions and collaborations. The light pink vertical band corresponds to the H_0 value published by Planck 2018 team [5] taking the ΛCDM model, while the cyan vertical band corresponds to the H_0 value from SH0ES Team [90] (R20, $H_0 = 73.2 \pm 1.3$ kms^{-1}Mpc^{-1}). The ΛCDM model and all other cosmological models describe the Universe, its history and its evolution using background and perturbation equations to describe the Universe's large-scale structure and its small-scale fluctuations.

2.1.1 | The Friedmann equations of the ΛCDM model

The background equations describe the Universe assuming that it is homogeneous and isotropic ignoring small-scale inhomogeneities. The ΛCDM model takes general relativity (GR) as its theory of gravity [37, 33]. Thus, to describe the dynamics of spacetime it uses the principle of least action given by,

$$S = S_{EH} + S_M \,, \tag{2.1}$$

where S_{EH} is the Einstein-Hilbert (EH) action [30, 102] which corresponds to the gravitational action, while S_M represents the matter action. The EH action describes the dynamics of the spacetime geometry as,

$$S_{EH} = \frac{1}{2\kappa^2} \int \mathring{R} \sqrt{-g} d^4x \,, \tag{2.2}$$

where g is the determinant of $g_{\mu\nu}$ which is the metric. This ensures that the integration is performed over the proper volume element in curved spacetime. The $\mathring{R}$ is the Ricci scalar and $\kappa^2 = 8\pi G c^{-4}$ where $c \equiv 1$. The matter action [37] is represented as,

$$S_M = \int \sqrt{-g} \mathcal{L} d^4x \tag{2.3}$$

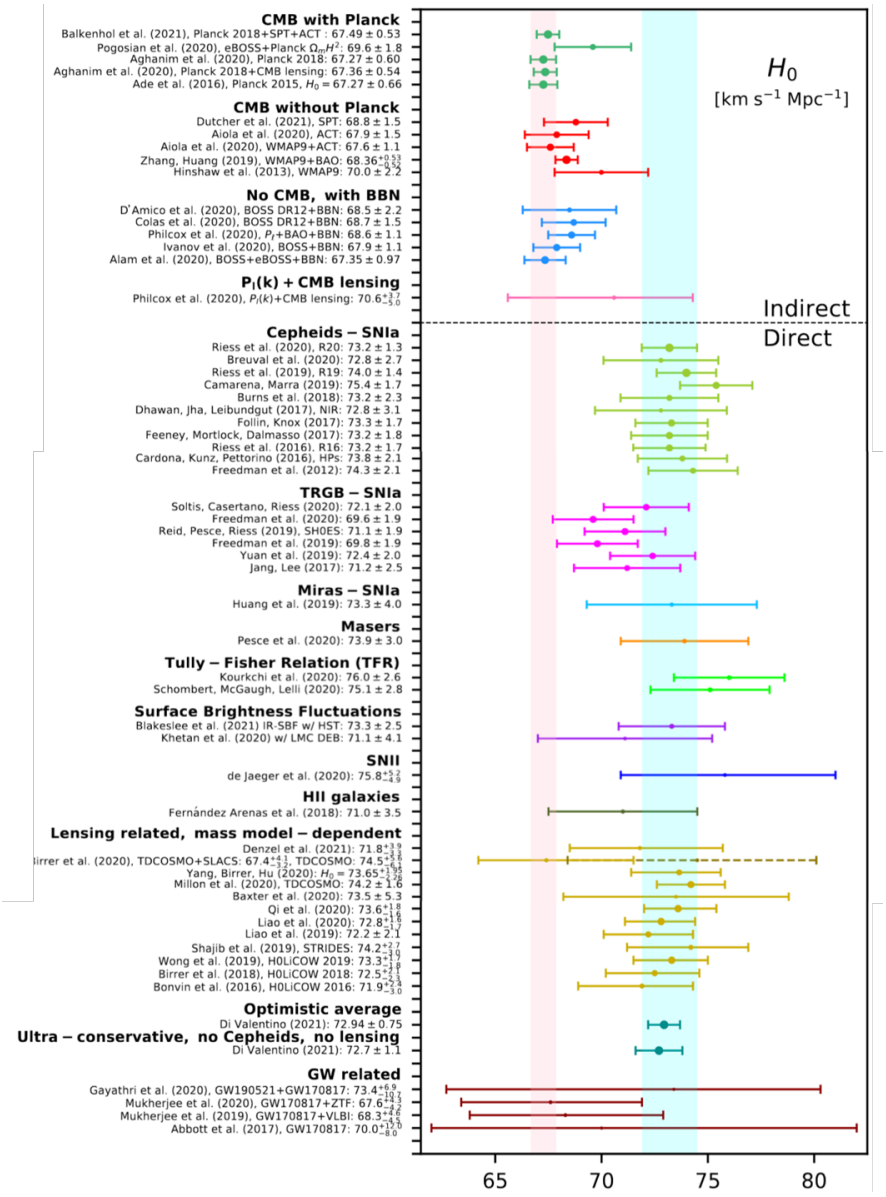

Figure 2.1: A Whisker plot [35] showing the inconsistencies with H_0 when using different measurements.

where $\mathcal{L}$ is the Lagrangian density. This term describes how matter and energy are distributed and how they interact with the gravitational field.

The cosmological principle states that on large scales, the Universe is homogeneous and isotropic. This allows the cosmos to be treated as a smooth fluid, ig-

noring small-scale inhomogeneities like galaxies and clusters of galaxies [10, 37]. This approach naturally leads to a fluid description, where macroscopic properties like temperature, pressure, and density are considered [25]. Thus for a perfect fluid, the stress-energy tensor is [95, 74, 69]

$$T_{\mu\nu} = (\rho + P)u_\mu u_\nu + P g_{\mu\nu} \,, \tag{2.4}$$

where u_μ and u_ν are the four-velocity of the fluid, ρ and P are the density and pressure of the fluid. The components of the stress-energy tensor describe how energy and momentum are distributed and how they flow through spacetime. The stress-energy tensor obeys the conservation laws given by the vanishing divergence

$$\nabla T_{\mu\nu} = 0 \,. \tag{2.5}$$

Eq. 2.5 represents the local conservation laws of energy and momentum in spacetime. It implies that the flow of energy and momentum is continuous and conserved. The Einstien-Hilbert action in Eq. 2.2 leads to the Einstien field equations which incorporates $T_{\mu\nu}$ [95, 60],

$$G_{\mu\nu} + \Lambda g_{\mu\nu} = 8\pi G T_{\mu\nu} \,, \tag{2.6}$$

where $G_{\mu\nu}$ is the Einstein tensor describing the curvature of spacetime, $g_{\mu\nu}$ is the metric tensor and it defines the distance between nearby points in spacetime. G is the gravitational constant and Λ is the cosmological constant. The Einstein's field equations, describe how matter and energy influence the curvature of spacetime which in turn dictates the gravitational field.

The equation of state (EoS) [123, 78] is a thermodynamic equation that relates the pressure, volume and mass of a fluid. The EoS for dark energy, w is defined by the equation,

$$w \equiv \frac{P}{\rho} \,, \tag{2.7}$$

where p is the pressure of the Universe and ρ represents the energy density of the Universe. The ΛCDM model assumes that w is constant and equal to -1 throughout the history of the Universe. This assumption is due to the model treating dark energy as a cosmological constant, Λ, representing a constant ρ filling space homogeneously while the expansion of the Universe is due to a negative P. This assumption suggests that the Universe is flat and will continue to expand at an accelerating rate indefinitely.

A metric is a mathematical framework used to describe the geometry of spacetime. It allows the ability to calculate the distances between two points in a manifold. The Friedmann-Lemaître-Robertson-Walker (FLRW) metric [36, 37] is a solution to Einstein's field equations and it has the general form, using spherical

coordinates, of

$$ds^2 = -c^2dt^2 + a(t)^2\left(\frac{dr^2}{1-kr^2} + r^2d\theta^2 + r^2\sin^2\theta d\phi^2\right) , \tag{2.8}$$

where ds^2 is the spacetime interval, c is the speed of light. For simplification of equations it is assumed that $c = 1$. This assumption is commonly made by researchers. t is the time coordinate measured by a comoving observer, r, θ and ϕ are the comoving spherical coordinates, and k is the curvature parameter. $a(t)$ is the cosmological scale factor, both are a function of the cosmological time where a is related to the redshift z, by the equation,

$$a = \frac{1}{1+z} . \tag{2.9}$$

As the Universe expands, the value of a increases and the wavelength of light from distant objects stretches, leading to an increase in redshift. The FLRW metric is a geometric description of spacetime by providing the framework of the geometry assuming that it is homogeneous and isotropic [25, 10]. The ΛCDM model assumes that the Universe is flat, hence, $k = 0$, which results in the FLRW metric to be

$$ds^2 = -dt^2 + a(t)^2\left(dr^2 + r^2d\theta^2 + r^2\sin^2\theta d\phi^2\right) . \tag{2.10}$$

In the Cartesian coordinate system, the FLRW metric becomes [36, 102],

$$ds^2 = -dt^2 + a^2(t)d\vec{x}^2 , \tag{2.11}$$

where $\vec{x}^2 = dx^2 + dy^2 + dz^2$. The flatness assumption that the standard model makes was later backed up by collaborations such as the Planck data [5, 110]. With the FLRW and Einstien's field equations, the equation that represents the dynamics of the Universe known as the first Friedmann equation can be derived,

$$H^2 = \frac{8\pi G}{3}\rho_i - \frac{k}{a^2} + \frac{\Lambda}{3} , \tag{2.12}$$

where H is the Hubble parameter $H = \frac{\dot{a}}{a}$, G is the gravitational constant and ρ_i is the total energy density. The Friedmann equation uses the framework of the FLRW metric [36] to determine how the Universe's scale factor changes over time essentially describing the evolution of the Universe. This means that Eq. 2.12, gives the history and evolution of the Universe as well as its future. In the case of the ΛCDM model, $k = 0$ due to the cosmological constant, Λ, and the energy density of a vacuum is defined as

$$\rho_\Lambda \equiv \frac{\Lambda}{8\pi G} . \tag{2.13}$$

The first Friedmann equation in the case of the ΛCDM model becomes

$$H^2 = \frac{8\pi G}{3}\rho_i \,. \tag{2.14}$$

The continuity equation is a key component of the Friedmann equations [102] as it is a manifestation of the principle of conservation of energy applied to an expanding Universe. It states that the change in energy density of a component within a comoving volume is due to the work done by or against the pressure as the volume changes. This can be derived from the first law of thermodynamics. The continuity equation can be expressed as [101, 60]

$$\dot{\rho}_i + 3H(\rho_i + P_i) = 0 \,, \tag{2.15}$$

where $\dot{\rho}$ is the time derivative of the energy density for each component of the Universe represented by i. The Universe is composed of several key components, each contributing to its overall energy density and dynamics. By solving the continuity equation for different components, it can be known how the energy densities of matter, radiation, and dark energy change over time. Depending on the component, the value of ρ changes. The cosmic fluid is composed of three elements: matter, radiation, and vacuum, each of which individually has a unique equation of state [101]:

$$\rho_i = \rho_m + \rho_r + \rho_\Lambda \,, \tag{2.16}$$

where ρ_m is the density of the matter component of the Universe, ρ_r is the density of radiation while ρ_Λ is the density of vacuum. There are different kinds of matter found in the Universe. There is the normal baryonic matter such as protons and electrons. However, there are non-baryonic dark matter, which interacts with the electromagnetic field only very weakly and is invisible. Additionally, the name of the various types of dark matter [69], such as cold dark matter (CDM) and hot dark matter (HDM), is related to whether or not the particles' characteristic energy is relativistic or not. The total matter density may be represented as the sum of the contributions from baryonic and dark matter [101]

$$\rho_m = \rho_b + \rho_{dm} \,, \tag{2.17}$$

where ρ_b and ρ_{dm} are the density of baryonic matter and dark matter respectively. Since the matter particles are assumed to have thermal energies that are significantly lower than their rest mass energies, the matter is pressureless (dust). Hence, the equation of state parameter in this instance is $w = 0$. By taking the present-day proper density of matter to be $\rho_m(t_0) \equiv \rho_{m_0}$, the density can be then expressed as [55]

$$\rho_m(a) = \rho_{m_o}(a)^{-3} \,, \tag{2.18}$$

Eq. (2.18) is consistent with how we anticipate the spatial density of dust particles to behave in an expanding Universe.

Radiation refers to photons as well as other species with very low or zero rest masses that travel relativistically in the present [13]. The total equivalent mass density of radiation in the cosmos at any cosmic time t may be expressed as the sum of the photon and neutrino contributions

$$\rho_r(t) = \rho_\gamma(t) + \rho_\nu(t) \,, \tag{2.19}$$

where ρ_γ and ρ_ν are the densities of photons and neutrinos respectively. In the case of radiation, w is taken to be $\frac{1}{3}$. If $\rho_r(t_0) \equiv \rho_{r_0}$, then the density of radiation can be written as

$$\rho_r(a) = \rho_{r_0}(a)^{-4} \,. \tag{2.20}$$

There is an additional factor of a^{-1} when Eq. (2.20) is compared to Eq. (2.18). This additional factor is due to the cosmic redshift of each photon. Neutrinos also experience redshifting as the universe expands, just like photons [37]. However, the effect of redshifting on neutrinos is much smaller compared to that on photons, because neutrinos have a much smaller interaction cross-section with matter, and hence they decouple from matter much earlier in the history of the universe. This means that ρ_ν changes very little during the later stages of the universe's expansion. So although ρ_ν also has a redshifting factor of $(1+z)$, the effect is much smaller than that for photons.

Therefore, the first Friedmann equation in Eq. 2.12 for the ΛCDM model becomes [37, 10]

$$H^2 = \frac{8\pi G}{3}\left[\rho_{r_0}a^{-4} + \rho_{m_0}a^{-3} + \rho_\Lambda\right] \,. \tag{2.21}$$

After the first Friedmann equation, Eq. 2.12 which relates the expansion rate of the Universe to its energy content, there is the second Friedmann equation which describes the acceleration (or deceleration) of the Universe's expansion. The second Friedmann equation [60, 69] is derived by combining the first Friedmann equation with the Einstein's Field equations in Eq. 2.6 and relates the second time derivative of the scale factor $a(t)$ to the energy density and pressure of the Universe's contents with the equation,

$$\frac{\ddot{a}}{a} = -\frac{4\pi G}{3}(\rho_i + 3P_i) \,, \tag{2.22}$$

for each component of the cosmos represented by i, $\ddot{a}$ is the second proper time derivative of the scale factor, a. Eq. 2.22 shows how the ρ and p influences the Universe's acceleration or deceleration.

2.1.2 | Perturbation Equations

In the Universe, the cosmological principle holds, but this starts to break down at lower scales. In the early Universe, because the cosmos was expanding rapidly, different regions of the universe were not able to "communicate" with each other. This communication refers to the exchange of information or interactions, which are limited to the speed of light. Due to this, there are anisotropies that need to be accounted for to obtain a complete description of the cosmos. These perturbations grow over time due to gravitational instability which leads to the formation of large-scale structures. Before inflation, the Universe had small fluctuations but when inflation happened, these fluctuations were stretched out to macroscopic scales making the once small fluctuations now significant. As the Universe expanded, these fluctuations grew and eventually crossed the cosmological horizon. As soon as they crossed the horizon, these fluctuations stopped evolving and became fixed [37]. These 'frozen' fluctuations manifested in density perturbations. Regions with higher densities attracted more matter due to gravity, which led to the formation of galaxies as well as galaxy clusters. After inflation ended, the Universe still continued to expand, but at a slower rate. The perturbations that had crossed the horizon during inflation eventually re-entered the horizon. There are different types of perturbations; scalar perturbations, vector perturbations and tensor perturbations [51].

The scalar perturbations are connected to the matter fluctuations. These are a type of fluctuation in the density of the cosmological fluid; they play an important role when it comes to the understanding of the formation of the large-scale structure of the cosmos [10]. Since the Universe is taken to be a fluid, scalar perturbations can be thought of as small ripples in this fluid that are a result of the differences in the density of matter and energy at different points in space. Furthermore, the scalar perturbations represent the density fluctuations that lead to gravitational potential wells, and because of gravitational instabilities, this type of perturbations grow over time, which is the reason why they impact the formation of structures in the cosmos. These perturbations influenced the distribution of matter and radiation in the Universe, leading to the anisotropies observed in the CMB.

In perturbation theory, the two commonly used gauges are: the Newtonian gauge and the synchronous gauge. [51] Gauges refer to different choices of coordinate systems or reference frames [69]. They help simplify the equations of perturbations, making them easier to solve. In the Newtonian gauge, the observer is attached to the unperturbed frame, resulting in two potentials in the scalar perturbations. Thus, the metric of the scalar perturbations in the Newtonian gauge

[74, 25] can be written as

$$ds^2 = -(1+2\Psi)dt^2 + a^2(t)(1-2\Phi)\delta_{ij}dx^i dx^j \,, \tag{2.23}$$

where δ_{ij} is the Kronecker delta which represents the unperturbed spatial part of the metric indicating a flat, homogeneous, and isotropic Universe, Ψ is the gravitational potential and Φ is the curvature perturbation. In the absence of Φ and Ψ, Eq. 2.23 simplifies to the FLRW metric seen in Eq. 2.11.

Since scalar perturbations involve density and gravitational potential variations, w affects these fluctuations as it affects the growth rate of the density fluctuations. If $w = -1$, which is the assumption that the ΛCDM model makes, the growth of the density perturbations remains constant, meaning that the accelerated expansion suppresses the growth of the perturbations. When $w = 0$, which applies to a matter-dominated era, density perturbations grow linearly with respect to a. This is because pressure is negligible, and gravity drives the growth of density fluctuations. However, if $w > -1$, the rapid acceleration driven by phantom energy leads to a strong suppression of the growth of scalar perturbations. The expansion rate becomes so significant that density perturbations are stretched apart, preventing them from growing. For $-1 < w < 0$, the growth of perturbations is suppressed, but structure formation still occurs, while for $w > 0$ the growth of perturbations is suppressed by the fluid's pressure. During radiation radiation-dominated era ($w = \frac{1}{3}$), the growth of perturbations is suppressed due to the pressure of radiation, leading to oscillations and damping.

Due to the fact that they decay quickly in the early Universe, vector perturbations are less significant when it comes to structure formation. However, they still affect the dynamics of the Universe. Vector perturbations are associated with the rotational or vortical motion of the fluid. They describe how different parts of the fluid move relative to each other in a rotational manner. These perturbations can also be related to shear stress in the fluid [37], which is a measure of how different layers of the fluid slide past each other. The dissipation of these perturbations happens due to the expansion of the Universe during inflation, stretching out the rotational motion resulting in these perturbations becoming less significant towards the late Universe. The metric of the vector perturbations [51] in the Newtonian gauge is represented as,

$$ds^2 = a^2(t)[-dt^2 + (\delta_{ij} + F_{i,j} + F_{j,i})dx^i dx^j] \,, \tag{2.24}$$

where F_i represents the vector perturbation. Vector perturbations rapidly decay after inflation to the point that they do not affect the formation or evolution of the Universe. Thus, the value of w does not affect this type of fluctuations, and so they are not considered for this project.

The tensor perturbations are related to inflation and primordial gravitational waves. Tensor perturbations unlike the other previously mentioned perturbations, are purely geometrical and represent ripples in the fabric of spacetime itself [37]. These are ripples in spacetime that propagate at the speed of light, generated by accelerating masses, such as merging black holes or neutron stars. Tensor perturbations propagate freely through the cosmos without being affected by the matter content. This makes them good probes of the early Universe, as they carry information from the inflationary period to the present day. Tensor perturbations leave an imprint on the polarization of the CMB as they are responsible for the B-mode polarization [10]:

$$\ddot{h}_{ij} + 3H\dot{h}_{ij} + \frac{k^2}{a^2}h_{ij} = 0\,, \tag{2.25}$$

where h_{ij} are the components of the tensor perturbation. Eq. 2.25 describes the propagation and damping of gravitational waves in an expanding Universe. The metric of this type of perturbations in the Newtonian gauge is given by [49]

$$ds^2 = a^2(t)[-dt^2 + (\delta_{ij} + h_{ij})dx^i dx^j]\,. \tag{2.26}$$

Gravitational waves propagate independently of matter content. For this project the tensor perturbations will not be considered.

2.1.3 | ΛCDM parameters

The Cosmic Microwave Background Radiation (CMB) refers to a type of electromagnetic radiation that is a remnant of the Big Bang, and this fills the entire observable Universe. The CMB offers a unique window into the early Universe, providing a snapshot of when the Universe was just 380000 years old [109], when photons decoupled from matter and were able to travel freely through space. This radiation contains information about the structure of the primordial cosmos and the physical conditions.

In Fourier space, a power spectrum is any real quadratic function of a perturbation variable [10]. A more general description of a power spectrum would be that it is a graphical representation of the distribution of a signal's power when taking into account different frequencies. Since the power spectrum measures the amplitude of fluctuations as a function of their spatial scale or wavelength, it enables us to interpret information about these fluctuations.

First, it is good to note that any function on the surface of a sphere can be written as a sum over complex functions. This can be seen in the following equation [75]:

$$\Theta(\mathbf{x}, \hat{\mathbf{p}}, \eta) = \sum_{l=1}^{\infty} \sum_{m=-l}^{l} a_{lm}(\mathbf{x}, \eta) Y_{lm}(\hat{\mathbf{p}}) \tag{2.27}$$

where $T(\theta, \phi)$ represents the surface of the sphere, $Y_{lm}(\theta, \phi)$ is the spherical harmonics, a_{lm} is the amplitude, l represents the wavelength of the oscillations i.e. it is the number of poles, and m is the multipole moment which ranges from $-l$ to l.

The purpose of a cosmological model, in general, is not to predict the temperature of the CMB in a particular direction, or the value for any given a_{lm}. In fact, they actually predict properties of a more statistical nature such as the mean and variance of those coefficients, which can take on predictable values given certain cosmologies. For example, isotropic ones lead to the mean of every a_{lm} except for the monopole to be zero. As for the variance, it is independent of m in isotropic theories and is given by [37]

$$C(l) = \langle a_{lm} a_{lm}^{*} \rangle \ , \tag{2.28}$$

Incidentally, this function of l is what is referred to as the "power spectrum". The distribution of the CMB's anisotropies have frequency components which can be represented by a power spectrum displaying a sequence of peaks and valleys. These peaks hold valuable information regarding the physical properties of the Universe.

Fig. 2.2 is a visual view of the CMB power spectrum. The curve shows the theoretical power spectrum while the points show the data from the Planck 2018 collaboration [5]. The angle θ has a relation with the multipole l represented as $\theta = \frac{\pi}{l}$. The first peak seen in Fig. 2.2 determines the overall curvature of the Universe, which is consistent with a flat Universe [29]. The second and third peaks represent the density of normal matter and dark matter respectively as well as give information on the baryonic acoustic oscillations that occurred in the early Universe.

The fluctuations in the density of baryonic matter have a direct impact on the prominence of the peaks [29]. When there is a high concentration of baryonic matter, the odd-numbered peaks tend to be more pronounced than the even-numbered ones. This is a consequence of the decreased oscillation frequency brought about by the substantial baryons. As a result, one of the most straightforward parameters to determine from the CMB is the density of baryonic matter

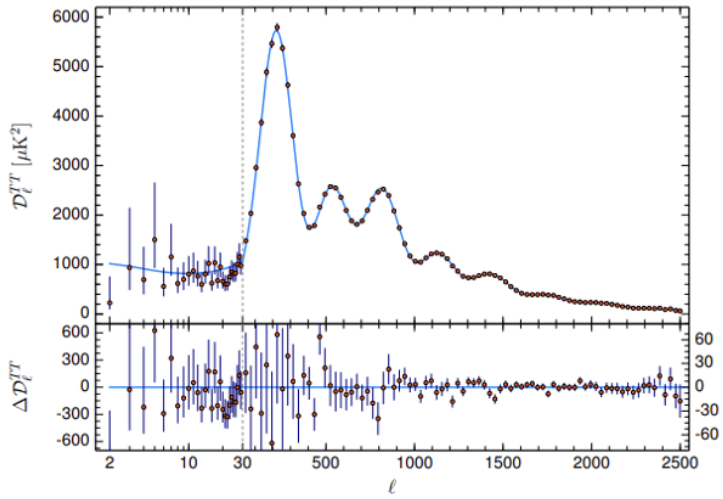

Figure 2.2: The CMB power spectrum; $\frac{l(l+1)C_l}{2\pi}$ versus the angular size and the multipole moment l where the curve shows the theoretical prediction while the points are the data obtained from the Planck 2018. Retrieved from the Planck 2018 paper [5].

[37]. It is also important to note that changes in the baryon density lead to a shift in the locations of the peaks, due to the corresponding change in the sound horizon. Additionally, these changes also result in changes in the peak heights.

The ISW is accountable for the low multiples in the CMB power spectrum [101]. This is due to the decrease in the gravitational potential when the Universe transitions from the standard matter era to an accelerated epoch, as predicted by the ΛCDM model [10].

In order to constrain the CMB power spectrum, certain parameters need to be chosen in such a way that impacts the state of the power spectrum. The ΛCDM model takes specifically six parameters which are w_{cdm}, w_b, θ_s, τ_{reio}, A_s and n_s. These parameters are chosen because they effectively capture the essential state of the early universe and its evolution which can then be extended to give information on the late Universe. The advantage of only having six parameters is that it gives enough information on the early Universe yet at the same time it simplifies simulations [37]. Other parameters can be considered though issues with degeneracies can occur between parameters, and moreover, adding more parameters can run into problems with simulations not being able to differentiate between each one.

The parameter w_{CDM} is the physical energy density in CDM and is represented by the equation,

$$w_{cdm} = h^2 \Omega_{cdm}, \tag{2.29}$$

where $h = \frac{H_0}{100}$ is the reduced Hubble constant and Ω_{cdm} represents the density parameter for cold dark matter [109]. The parameter w_b is the physical energy density in baryons and is described by the equation,

$$w_b = h^2 \Omega_b \, , \tag{2.30}$$

where Ω_b is the density parameter for baryonic matter. It is the fraction of the total energy density of the universe that is made up of baryons, which are particles such as protons and neutrons that make up ordinary matter. The parameters w_{cdm} and w_b play a role in the CMB's power spectrum, they influence the heights and positions of the acoustic peaks. Baryons affect the amplitude of the peaks, while cold dark matter affects the overall shape and position.

θ_s is the angular size of the sound horizon and represents the maximum distance that sound waves could travel in the early universe before the photons decoupled from matter that occurred in the time of last scattering [109]. This can be calculated from the distance from the angular size of 90° till the first peak in Fig. 2.2. From θ_s, knowledge can be retrieved about the geometry and the expansion rate of the Universe as the parameter can be taken as a standard ruler for measuring distances in the cosmos.

τ_{reio} is the optical depth to reionization, it quantifies the amount of scattering that CMB photons experienced due to free electrons released during the epoch of reionization. The primary effect of τ_{reio} in the CMB power spectrum is that it dampens small-scale fluctuations [37]. This happens because the reionization process re-scatters CMB photons, which smooths out the temperature fluctuations on small angular scales. Reionization also enhances the polarization signal on large scales. This is because the re-scattering of CMB photons during reionization generates additional polarization, which is observed as an increase in the large-scale E-mode polarization power spectrum. The value of τ_{reio} affects the normalization of the matter power spectrum. A higher optical depth implies more reionization, which in turn affects the amplitude of fluctuations observed today.

A_s is the amplitude of the primordial scalar perturbations. With respect to Fig. 2.2 it is the amplitude of the primordial power spectrum which is the amplitude of the first peak, as it measures the initial amplitude of the density fluctuations in the Early Universe. The value of A_s directly influences the growth of structures in

the Universe. Higher values of A_s lead to more pronounced density fluctuations, which in turn lead to more efficient formation of galaxies and clusters.

The final parameter of the ΛCDM is n_s. This parameter refers to the spectral index of the primordial scalar perturbations, which is the distribution of the primordial density fluctuations across different scales. It thus, affects the "tilt" of the primordial power spectrum. The n_s parameter is crucial during the period of inflation as it provides information about the energy scale at which inflation occurred.

These six parameters are enough to constrain the CMB power spectrum curve. However, due to the tensions found in the H_0 and σ_8 parameters, other parameters besides the six ΛCDM parameters can be added in hopes of constraining the power spectrum curve in a way that could lessen these tensions when the early Universe is extended to the late Universe. Models that add more parameters are essentially a relaxation of the assumptions that are taken in that standard model of cosmology as it generalises the ΛCDM model even more.

2.2 | wCDM

The wCDM model is an extension of the standard cosmological, ΛCDM, since it is a reparameterization of it [120, 2]. The wCDM model, unlike the ΛCDM model, does not assume that $w = -1$, and focusses on the idea that the true value of the equation of state of dark energy could actually be different from what the standard model takes it to be. By finding the true value of w a better model can be obtained and could lessen the pressing tensions in cosmology. This idea has been explored by various cosmologists and researchers over the years. This model became more prominent in the early 2000s when significant research emerged, increasing the possibility that wCDM could be a solution to the tensions [4, 15]. One of the notable and early contributors to the development and exploration of the wCDM model is John D. Barrow [70, 73].

If w is different from -1, then from the definition of w in Eq. 2.7, the amount of how much ρ and P are proportional to each other will be different from the ΛCDM model. In the cases where the assumption of w being constant is also removed and it is let to vary, then the rate at which ρ and P are proportional to also changes over time. The value of w helps determine the behaviour of the Universe regarding the pressure and energy density. In fact, it is often used to characterize the nature of dark energy [37]. There are three scenarios of w and they all have a different description of the Universe.

When $w < -1$, the curvature is negative, implying an open Universe, leading to a highly accelerated expansion of the Universe and is known as phantom energy. Phantom energy is when dark energy is highly dominating and so the acceleration of the Universe accelerates so much that there will be a big rip.

In the case of $w > -1$, dark energy becomes less dominant as the Universe expands, resulting in a deceleration of the expansion. It also means that the curvature is positive, leading to a closed Universe.

Many observational data such as distant supernovae measurements like SH0ES [90], CMB observations such as Planck [5, 110] and other measurements from COBE [105] and WMAP [17] all show that the Universe is experiencing an accelerating expansion. This results in considering a negative pressure component at late times [42]. Substituting Eq. 2.7 into the second Friedmann equation Eq. 2.22, gives

$$\frac{\ddot{a}}{a} = -\frac{4\pi\rho G}{3}(1+3w)\,, \tag{2.31}$$

Thus in order to have an accelerated cosmic expansion, at late times the pressure is negative, and adding to the fact that energy is always positive it is required that to satisfy those conditions, $\frac{\ddot{a}}{a} > 0$ [42] and $\Lambda = 0$. Knowing this, Eq. 2.31 becomes

$$-\frac{4\pi\rho G}{3}(1+3w) < 0\,, \tag{2.32}$$

$$w < -\frac{1}{3}\,. \tag{2.33}$$

Therefore, for an accelerated expansion, at late times it is required that $w < -\frac{1}{3}$. This is taken as a constraint in this project. Since in the wCDM model w is now time-dependent, this change also impacts the second Friedmann equation as shown in Eq. 2.31 and introduces more complexity to the equation, as now w impacts the acceleration rate of the cosmos. Allowing for more flexibility and is capable of achieving a more accurate value of the second Friedmann equation.

The evolution of the energy density is governed by the fluid equation and can be derived from the equation of the conservation of energy, Eq. 2.15. In the case where w is time-dependent, Eq. 2.7 needs to be substituted into Eq. 2.15 for it to be then integrated [123].

$$\dot{\rho}_i + 3H(\rho_i + P_i) = 0 \tag{2.34}$$

$$\dot{\rho}_i + 3H(\rho_i + \rho_i w_i) = 0 \tag{2.35}$$

$$\dot{\rho}_i + 3\rho_i H(1+w_i) = 0\,. \tag{2.36}$$

Substituting the equations $H = \frac{\dot{a}}{a}$, and then rewriting the Eq. 2.36 the equation becomes

$$\frac{\dot{\rho}_i}{\rho_i} = -3(1+w_i)\frac{\dot{a}}{a}\,. \tag{2.37}$$

Then, integration with respect to t is done to get the time-dependent equation of $\rho(a)$ [37],

$$\int \frac{\dot{\rho}_i}{\rho_i}dt = \int -3(1+w_i)\frac{\dot{a}}{a}dt\,, \tag{2.38}$$

$$\int \frac{d\rho_i}{\rho_i} = \int -\frac{3(1-w_i)}{a}da\,, \tag{2.39}$$

$$\ln(\rho_i) = \int -\frac{3(1-w_i)}{a}da\,, \tag{2.40}$$

$$\rho(a) \propto \exp\left[-\int_a^{a_0} 3\frac{1+w(a)}{a}da\right]\,, \tag{2.41}$$

where a_0 is the scale factor at current times. The time-dependent density helps in the understanding of how the density of the Universe evolves over time which is important for the construction of cosmological models and then comparing its theoretical predictions with observational data. For the ΛCDM model, $w(a) = -1$ thus, the expression in Eq. 2.41 reduces to $\rho(a) \propto 1$ [42]. Eq. 2.41 is then added to Eq. 2.12 to have a complete first Friedmann equation for the wCDM model.

$$\begin{aligned} H^2 &= \frac{8\pi G}{3}\left[\rho_{r0}a^{-4} + \rho_{m0}a^{-3}\right] \\ &+ \frac{8\pi G}{3}\left[\rho_{DE}\exp\left[-\int_a^{a_0} 3\frac{1+w(a)}{a}da\right]\right]\,. \end{aligned} \tag{2.42}$$

This means that no matter what the dark energy equation of state, w, a model has, the Hubble rate can be found with Eq. 2.42. Consequently, the term $\int_a^{a_0} 3\frac{1+w(a)}{a}da$ in Eq. 2.41 would need to be calculated for each version of w for each model of wCDM in order to know how $\rho(a)$ varies over time and also for the Friedmann equation to be calculated.

Since the wCDM model is an extension of reparametrisation of the ΛCDM model, it does not affect the general form of the perturbation equations but this does not mean that it does not affect them indirectly. The value of w and how it varies affects the relationship between ρ_{DE} and P, thus affecting the density fluctuations, especially since the growth rate of cosmic structures is sensitive to the value of w. A different time-dependent w changes the rate at which perturbations grow over time. Changes in the density perturbation lead to a different prediction of the CMB and the large-scale structure of the Universe [9].

The impact of w on the perturbation can be more clearly seen by exploring the perturbation equations of a general dark energy scenario by using the synchronous gauge instead of the Newtonian gauge. In the synchronous gauge, the position of the observer is chosen such that the time coordinate is synchronized with the proper time of the comoving observers [74, 25]. This results in the metric perturbations not affecting the time-time component and the time-space components of the metric. The synchronous gauge is chosen since the specific choice of coordinates simplifies the equations by setting certain components of the metric perturbations to zero. Therefore, the general perturbed FLWR metric [120] in the synchronous gauge is in the form of

$$ds^2 = a^2(\tau)[-d\tau^2 + (\delta_{ij} + h_{ij})dx^i dx^j] \,, \tag{2.43}$$

where τ is the conformal time, h_{ij} and δ_{ij} are respectively the perturbed and unperturbed metric, which can include scalar, vector, and tensor components. The Euler equations help in understanding how small initial perturbations in the density of the Universe grow over time. Since the Universe can be considered as a fluid, then the Euler equation can describe the dynamics of these fluids, including their motion and interaction under the influence of gravity. Understanding these dynamics is essential for predicting how structures in the Universe evolve over time.

In the synchronous gauge, the continuity and Euler equations can also be obtained as [78, 69, 51],

$$\begin{aligned} \delta_i' &= -(1+w_i)\left(\theta_i + \frac{h'}{2}\right) - 3\mathcal{H}\left(c_s^2 - w_i\right)\delta_i \\ &- 9\mathcal{H}^2\left(\frac{\delta P_i}{\delta\rho_i} - c_{a,i}^2\right)(1+w_i)\frac{\theta_i}{k^2} \,, \end{aligned} \tag{2.44}$$

$$\theta'_i = -\mathcal{H}\left(1 - 3\frac{\delta P_i}{\delta\rho_i}\right)\theta_i + \frac{\delta P_i}{\delta\rho_i}\frac{1}{1-w_i}k^2\delta_i - k^2\sigma_i \,. \tag{2.45}$$

In Eq. 2.44 and Eq. 2.45, the prime denotes differentiation with respect to the conformal time $\tau = \int \frac{dt}{a(t)}$. The density perturbation is represented by $\delta_i = \frac{\delta\rho_i}{\rho_i}$, the conformal Hubble parameter is represented as $\mathcal{H} = \frac{a'}{a}$, $h = h_{ij}$ is the trace of the metric perturbations h_{ij}, the divergence of the i-th fluid velocity is denoted by $\theta_i \equiv ik^j v_j$, c_s^2 is the sound speed for an imperfect fluid and it is defined as $c_s^2 \equiv \frac{\delta P_i}{\delta\rho_i}$, σ_i is the anisotropic stress of the fluid, which will be neglected in the analysis and $c_{a,i}^2$ is the adiabatic speed of sound [74].

In early times, the Universe was a hot plasma of photons, electrons and baryons. The interaction between photons and baryons created pressure waves, known

as acoustic oscillations. These pressure waves affected the distribution of matter. Regions with higher density attract more matter due to gravity, leading to clumping. However, the pressure waves can counteract this gravitational pull. The balance between gravitational attraction and pressure support determines the growth of these density perturbations.

The adiabatic sound speed [37] in a fluid is a measure of how fast pressure disturbances propagate through the fluid when the process is adiabatic. It determines the rate at which pressure waves travel through the fluid. It influences the balance between gravitational forces and pressure forces, affecting how matter clumps together to form large-scale structures. The adiabatic speed of sound for the i-th fluid is defined as,

$$c_{a,i}^2 \equiv \frac{\dot{P}_i}{\dot{\rho}_i} \,. \tag{2.46}$$

Knowing this definition, together with the continuity equation in Eq. 2.44 and the Euler equation in Eq. 2.45, $c_{a,i}^2$ can be related to w_i with the equation [78],

$$c_{a,i}^2 = w_i - \frac{w_i'}{3\mathcal{H}(1+w_i)} \,. \tag{2.47}$$

The speed of sound is a key factor in determining the stability of a fluid. For instance, if perturbations grow too quickly relative to the speed of sound, it can lead to instabilities that influence structure formation. Eq. 2.47 can be arranged as shown below,

$$c_{a,i}^2 = w_i - \frac{a\frac{dw_i}{d\tau}}{3\frac{da}{d\tau}(1+w_i)} \,, \tag{2.48}$$

$$= w_i - \frac{a}{3(1+w_i)}\frac{dw_i}{da} \,. \tag{2.49}$$

Thus, for every wCDM parameterization model, the differentiation of w with respect to a needs to be calculated for each one. Therefore, the value $c_{a,i}^2$ can be obtained and hence, the predicted perturbations for each parameterization can be known.

For this project, six models are going to be considered; w_0CDM, CPL, JPB, GE, BA, and OSCILL. These chosen models are generalised and are restricted to mostly two free parameters because a large number of parameters is generally likely to lead to degeneracy amongst them [78]. Also, each model was taken from literature and was chosen due to evidence towards the possibility of these models lessening the tensions in cosmology.

2.2.1 | Constant model

Recent advancements in machine learning and their applications have been made. Neural networks [124, 113] is a modern and popular technique that is being used for estimating cosmological parameters and is being utilized more frequently to examine dynamical dark energy models such as quintessence [11, 80]. Despite the advancements neural networks brings, it is computationally intensive [96], which is the reason why neural networks were not used in this project.

The simplest form of generalisation of the ΛCDM model is w_0CDM model which still assumes that w is constant but it removes the assumption that $w = -1$. This is the first step to delve into reparametrisation or w. It is a basic model as it allows for the possibility for the additional parameter to be different than one, yet it is still taken to be a constant throughout the evolution of the Universe like the ΛCDM model [123].

$$w_{w0CDM}(a) = w_{0,w0CDM}\,, \tag{2.50}$$

where $w_{0,w0CDM}$ is the equation of state parameter at current times for the wCDM model. The parameter $w_{0,w0CDM}$ is taken instead of w_{w0CDM} to keep similarities with the rest of the parameterizations. When $w_{0,w0CDM} = -1$, the w_0CDM parametrisation reduces to the ΛCDM model.

Fig. 2.3 shows how the w_0CDM parameterization describes w as a constant parameter throughout the history of the Universe. The value of $w_{0,w0CDM}$ was taken as -1.046 while the shaded red area represents the 1σ variation taken as $1\sigma = ^{+0.024}_{-0.024}$ where both of which are results obtained that will be discussed further in Chapter 4.

Since wCDM models affect the background and perturbation equations as seen in this chapter, the first Friedmann equation shown in Eq. 2.12 as well as the adiabatic speed sound, $c_{a,i}$ shown in Eq. 2.47 need to be retrieved for each parametrisation. Thus integration is needed for the Friedmann equation by evaluating the term $3\int_a^{a_0} \frac{(1+w(a))}{a} da$, and differentiation of $w(a)$ with respect to a is needed for $c_{a,i}$ to be calculated, where $w(a)$ of this model is given in Eq. 2.50. Starting with integration for the background equation,

$$\int_a^{a_0} \frac{3(1+w_{w0CDM}(a))}{a} da = \int_a^{a_0} \frac{3(1+w_{0,w0CDM})}{a} da\,, \tag{2.51}$$

$$= 3(1+w_{0,w0CDM}) \ln(a)\Big|_a^{a_0}\,. \tag{2.52}$$

Since a_0 is the value of the scale factor at current times and taking into consideration the definition of a in Eq. 2.9, $a_0 = 1$ due to $z = 0$ at current times. Hence,

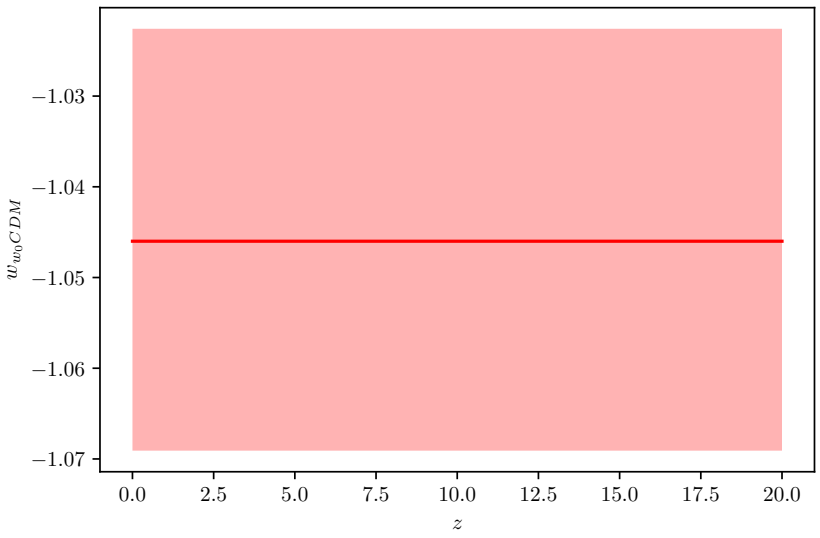

Figure 2.3: A graph showing how w varies with the redshift, z, for the w_0CDM parameterization. The red line is the equation of w_{w0CDM} when using the result of $w_{0,w0CDM}$ from Chapter 4. The light red shade represents the 1σ variation.

knowing that $a_0 = 1$, Eq. 2.52 becomes:

$$\begin{aligned}\int_a^{a_0} \frac{3(1+w_{w0CDM}(a))}{a} da &= 3(1+w_{0,w0CDM})\ln(1) \\ &- 3(1+w_{0,w0CDM})\ln(a)\,, \qquad (2.53)\\ &= 3(1+w_{0,w0CDM})\ln\left(\frac{1}{a}\right)\,. \qquad (2.54)\end{aligned}$$

Subsequently, the evaluated term in Eq. 2.54 was added to the first Friedmann equation in Eq. 2.42 and so the Friedmann equation for the w_0CDM parameterization is,

$$\begin{aligned}H^2 &= \frac{8\pi G}{3}\left[\rho_{r0}a^{-4} + \rho_{m_0}a^{-3}\right] \\ &+ \frac{8\pi G}{3}\left[\rho_{DE}\exp\left[-3(1+w_{0,w0CDM})\ln\left(\frac{1}{a}\right)\right]\right]\,, \qquad (2.55)\\ &= \frac{8\pi G}{3}\left[\rho_{r_0}a^{-4} + \rho_{m_0}a^{-3} + \rho_{DE}\left[a^{3(1+w_{0,w0CDM})}\right]\right]\,. \qquad (2.56)\end{aligned}$$

Now, moving to differentiating Eq. 2.50 with respect to a to obtain the adiabatic

sound speed, $c_{a,i}$ that was previously discussed in Eq. 2.47,

$$\frac{dw_{w0CDM}(a)}{da} = \frac{dw_{0,w0CDM}}{da}\,, \tag{2.57}$$

$$= 0\,. \tag{2.58}$$

Therefore, after substituting Eq. 2.58 into the equation of the adiabatic speed sound shown in Eq. 2.47, the equation of $c^2_{a,i}$ for the w_0CDM model becomes

$$c^2_{a,w0CDM} = w_{w0CDM}\,. \tag{2.59}$$

Therefore, the adiabatic speed sound of the w_0CDM is constant. From Eq. 2.59, the perturbation equations for the w_0CDM parameterization can be known. By now knowing the Friedmann and perturbation equations of w_0CDM, results can be retrieved from it by the help of simulations.

2.2.2 | Linear model

The Chevallier Polarski Linder (CPL) parameterization was first introduced by Chevallier and Polarski in 2001 then was later expanded by Linder in 2003 [66]. This parameterization generalises the ΛCDM model even more than the w_0CDM parameterization by incorporating dynamical features by taking w to be time-dependent instead of being constant, giving the freedom to reconstruct the expansion history of the Universe with observational data. moving away from the concept that w is constant by allowing it to vary throughout the evolution of the Universe [94]. This is done by using two parameters instead of one, allowing for a smooth transition of the dark energy equation of state parameter from the present value, $w_{0,CPL}$ to a different value in the past, controlled by $w_{a,CPL}$ [42, 123, 66] as seen below,

$$w_{CPL}(a) = w_{0,CPL} + w_{a,CPL}(1-a)\,, \tag{2.60}$$

When $w_{0,CPL} = -1$ and $w_{a,CPL} = 0$, the CPL parematrisation reduces to the ΛCDM model. The additional parameter, $w_{a,CPL}$, is what determines how w_{CPL} evolves over time. Consequently, if $w_{a,CPL} = 0$ then w_{CPL} becomes constant. Additionally, it provides a linear function between w_{CPL} and a which is one of the reasons why this model is commonly used [95]. Eq. 2.60 describes how the model describes the Universe at early and late times, by describing how w_{CPL} varies with a.

At high redshifts, w_{CPL} is constant and equal to $w_{0,CPL} + w_{a,CPL}$, meaning that for high reshifts, the CPL parameterization stops having a dynamical w. This changes at smaller redshifts as it diverges towards larger w_{CPL} for negative $w_{a,CPL}$.

The evolution from $w_{CPL} = w_{0,CPL} + w_{a,CPL}$ at early times to $w_{CPL} = w_{0,CPL}$ at current times is gradual and linear, seen in Fig. 2.4. One of the main advantages of this model is that it is well-behaved from $a = 0$ all the way to $a = 1$.

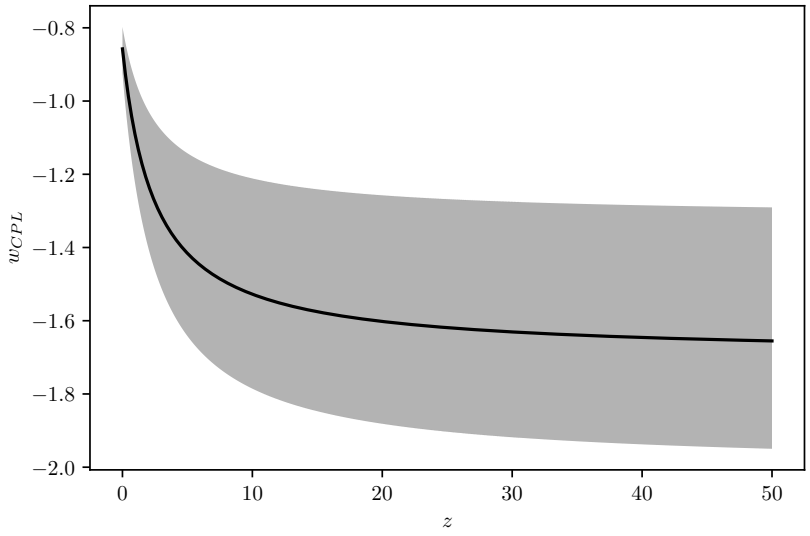

Figure 2.4: This graph shows how the CPL parameterization describes how w varies with z throughout the history of the Universe. The black line represents the equation of w_{CPL} and the grey shaded region represents the 1σ variation, where the values of $w_{0,CPL}$, $w_{a,CPL}$ and 1σ are results that were obtained and shown in Chapter 4.

Fig. 2.4 shows how the CPL parameterization is linear, and the main effect that this parameterization has in late times, showing a rapid decrease in the value of the equation of state parameter of dark matter from current times to late times. In the figure, $w_{0,CPL} = -0.858^{+0.060}_{-0.066}$ and $w_{a,CPL} = -0.84^{+0.32}_{-0.24}$ these values are the results retrieved from this model. The results of this parameterization are in Chapter 4 and discussed there.

Similar to the wCDM, the integration and differentiation of the CPL model shown in Eq. 2.60, were also calculated for the background and perturbation equations of this parameterization. Starting with integration,

$$\int_a^{a_0} \frac{3(1 + w_{CPL}(a))}{a} da \;=\; \int_a^{a_0} \frac{3(1 + w_{0,CPL} + w_{a,CPL}(1 - a))}{a} da\,, \quad (2.61)$$

$$
\begin{aligned}
&= \int_a^{a_0} \frac{3(1+w_{0,CPL}+w_{a,CPL})}{a} da \,, \\
&- \int_a^{a_0} \frac{3w_{a,CPL}}{a} da \qquad (2.62) \\
&= [3(1+w_{0,CPL}+w_{a,CPL})\ln(a) \\
&- 3w_{a,CPL}\, a]\Big|_a^{a_0} \,, \qquad (2.63)
\end{aligned}
$$

Knowing that $a_0 = 1$, Eq. 2.63 continues as follows.

$$
\begin{aligned}
\int_a^{a_0} \frac{3(1+w_{CPL}(a))}{a} da &= 3(1+w_{0,CPL}+w_{a,CPL})\ln(a_0) - 3w_{a,CPL}a_0 \\
&- 3(1+w_{0,CPL}+w_{a,CPL})\ln(a) + 3w_{a,CPL}a \,, \quad (2.64) \\
&= 3(1+w_{0,CPL}+w_{a,CPL})\ln(1) - 3w_{a_{CPL}} \\
&- 3(1+w_{0,CPL}+w_{a,CPL})\ln(a) + 3w_{a,CPL}a \,, \quad (2.65) \\
&= 3(1+w_{0,CPL}+w_{a,CPL})\ln\left(\frac{1}{a}\right) \\
&+ 3w_{a,CPL}(a-1) \,. \qquad (2.66)
\end{aligned}
$$

Thus, Eq. 2.66 was substituted into the complete first Friedmann equation of a time-dependent w,

$$
\begin{aligned}
H^2 &= \frac{8\pi G}{3}\left[\rho_{r_0}a^{-4} + \rho_{m_0}a^{-3}\right] \\
&+ \frac{8\pi G}{3}\left[\rho_{DE}\exp\left[-3(1+w_{0,CPL}+w_{a,CPL})\ln\left(\frac{1}{a}\right)\right]\right] \\
&\times \frac{8\pi G}{3}\exp\left[3w_{a,CPL}(a-1)\right] \,. \qquad (2.67) \\
&= \frac{8\pi G}{3}\left[\rho_{r_0}a^{-4} + \rho_{m_0}a^{-3}\right] \\
&+ \frac{8\pi G}{3}\left[\rho_{DE}a^{3(1+w_{0,CPL}+w_{a,CPL})}\exp\left[3w_{a,CPL}(a-1)\right]\right] \qquad (2.68)
\end{aligned}
$$

After the Friedmann equation of the CPL parametrisation in Eq. 2.68, the next step is to differentiate Eq. 2.60 with respect to a,

$$
\begin{aligned}
\frac{dw_{CPL}(a)}{da} &= \frac{d(w_{0,CPL}+w_{a,CPL}(1-a)}{da} \,, \qquad (2.69) \\
&= -w_{a,CPL} \,. \qquad (2.70)
\end{aligned}
$$

Substituting $\frac{dw_{CPL}(a)}{da}$ in Eq. 2.70 into the equation for $c_{a,i}$ in Eq. 2.47 to obtain the equation for the adiabatic speed sound,

$$
c^2_{a,CPL} = w_{CPL} + \frac{aw_{a,CPL}}{3(1+w_{CPL})} \,. \qquad (2.71)
$$

Thus, perturbation equations can be evaluated from Eq. 2.71. Since the first Friedmann equation and the adiabatic speed sound in Eq. 2.68 and Eq. 2.71 respectively are known, then this model can be implemented in simulations, and results of the CPL parametrisation can be achieved.

2.2.3 | Quadratic Model

The Jassal-Bagla-Padmanabhan (JBP) parametrisation was introduced by H. K. Jassal, J. S. Bagla, and T. Padmanabhan in the early 2000s [67]. This parametrization is particularly useful because it provides a simple yet more flexible way than the CPL model as it describes the dark energy equation of state parameter [123] as,

$$w_{JBP}(a) = w_{0,JBP} + w_{a,JBP}\, a(1-a)\,. \tag{2.72}$$

At first glance, Eq. 2.72 might seem to be very similar to the CPL. However, the extra degree of a explains the evolution of w quadratically which is different from the previous model and this extra degree is what makes this parameterization more general. The JBP model explains the evolution of w such that it affects the Universe only during early times. Thus, w is only dynamic at early times while at current and late times w is constant.

Similarly to the CPL model, after the Big Bang, in the early Universe, w_{JBP} does not behave dynamically and is a constant, $w_{JBP} = w_{0,JBP}$. It becomes dynamical when it approaches late time and behaves quadratically unlike the previously discussed parameterization. Similar to the CPL parameterization, JBP limits to the ΛCDM model when $w_{0,JBP} = -1$ and $w_{a,JBP} = 0$.

Fig. 2.5 is a graph which shows how the JBP parameterization describes the Universe that has a varying w only at late times and it varies quadratically. The values of $w_{0,JBP}$ and $w_{a,JBP}$ were taken as -0.878 and -1.12 respectively. The shaded region representing the 1σ variation of $w_{0,JBP}$ and $w_{a,JBP}$ were taken as $1\sigma_{w_{0,JBP}} = ^{+0.078}_{-0.022}$ and $1\sigma_{w_{a,JBP}} = ^{+0.29}_{-0.47}$. These values will be further discussed in Chapter 4. Fig. 2.5 shows how at high and close to zero redshifts the value of w_{JBP} is less than -1 but at low redshifts w_{JBP} is less than -1 showing that the Universe is exhibiting phantom energy.

Similar to the previous parameterizations, the differentiated and integrated equation of $w_{JBP}(a)$ are required to be known as they are needed for the first Friedmann equation as well as the equation for the adiabatic speed sound, which are crucial in order to have a complete picture of the evolution of the Universe de-

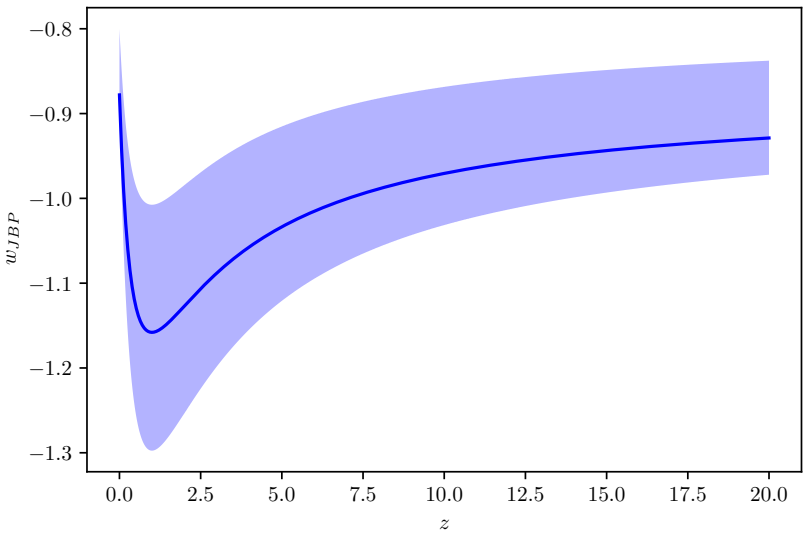

Figure 2.5: This figure shows how w varies with z in the JBP parameterization. The blue curve is the equation of state parameter of dark energy taking the result achieved in Chapter 4 while the shaded region is the 1σ variation.

scribed by this model. First starting with integration,

$$\int_a^{a_0} \frac{3(1+w_{JBP}(a))}{a} da = \int_a^{a_0} \frac{3(1+w_{0,JBP}+w_{a,JBP}\, a(1-a))}{a} da\,, \quad (2.73)$$

$$= \int_a^{a_0} \frac{3(1+w_{0,JBP})}{a} - 3w_{a,JBP}\,(1-a) da\,, \quad (2.74)$$

$$= [3(1+w_{0,JBP})\ln(a) + 3w_{a,JBP}\, a - \frac{3w_{a,JBP}\, a^2}{2}]\Big|_a^{a_0}\,, \quad (2.75)$$

Substituting $a_0 = 1$, Eq. 2.75 continues as follows.

$$\begin{aligned}\int_a^{a_0} \frac{3(1+w_{JBP}(a))}{a} da &= 3(1+w_{0,JBP})\ln(a_0) + 3w_{a,JBP}\, a_0 - \frac{3w_{a,JBP}\, a_0^2}{2} \\ &- 3(1+w_{0,JBP})\ln(a) - 3w_{a,JBP}\, a \\ &+ \frac{3w_{a,JBP}\, a^2}{2}\,, \\ &= 3(1+w_{0,JBP})\ln\left(\frac{1}{a}\right) + 3w_{a,JBP} - \frac{3w_{a,JBP}}{2}\end{aligned} \quad (2.76)$$

$$- \quad 3w_{a,JBP}\, a + \frac{3w_{a,JBP}\, a^2}{2}, \tag{2.77}$$

$$= \quad 3(1+w_{0,JBP}) \ln\left(\frac{1}{a}\right) + 3w_{a,JBP}\,(1-a)$$

$$+ \quad \frac{3w_{a,JBP}}{2}(a^2-1)\,. \tag{2.78}$$

Therefore, from Eq. 2.54, the first Friedmann equation of the JBP parameterization can be written as

$$\begin{aligned} H^2 &= \frac{8\pi G}{3}\left[\rho_{r_0}a^{-4} + \rho_{m_0}a^{-3}\right] \\ &+ \frac{8\pi G}{3}\left[\rho_{DE}\exp\left[-3(1+w_{0,JBP})\ln\left(\frac{1}{a}\right)\right]\right] \\ &\times \exp\left[3w_{a,JBP}(1-a) + \frac{3w_{a,JBP}}{2}(a^2-1)\right], \end{aligned} \tag{2.79}$$

$$\begin{aligned} &= \frac{8\pi G}{3}\left[\rho_{r_0}a^{-4} + \rho_{m_0}a^{-3}\right] \\ &+ \frac{8\pi G}{3}\left[\rho_{DE}a^{-3(1+w_{0,JBP})}\right] \\ &\times \exp\left[3w_{a,JBP}\left[(1-a) + \frac{(a^2-1)}{2}\right]\right]. \end{aligned} \tag{2.80}$$

Similar to the other parametrisation models, w is differentiated to get the equation for $c_{a,i}$ for this specific equation of state parameter.

$$\frac{dw_{JBP}(a)}{da} = \frac{d(w_{0,JBP} + w_{a,JBP}\, a(1-a)}{da}, \tag{2.81}$$

$$= w_{a,JBP} - 2aw_{a,JBP}\,. \tag{2.82}$$

The differentiation in Eq. 2.82 is then substituted in Eq. 2.47, resulting in the equation of $c_{a,i}$ of the JBP parametrisation to be

$$c^2_{a,JBP} = w_{JBP} - \frac{aw_{a,JBP}(1-2a)}{3(1+w_{JBP})}\,. \tag{2.83}$$

From, Eq. 2.80 and Eq. 2.83 the background as well as the perturbation equations are known and can be implemented into simulations so that results for the JBP parametrisation can be retrieved.

2.2.4 | Logarithmic model

The G. Efstathiou (GE) parametrisation was proposed by George Efstathiou [41] and is often referred to as the logarithmic model, as it describes the time evolution

for $w(a)$ logarithmically by describing it as

$$w(a) = w_{0,GE} - w_{a,GE} \ln(a) \, . \tag{2.84}$$

The evolution of this parameterization is completely different from all the other models. Despite the fact that this model behaves logarithmically, when $z = 0$ this model crosses the point of $w_{GE} = w_{0,GE}$. The value of $w_{a,GE}$ cannot be higher than 0 or else there will be stability. Also, when $w_{a,GE} > 0$, it will go against the assumption that was taken that at late times, $w(a) < -\frac{1}{3}$, that is required for an accelerating Universe.

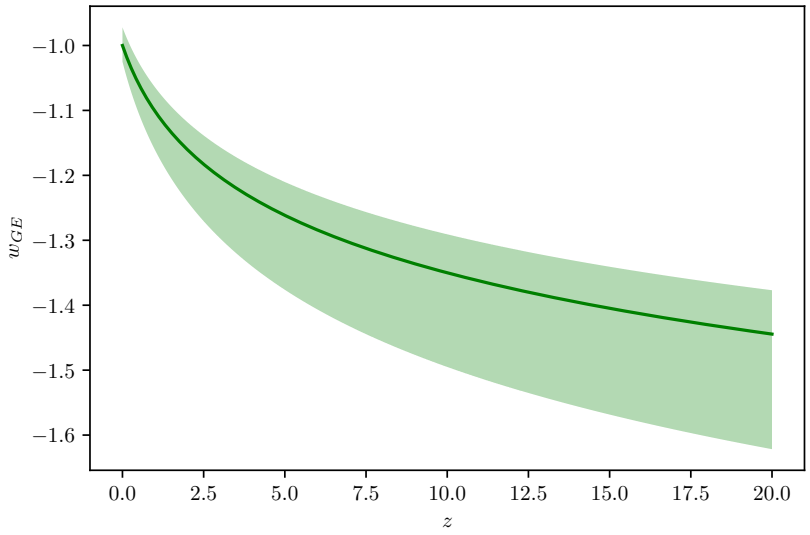

Figure 2.6: A graph of w against z for the GE parameterization, where the curve shows how w_{GE} varies when adding the values obtained as shown in Chapter 4 while the shaded region shows the 1σ variation.

Fig. 2.6 shows visually the logarithmic effect on w_{GE} when the values for $w_{0,GE}$ and $w_{a,GE}$ where taken as $-1.000^{+0.028}_{-0.025}$ and $-0.146^{+0.013}_{-0.054}$ respectively. These values will be discussed in Chapter 4. The graph shows how the value of w_{GE} increases from early time to current time. During late times the increase is more rapid when compared to early times. This model describes the Universe exhibiting phantom energy throughout its history.

For the background equations, specifically for the complete first Friedmann equation of this version of $w_{GE}(a)$, the term $\int_a^{a_0} 3\frac{1+w_{GE}(a)}{a} da$ needs to be calculated as

follows:

$$\int_a^{a_0} \frac{3(1+w_{GE}(a))}{a} da = \int_a^{a_0} \frac{3(1+w_{0,GE}-w_{a,GE}\ln(a))}{a} da \,, \tag{2.85}$$

Taking $u = 1 + w_{0,GE} - w_{a,GE}\ln(a)$ and $du = -\frac{w_{a,GE}}{a}$ the equation becomes

$$\begin{aligned} \int_a^{a_0} \frac{3(1+w_{GE}(a))}{a} da &= -\frac{3}{w_{a,GE}} \int_a^{a_0} u\, du \,, & (2.86)\\ &= -\frac{3}{w_{a,GE}} \left[\frac{u^2}{2}\right] \Big|_a^{a_0} \,. & (2.87) \end{aligned}$$

After substituting $a_0 = 1$, Eq. 2.87 becomes

$$\begin{aligned} \int_a^{a_0} \frac{3(1+w_{GE}(a))}{a} da &= -\frac{3}{w_{a,GE}} \left[\frac{(1+w_{0,GE})^2}{2}\right] \\ &+ \frac{3}{w_{a,GE}} \left[\frac{(1+w_{0,GE}-w_{a,GE}\ln(a))^2}{2}\right] \,. \end{aligned} \tag{2.88}$$

Then, the calculated term $\int_a^{a_0} \frac{3(1+w_{GE}(a))}{a} da$ in Eq. 2.88, is substituted into the first Friedmann equation with a time-dependent w shown in Eq. 2.42.

$$\begin{aligned} H^2 &= \frac{8\pi G}{3}\left[\rho_{r_0} a^{-4} + \rho_{m_0} a^{-3}\right] \\ &+ \frac{8\pi G}{3}\left[\rho_{DE} \exp\left[\frac{3}{w_{a_{GE}}}\left[\frac{(1+w_{0_{GE}})^2}{2}\right]\right]\right] \\ &\times \exp\left[-\frac{3}{w_{a,GE}}\left[\frac{(1+w_{0,GE}-w_{a,GE}\ln(a))^2}{2}\right]\right] \,. \end{aligned} \tag{2.89}$$

So, Eq. 2.89 is the first Friedmann equation of the GE parametrisation. Since in Eq. 2.88, $w_{a,GE}$ is in the denominator it cannot be zero. Therefore, the integral needs to be recalculated for the case of when $w_{a,GE}$. Thus, the equation of the model, after taking $w_{0,GE} = 0$, becomes $w_{GE}(a) = w_{0,GE}$. Then, the integration goes as follows,

$$\begin{aligned} \int_a^{a_0} \frac{3(1+w_{GE}(a))}{a} da &= \int_a^{a_0} \frac{3(1+w_{0,GE})}{a} da \,, & (2.90)\\ &= 3(1+w_{0,GE})\ln(a)\Big|_a^{a_0} \,, & (2.91)\\ &= -3(1+w_{0,GE})\ln(a) \,. & (2.92) \end{aligned}$$

So then, the Friedmann equation for the case when $w_{0,GE} = 0$,

$$\begin{aligned} H^2 &= \frac{8\pi G}{3}\left[\rho_{r_0}a^{-4} + \rho_{m_0}a^{-3}\right] \\ &+ \frac{8\pi G}{3}\left[\rho_{DE}\exp\left[3(1+w_{0,GE})\ln(a)\right]\right] , \qquad (2.93) \\ &= \frac{8\pi G}{3}\left[\rho_{r_0}a^{-4} + \rho_{m_0}a^{-3} + \rho_{DE}a^3(1+w_{0,GE})\right] . \qquad (2.94) \end{aligned}$$

Hence, $c_{a,i}$ needs to be obtained for the perturbation equations so, $w_{GE}(a)$ was differentiated,

$$\begin{aligned} \frac{dw_{GE}(a)}{da} &= \frac{d(w_{0,GE} - w_{a,GE}\ln(a))}{da} , \qquad (2.95) \\ &= -\frac{w_{a,GE}}{a} . \qquad (2.96) \end{aligned}$$

For the perturbation equations, the differentiation in Eq. 2.96 is input in Eq. 2.47 ,

$$c^2_{a,GE} = w_{GE} + \frac{w_{a,GE}}{3(1+w_{GE})} . \qquad (2.97)$$

Now, the cases of $w_{a,GE} < 0$ and $w_{a,GE} = 0$ were implemented in simulations for the two Friedmann equations, Eq. 2.89 and Eq. 2.94 and the equation for the adiabatic speed sound in Eq. 2.97.

2.2.5 | Barboza and Alcaniz

The Barboza and Alcaniz (BA) is a parametric model for dark energy, proposed by E.M. Barboza Jr. and J.S. Alcaniz which was first introduced in 2008 [14, 93]. It is another model that has a dynamical w and that can be used to describe the time evolution of this new varying parameter. This model was chosen since despite it being different from the other four models it is still mathematically simple. The BA model is represented by [123],

$$w(a) = w_{0,BA} + w_{a,BA}\left[\frac{1-a}{2a^2 - 2a + 1}\right] , \qquad (2.98)$$

Eq. 2.98 shows that similar to the CPL parameterization, at high redshifts $w_{BA} = w_{0,BA} + w_{a,BA}$, but for low redshifts $w_{BA} = w_{0,BA}$. Also, similar to the previous models, this parameterisation limits to the ΛCDM model when $w_{0,BA} = -1$ and $w_{a,BA} = 0$.

Fig. 2.7 shows how this parametrisation varies w_{BA} in a way that varies at late and current times but quickly becomes constant when it approaches early time.

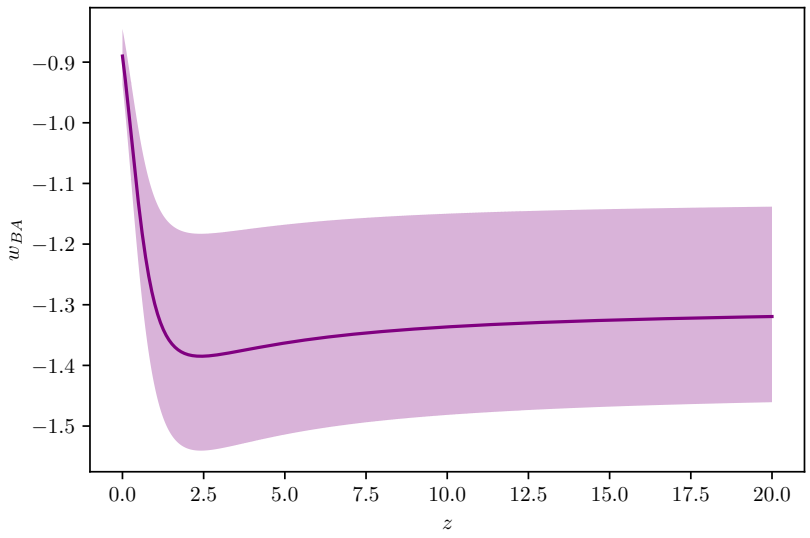

Figure 2.7: A graph demonstating how w_{BA} varies with z. The curve is w_{BA} when z is varying while the shaded region is the 1σ variation. The values needed were taken from the results shown in Chapter 4.

It shows that at a point during late time w experiences a dip in its value just before its value rapidly increases in current times. In order to plot w_{BA}, results that can be found in Chapter 4 were taken: $w_{0_{BA}} = -0.890^{+0.045}_{-0.047}$ and $w_{a_{BA}} = -0.41^{+0.13}_{-0.09}$ these will be further discussed later on. The figure shows that the model describes the Universe as exhibiting phantom energy, except at current times as it goes to values less than -1.

Like the other models that were discussed, integration as well and differentiation are needed for the background and perturbation equations. Starting with the calculation of the first Friedmann equation for this model, Eq. 2.98 was integrated as follows,

$$\int_a^{a_0} \frac{3(1+w_{BA}(a))}{a} da = \int_a^{a_0} \frac{3\left(1+w_{0,BA}+w_{a,BA}\left[\frac{1-a}{2a^2-2a+1}\right]\right)}{a} da \,, \quad (2.99)$$

$$= 3\int_a^{a_0} \frac{(-w_{0,BA}-1)(2a^2-2a+1)}{a(2a^2-2a+1)} + \frac{w_{a,BA}(a-1)}{a(2a^2-2a+1)} da \,, \quad (2.100)$$

$$
\begin{aligned}
&= 3\int_a^{a_0} \frac{2aw_{a,BA} - w_{a,BA}}{(2a^2 - 2a + 1)} \\
&- \frac{w_{a,BA} + w_{0,BA} + 1}{a} da \, . \qquad (2.101)
\end{aligned}
$$

To be able to continue with the integration, $u = 2a^2 - 2a + 1$ and $du = (4a - 2)da$ were substituted into Eq. 2.101.

$$
\begin{aligned}
\int_a^{a_0} \frac{3(1 + w_{BA}(a))}{a} da &= -\frac{3w_{a,BA}}{2} \int_a^{a_0} \frac{1}{u} du \\
&+ 3(w_{a,BA} + w_{0,BA} + 1) \ln(a)\Big|_a^{a_0} \, , \qquad (2.102) \\
&= -\frac{3w_{a,BA}}{2} \ln(u)\Big|_a^{a_0} \\
&+ 3(w_{a,BA} + w_{0,BA} + 1) \ln(a)\Big|_a^{a_0} \, , \qquad (2.103) \\
&= -\frac{3w_{a,BA}}{2} \ln(2a^2 - 2a + 1)\Big|_a^{a_0} \\
&+ 3(w_{a,BA} + w_{0,BA} + 1) \ln(a)\Big|_a^{a_0} \, , \qquad (2.104) \\
&= \frac{3w_{a,BA}}{2} \ln(2a^2 - 2a + 1) \\
&- 3(w_{a,BA} + w_{0,BA} + 1) \ln(a) \, . \qquad (2.105)
\end{aligned}
$$

Therefore, the Friedmann equation for the BA parametrisation is

$$
\begin{aligned}
H^2 &= \frac{8\pi G}{3} \left[\rho_{r_0} a^{-4} + \rho_{m_0} a^{-3}\right] \\
&+ \frac{8\pi G}{3} \left[\rho_{DE} \exp\left[-\frac{3w_{a,BA}}{2} \ln(2a^2 - 2a + 1)\right]\right] \\
&\times \exp\left[3(w_{a,BA} + w_{0,BA} + 1) \ln(a)\right] \, , \qquad (2.106) \\
&= \frac{8\pi G}{3} \left[\rho_{r_0} a^{-4} + \rho_{m_0} a^{-3}\right] \\
&+ \frac{8\pi G}{3} \left[\rho_{DE} (2a^2 - 2a + 1)^{-\frac{3w_{a,BA}}{2}} a^{3(w_{a,BA} + w_{0,BA} + 1)}\right] \, . \qquad (2.107)
\end{aligned}
$$

Moving on to obtaining $c_{a,i}$, the differentiation of Eq. 2.98 was done as shown:

$$
\begin{aligned}
\frac{dw_{BA}(a)}{da} &= \frac{d\left(w_{0,BA} + w_{a,BA}\left[\frac{1-a}{2a^2-2a+1}\right]\right)}{da} \, , \qquad (2.108) \\
&= -w_{a,BA}\left[\frac{1}{(2a^2 - 2a + 1)} + \frac{(1-a)(4a-2)}{(2a^2 - 2 + 1)^2}\right] \, , \qquad (2.109)
\end{aligned}
$$

$$= -w_{a,BA}\left[\frac{1}{2a^2-2a+1} - \frac{-4a^2+6a-2}{(2a^2-2a+1)^2}\right], \tag{2.110}$$

$$= -w_{a,BA}\left[\frac{(2a^2-2a+1)+(-4a^2+6a-2)}{(2a^2-2a+1)^2}\right], \tag{2.111}$$

$$= w_{a,BA}\frac{(2a^2-4a+1)}{(2a^2-2a+1)^2}. \tag{2.112}$$

From Eq. 2.98, then $c^2_{a,i}$ for the JBP parametrisation is,

$$c^2_{a,BA} = w_{BA} - \frac{aw_{a,BA}}{3(1+w_{BA})}\frac{2a^2-4a+1}{(2a^2-2a+1)^2}. \tag{2.113}$$

Since the background and perturbation equations for the BA parametrisation were computed, the results for this parametrisation can be obtained with the help of simulations that will be discussed more in chapter 3.

2.2.6 | Oscillatory model

A different model to the previous ones is the oscillatory (OSCILL) model [126, 77]. Oscillatory models are a good idea to be considered as they allow w to exhibit oscillatory behaviour over time, rather than being constant or following a simple linear trend, offering a more flexible framework to describe the evolution of dark energy. This parameterization is a general oscillatory wCDM parameterization and it was chosen as it gives the opportunity to be able to test if an oscillatory dark energy equation of state can lessen tensions when confronted with observational data. Some scalar field models of dark energy naturally lead to oscillatory solutions such as quintessence or phantom fields can exhibit oscillatory behaviour. Thus, this periodic variation might be able to explain cosmological discrepancies. [78]

$$w_{OSCILL}(a) = w_{0,OSCILL} + w_{a,OSCILL}\left[a\sin\left(\frac{1}{a}\right) - \sin(1)\right], \tag{2.114}$$

This parameterization also limits to the standard model $w_{OSCILL}(a) = -1$ when $w_{0,OSCILL} = -1$ and $w_{a,OSCILL} = 0$. The OSCILL model is the only model out of the six models to vary $w_{OSCILL}(a)$ throughout the history of the cosmos by oscillating it at current time, late time and early time. The general version of Eq. 2.114 can be found in [126, 77] where the authors considered other free parameters such as the period of oscillations, therefore leading to an extended parameter space. As a large number of parameters generally leads to degeneracy among them, in this work only two-parameter models were considered.

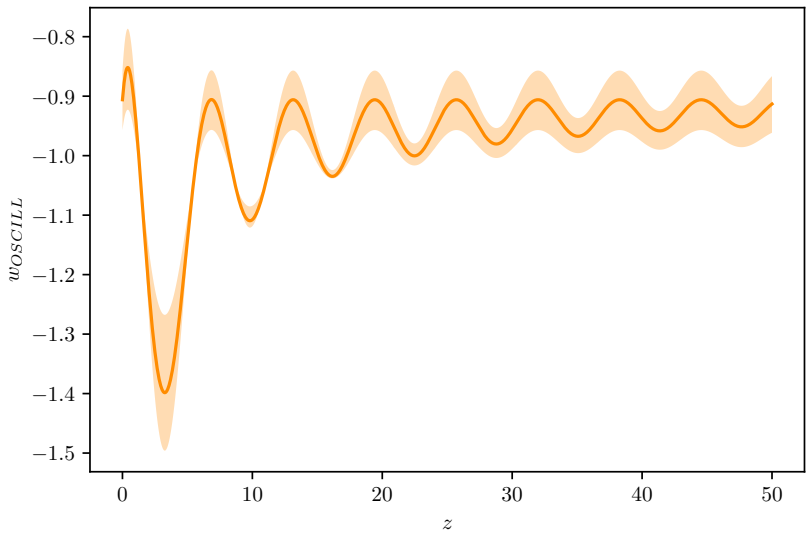

Figure 2.8: This graph shows how the OSCILL model varies w_{OSCILL} with respect to z. The curve shows the w_{OCILL} and the shaded shows the 1σ variation.

Fig. 2.8 shows the oscillatory behaviour of w_{OSCILL}. Showing that in late times the amplitude of the oscillations are larger when compared to the oscillations in early times. In fact the oscillations continue to decrease as z increases. The values needed for the plotting of this graph are the results that were achieved from this choice of parameterization that are shown in Chapter 4. The values of $w_{0,OSCILL}$ and $w_{a,OSCILL}$ were taken as $-0.910^{+0.042}_{-0.043}$ and $1.08^{+0.28}_{-0.33}$ respectively.

Like the other models, the differentiation and integration of Eq. 2.114 are needed for the background and perturbation equations respectively. For the completion of the first Friedmann equation, the term $\int_a^{a_0} 3\frac{(1+w_{OSCILL}(a)}{a}da$ in Eq. 2.12 was achieved by

$$\begin{aligned}\int_a^{a_0} \frac{3(1+w_{OSCILL}(a))}{a}da &= \int_a^{a_0} \frac{3(1+w_{0,OSCILL})}{a} \\ &+ \frac{3w_{a,OSCILL}\left[asin\left(\frac{1}{a}\right) - sin(1)\right]}{a}da \\ &= \int_a^{a_0} \frac{3w_{a,OSCILL}\left[a\sin\left(\frac{1}{a}\right) - \sin(1)\right]}{a}\end{aligned} \tag{2.115}$$

$$+ \quad \frac{3w_{0,OSCILL}}{a} + \frac{3}{a}da \,, \tag{2.116}$$

$$= \quad 3\int_a^{a_0} w_{a,OSCILL} \sin\left(\frac{1}{a}\right) - \frac{w_{a,OSCILL}\sin(1)}{a}$$

$$+ \quad \frac{w_{0,OSCILL}}{a} + \frac{1}{a}da \,, \tag{2.117}$$

$$= \quad 3\int_a^{a_0} w_{a,OSCILL} \sin\left(\frac{1}{a}\right) da$$

$$- \quad 3w_{a,OSCILL}\sin(1)\ln(a) + 3w_{0,OSCILL}\ln(a)$$

$$+ \quad 3\ln(a) \,. \tag{2.118}$$

For the term $3\int_a^{a_0} w_{a,OSCILL} \sin\left(\frac{1}{a}\right) da$, the method of integration by parts can be used. Taking the choice of,

$$f = \sin\left(\frac{1}{a}\right), \; g' = 1 \,, \tag{2.119}$$

$$f' = -\frac{\cos\left(\frac{1}{a}\right)}{a^2}, \; g = a \,, \tag{2.120}$$

The integral becomes

$$3\int_a^{a_0} w_{a,OSCILL} \sin\left(\frac{1}{a}\right) da \quad = \quad 3w_{a,OSCILL}\left[\sin\left(\frac{1}{a}\right)\right]$$

$$+ \quad 3w_{a,OSCILL}\left[\int_a^{a_0} \frac{\cos\left(\frac{1}{a}\right)}{a^2}\right] da \,, \tag{2.121}$$

For simplicity, when substituting $u = \frac{1}{a}$ and $du = -\frac{1}{a^2}da$, the integration leads to

$$3\int_a^{a_0} w_{a,OSCILL} \sin\left(\frac{1}{a}\right) da \quad = \quad 3w_{a,OSCILL}\left[\sin\left(\frac{1}{a}\right) a\right]$$

$$+ \quad 3w_{a,OSCILL}\left[\int_a^{a_0} \frac{\cos(u)}{u} du\right] \,, \tag{2.122}$$

$$= \quad 3w_{a,OSCILL}\left[a\sin\left(\frac{1}{a}\right) + \mathrm{Ci}(u)\right] \,, \tag{2.123}$$

Since the integration of $3\int_a^{a_0} w_{a_{OSCILL}} \sin\left(\frac{1}{a}\right) da$ is obtained, the full integration of the OSCILL model is,

$$\int_a^{a_0} \frac{3(1+w_{OSCILL}(a))}{a} da \quad = \quad -3(w_{a,OSCILL}\sin(1) - w_{0,OSCILL})\ln(a)\Big|_a^{a_0}$$

$$
\begin{aligned}
&- \left[3\ln(a) - 3w_{a,OSCILL} a \sin\left(\frac{1}{a}\right)\right]\Big|_a^{a_0} \\
&- 3w_{a,OSCILL}\mathrm{Ci}\left(\frac{1}{a}\right)\Big|_a^{a_0}, \qquad (2.124)\\
&= 3w_{a,OSCILL}(\sin(1) - \mathrm{Ci}(1)) \\
&+ 3(w_{a,OSCILL}\sin(1) - w_{0,OSCILL} - 1)\ln(a) \\
&- 3w_{a,OSCILL}\left[a\sin\left(\frac{1}{a}\right) - \mathrm{Ci}\left(\frac{1}{a}\right)\right]. \qquad (2.125)
\end{aligned}
$$

Then, after substituting Eq. 2.125 into the first Friedmann equation for the wCDM models in Eq. 2.42, the Friedmann equation for the OSCILL parameterization is

$$
\begin{aligned}
H^2 &= \frac{8\pi G}{3}\left[\rho_{r_0}a^{-4} + \rho_{m_0}a^{-3}\right] \\
&+ \frac{8\pi G}{3}\left[\rho_{DE}\exp\left[-3w_{a,OSCILL}(\sin(1) - \mathrm{Ci}(1))\right]\right] \\
&\times \exp\left[-3(w_{a,OSCILL}\sin(1) - w_{0,OSCILL} - 1)\ln(a)\right] \\
&\times \exp\left[3w_{a,OSCILL}\left[a\sin\left(\frac{1}{a}\right) - \mathrm{Ci}\left(\frac{1}{a}\right)\right]\right], \qquad (2.126)\\
&= \frac{8\pi G}{3}\left[\rho_{r_0}a^{-4} + \rho_{m_0}a^{-3}\right] \\
&+ \frac{8\pi G}{3}\left[\rho_{DE}\exp\left[-3w_{a,OSCILL}(\sin(1) - \mathrm{Ci}(1))\right]\right] \\
&\times a^{-3(w_{a,OSCILL}\sin(1) - w_{0,OSCILL} - 1)} \\
&\times \exp\left[3w_{a,OSCILL}\left[a\sin\left(\frac{1}{a}\right) - \mathrm{Ci}\left(\frac{1}{a}\right)\right]\right]. \qquad (2.127)
\end{aligned}
$$

Then, for the $c_{a,i}$ of this parametrisation, the differentiation of Eq. 2.114 was computed as demonstrated below:

$$
\begin{aligned}
\frac{dw_{OSCILL}(a)}{da} &= \frac{d\left(w_{0,OSCILL} + w_{a,OSCILL}\left[a\sin\left(\frac{1}{a}\right) - \sin(1)\right]\right)}{da}, \qquad (2.128)\\
&= w_{a,OSCILL}\sin\left(\frac{1}{a}\right) - \frac{a w_{a,OSCILL}\cos\left(\frac{1}{a}\right)}{a^2}, \qquad (2.129)\\
&= w_{a,OSCILL}\sin\left(\frac{1}{a}\right) - \frac{w_{a,OSCILL}\cos\left(\frac{1}{a}\right)}{a}. \qquad (2.130)
\end{aligned}
$$

Substituting into Eq. 2.47,

$$c^2_{a,OSCILL} = w_{OSCILL} - \frac{a w_{a_{OSCILL}}}{3(1+w_{OSCILL})}\left(\sin\left(\frac{1}{a}\right) - \frac{\cos\left(\frac{1}{a}\right)}{a}\right) . \tag{2.131}$$

Now, by having the equations, Eq. 2.127 and Eq. 2.131, the focus can shift to simulating the model and obtaining results for the OSCILL parameterization.

2.2.7 | Conclusion

In conclusion, the literature reveals that the wCDM model, characterized by a dynamic w, offers a more general framework than the ΛCDM model by allowing w to deviate from the cosmological constant value of -1 and adding it as a parameter with the six parameters that the ΛCDM model uses to constrain the CMB power spectrum. This flexibility enables the model to better accommodate observational data from various cosmological probes, including the CMB, supernovae Type Ia, and BAO. The changes in w affect the form of the background equations since $\rho_{de}(a)$ becomes time-dependent. However, when it comes to the perturbation equations, the general form is the same as the ΛCDM model but they are still affected indirectly. The six chosen models that are considered in this project are: w_0CDM, CPL, JBP, GE, BA and OSCILL. The reason why these models were considered is that apart from them being heavily backed up by research they all describe the evolution of the Universe in different ways, especially in early times, and they are all restricted to mostly two free parameters which avoids degeneracies between parameters. The integration and differentiation of w for each model were calculated so that the first Friedmann equation for a time-dependant w and for the adiabatic speed sound, $c_{a,i}$ are known for each parametrisation, which is in preparation for them to be implemented in the simulations, and hence, for the results to be obtained. The next step is to discuss which simulations were chosen for the generation of the results for each of the six parameterisation models, which will be discussed in Chapter 3.

3

Data & Simulations

In order to test out wCDM and produce results from it which are then later analysed, the data needs to be chosen as well as the simulators. The data is obtained from telescopes which gather observational measurements from the early and late time Universe. The role of the simulators is to make calculations by using the model that is being tested together with the data and then plot graphs from the results.

From the data sets, simulations are able to calculate the likelihood function $L(\Theta|D)$ and it expresses the probability of the observed data given a particular model with parameters Θ where D is the vector of observed data points. The likelihood function uses χ^2, which is a measure of how well a theoretical model fits observed data. χ^2 is defined as

$$\chi^2 = V^T C^{-1} V \,, \tag{3.1}$$

where V is the residual vector which represents the difference between observed data and model predictions. This means that each component of this vector indicates how far a data point is from the predicted value. C is the covariance matrix which contains the uncertainties and correlations. If the data points are uncorrelated, the covariance matrix is diagonal, with each element being the variance of a data point.

A low value of χ^2 indicates a good fit, where the model predictions are close to the data within the expected measurement uncertainties. On the other hand, a high value of χ^2 suggests a poor fit, meaning the model predictions are significantly different from the observed data beyond what is expected by random chance. Thus, simulations aim to minimize χ^2 as much as possible.

The covariance matrix C is essential in the likelihood function as it captures the

statistical properties of the data. The diagonal elements of the covariance matrix represent the variances (squared uncertainties) of individual measurements. Therefore, the larger values indicate more uncertainty. While the off-diagonals represent covariances, which measure the degree of correlation between different data points. Thus, non-zero off-diagonal terms indicate that changes in one measurement are related to changes in another.

In MontePython, each likelihood module often includes a predefined or user-provided covariance matrix that reflects the experimental uncertainties and correlations. Accurate covariance matrices are crucial because incorrect variances or correlations can bias parameter estimates and inflate or deflate uncertainties. Including correlations helps MontePython correctly weigh the data, especially when multiple measurements are not independent.

3.1 | Data

Observational data and measurements that provide insight into the conditions and state of the early Universe are usually referred to as early time data. While observations and measurements involving galaxies and galaxy clusters in the late Universe are commonly referred to as local time data or background data. This data particularly focusses on the cosmic structures that provide insights into the current state of the Universe.

Both early and late-time data are crucial for testing models that describe the Universe as the predictions made with the models need to agree with the observed data. They both separately are able to predict cosmological parameters such as H_0 and the wCDM parameters [2]. However, the late-time on its own is not able to make predictions on all the six ΛCDM parameter and on the σ_8 parameter while early-time data on its own can. Despite this, together the predictions will be more accurate since the combination of the observational data of the early and the late Universe will give a clearer picture of how the Universe evolved over time, and thus, constrain the model more efficiently [123].

In large datasets, for instance, Planck, Pantheon+SH0ES and DESI data, machine learning methods [21, 72] are particularly beneficial due to their ability to handle vast amounts of data and uncover subtle patterns. Machine learning can be used to preprocess and analyse data from the Planck satellite, improving the accuracy of CMB measurements. Machine learning techniques can enhance data preprocessing, feature extraction, and refine parameter estimation of large-scale data sets by minimizing the error between predicted and actual values [40, 61]. More

modern machine learning techniques like neural networks [124, 113] can model complex relationships between parameters and data, providing highly accurate estimations compared to traditional regression techniques.

3.1.1 | Early Time Data

The Cosmic Background Explorer (COBE) [105] satellite was launched in 1989 and was the first mission specifically designed to study the CMB radiation. COBE did not directly measure absolute temperatures in the CMB. Instead, it focused on mapping the "smoothness" of the CMB radiation field which in fact managed to discover minute temperature fluctuations. The key measurements from COBE were related to the anisotropies.

Then, the Wilkinson Microwave Anisotropy Probe (WMAP) [17] mission was launched in 2001 as a follow-up to COBE. Its objective was to measure temperature differences across the sky in the CMB and was specifically designed to map the temperature fluctuations in the CMB with much greater resolution and precision than COBE [105]. Instead of mapping the smoothness of the CMB, WMAP measured the absolute temperature of the CMB. It provides precise temperature values for different regions of the sky. WMAP data set produced an incredibly detailed and more refined map of the CMB anisotropies than COBE, and it also offered insights into the polarization of the CMB. Since WMAP has exact measurements of the CMB temperatures from the satellite's thermometers, it makes the data less precise.

After WMAP, the Planck mission was launched in 2009, and its first data set was released 2013 [3]. Planck also measures the CMB temperature fluctuations. However, it focusses more on relative temperature differences. Planck was designed to measure the CMB with even higher sensitivity, angular resolution, and frequency range than its predecessors. The Planck mission has an even broader frequency coverage when compared to its predecessors, which allowed it to better separate the CMB from foreground emissions [31]. It includes detailed maps of the temperature fluctuations, polarization data, and information on foreground emissions. Since the Planck data set has relative temperatures instead of exact values, it makes the data set more precise. Therefore, for the early time data, Planck 2020 (PR4) [110] and Planck 2018 (PR3) [5] were chosen. Both PR3 and PR4 data matched very closely the theoretical predictions made by the ΛCDM model which reinforces the validity of these early-time data sets.

Planck 2018 [1] (PR3) consists of ten data sets in total, six of which belong to the

[1]The PR3 data set can be found in the GitHub link:

high-l part and four belong to low-l [5]. From those, the data sets chosen for this project are:

- **low-l TT:**
  With this data set, the CMB TT likelihood, where l is $2 \leq l \leq 29$, [5] can be computed. By sampling the posterior distribution of the parameters of a model that combines the Planck maps to represent the CMB and the foreground emissions, the likelihood implements a Bayesian component-separation approach in pixel space [121]. The samples are then used to determine the low-l likelihood for any TT CMB spectrum that is foreground-marginalized [79].

- **low-l EE:**
  Calculating the EE likelihood in the range $l = 2 - 29$ is possible with this data set. High fidelity end-to-end simulations of the HFI instrument are compared to a cross-quasi-maximum-likelihood method (QML) on the 100 and 143 GHz maps in order to estimate the probability, as explained in [79].

- **high-l TT+TE+EE:**
  With the use of this data set, the CMB combined TT, TE, and EE probability may be calculated in the range $l = 30 - 2508$ for TT and $l = 30 - 1996$ for TE and EE. The file includes the binned half-mission T and E cross-spectra at 100 GHz, 143 GHz, and 217 GHz. Only the 100 × 100, 143 × 143, 143 × 217, and 217 × 217 spectra are truly employed in temperature; in contrast, all of them are used in TE and EE [5, 121]. For every spectrum, there are distinct masks and multipole ranges that are detailed in [79].

Planck 2020 [2] (PR4) data set used the six maps to derive the 15 cross-power spectra for each CMB mode, one each for 100×100, 143×143, and 217×217; and four each for 100×143, 100×217, and 143×217 [110]. In PR4 there are four high-l data sets and one low-l data set. Thus, for this project, the following data combination was chosen:

- **Lollipop:**
  - **low-l TT:**
    With this data set, the CMB TT likelihood, in the multipole range $l < 30$ can be computed. This data set used polarized frequencies from 30 to

https://github.com/carronj/plancklens.git

[2] The PR4 data set can be found in the GitHub link: https://github.com/planck-npipe

353 GHz [110]. It is based on cross-power spectra for which the bias is zero when the noise is uncorrelated between maps.

- **Hillipop:**
  - **high-l TT+TE+EE:**
    This data set covers the multipole range of $l = 30 - 2500$ of TT and $l = 30 - 2000$ for EE and TE and from this the CMB of TT, TE, EE can be calculated. The total number of multiples considered in this data set for TT + TE + EE is 29758 which is higher than the number of multiples in PR3 which was 25597 [110]. This data set makes use of the 15 cross-spectra computed from the six detset maps at 100, 143, and 217 GHz. From those 15 cross-spectra, the six cross-frequency spectra were derived after recalibration and co-addition. The use of all cross-frequencies allows the possibility of breaking some degeneracies in the foreground domain [110].

Lollipop only has low -l TT, so in the research, PR3 low- l EE was used in addition to the Lollipop data set for completeness of data. Planck data also includes data on massive neutrinos [52]. PR3 and PR4 have constraints on the sum of the masses of the neutrinos. The total mass of neutrinos is important as it affects the formation of large-scale structures in the universe and the CMB anisotropies [119].

In the early Universe, neutrinos used to move at relativistic speeds because they had very high kinetic energy compared to their tiny masses. This prevented clumping on small scales, known as the free-streaming effect. As the Universe expanded, it cooled down. This cooling process reduced the kinetic energy of particles, including neutrinos. The mass of neutrinos, although very small, became significant in this cooler, expanding Universe. Their mass influenced how they interacted with other particles and how they contributed to the overall mass-energy content of the Universe [119].

Planck data provides constraints on the sum of the masses of neutrinos, $\sum m_\nu$, by analyzing the CMB temperature and polarization power spectra and lensing potential power spectrum. The data does not measure the neutrino mass directly but places an upper limit on their total mass by studying their impact on the CMB and the distribution of matter [56].

Despite PR4 being the latest released data set by the Planck telescope, meaning that it has improved processing and calibration when compared to PR3, it has not been tested much, unlike PR3, which was used and tested for multiple models.

This makes PR3 more trustworthy than PR4 as there could be hidden inconsistencies with the recently released data set that have yet to be discovered through testing.

3.1.2 | Late Time Data

Late time, also known as local time, data sets help refine measurements of cosmic distances and refine the value of H_0 as they provide insights into dark energy. When late time data is added to early time data, it constrains the models even more. For the local time data, the data sets Cosmic Clocks 2016 (CC), Pantheon + SH0ES (SN+SH0ES) and Baryonic Acoustic Oscillations (BAO) transverse were used.

The CC data set [43] refers to a collection of observational data used to measure the expansion rate of the Universe using a method that relies on what is known as cosmic chronometers or cosmic clocks 2016 [59]. These chronometers are typically massive, passively evolving galaxies whose ages can be determined with high precision. The cosmic chronometer approach utilizes the ages of galaxies to measure H_0 at different redshifts [43, 71]. By comparing the relative ages of galaxies at different redshifts, one can infer the rate at which the Universe is expanding over time.

Pantheon+ (SN+) is an updated data set of Pantheon (SN) [23]. It is a compilation of over 1500 Type Ia supernovae data points ranging from the nearby to those at high redshifts. The SH0ES (Supernova H0 for the Equation of State) project [90] focusses on measuring H_0 using a variety of distance indicators, including Cepheid variable stars and Type Ia supernovae. The SH0ES team uses the Leavitt Law (or Period-Luminosity Relation) for Cepheid variables where the law states that the longer the pulsation period of a Cepheid variable, the brighter the star is intrinsically [20]. From this law, the distances from our Galaxy to nearby galaxies were measured. Then they used these measurements to calibrate the distances to Type Ia supernovae and calculated the value of H_0. The updated SN+ data set incorporates improvements in calibration, reduction of systematic errors, and a more comprehensive range of supernovae compared to its predecessor. With the incorporation of the SH0ES prior to the SN+ data set, the SN+SH0ES dataset [99] combines high-redshift supernova data with local measurements, leading to more accurate and reliable measurements of H_0.

The BAO transverse data set has measurements and data collected from the study of BAO in the distribution of galaxies. BAO originated in the early Universe when photons and baryons were tightly coupled due to Thomson scattering [37].

After the Universe cooled and expanded, photons decoupled from baryons, leaving an imprint in the form of density waves [53]. These oscillations affected the formation of galaxies, and so it affects large-scale structure. Large-scale surveys like the Sloan Digital Sky Survey (SDSS) [44, 50], the Dark Energy Survey (DES) [1], and the Baryon Oscillation Spectroscopic Survey (BOSS) [7] collect data on galaxy positions and redshifts. The data in this data set is one-dimensional, meaning that the BAO measurements are taken as if you are looking at the oscillations straight on, hence it is as if the oscillations are one-dimensional. The BAO transverse data set includes angular correlations of galaxies at different redshifts, allowing for the measurement of the BAO scale in the transverse direction taken from SDSS DR10 [27], SDSS DR11 [28] and BOSS DR10 [8].

The DESI 2024 (DESI) is 2D BAO data that was taken from the Dark Energy Spectroscopic Instrument. This data set used data from bright galaxies, the combined luminous red galaxies (LRGs) and emission-line galaxies (ELGs), quasars and the Lyman-α Forest [2]. The LRGs are older and massive galaxies, ELGs are younger, star-forming galaxies, quasars are luminous objects powered by supermassive black holes at the centres of galaxies, and the Lyman-α is a series of absorption features in the spectra of distant quasars that help probe the intergalactic medium. From these, DESI calculated the values of

$$\frac{D_H(z)}{r_d} = \frac{da(1+z)}{r_d}, \tag{3.2}$$

$$\frac{D_M(z)}{r_d} = \frac{c}{H(z)r_d}, \tag{3.3}$$

$$\frac{D_V(z)}{r_d} = \frac{(zD_M(z)^2 D_H(z))^{\frac{1}{3}}}{r_d}, \tag{3.4}$$

where D_H is the Hubble distance, D_M is the comoving angular diameter distance, D_V is the volume-averaged distance, da is the angular distance, the speed of light c in the paper is taken to be 1, and r_d is the sound horizon at the drag epoch which is when baryons decouple (i.e. when they stop moving). r_d can be expressed as

$$r_d = \int_{z_d}^{\infty} \frac{c_s(z)}{H_(z)}, \tag{3.5}$$

where c_s is the speed of sound before recombination.

3.2 | Simulation

After the choice of the data was made, the next step was choosing the simulation to calculate the theoretical predictions of the different models and choosing the

simulation that would plot the results. Simulations play a crucial role in modern cosmology, as they provide the means to model the Universe's evolution and compare theoretical predictions with observational data. Among the many tools developed for this purpose, Cosmic Linear Anisotropy Solving System (CLASS) and MontePython stand out for their importance and wide usage in the cosmological community.

3.2.1 | CLASS

Cosmic Linear Anisotropy Solving System[3] (CLASS) is a widely used software package designed to compute theoretical predictions for various cosmological observables [62]. It is a sophisticated software package designed to solve the equations governing the evolution of the Universe, particularly focussing on the behaviour of small perturbations around a homogeneous background as discussed in the previous chapter. It is a powerful tool that models the evolution of the Universe by solving Boltzmann equations which govern the behaviour of different components like dark matter, dark energy, baryons, photons, and neutrinos. CLASS can compute a wide range of cosmological observables, such as the CMB power spectrum, including temperature, polarization, and lensing effects [64]. It is also able to compute large-scale structure (LSS) observables, like the matter power spectrum, which is crucial for understanding the distribution of galaxies and other large-scale structures in the Universe.

This simulator was chosen since CLASS is optimized for speed and can handle complex computations in a relatively short time [63]. This efficiency makes it suitable for parameter estimation tasks, where many different models must be evaluated. CLASS can work with different cosmological models, including the standard ΛCDM model, as well as other models that stray away from the standard model in cosmology. This simulator is designed in a way, which allows for easy modification of the code to include these other models [62]. CLASS is coded in the programming language C. However, it has a Python wrapper that provides an interface to access its core functionalities directly from Python scripts, making it easier to integrate CLASS with other simulators.

CLASS begins by setting up initial conditions for the Universe based on parameters that are specified by the user. Then CLASS evolves the linear perturbations of the different components over time using the chosen data sets, in this case, PR4 or PR3 combined with CC, BAO and SN+SH0ES [62]. This involves solving the Boltzmann equations for the photons and neutrinos, the Einstein-Boltzmann

[3]CLASS can be downloaded with the GitHub link: https://github.com/lesgourg/class_public.git

equations for the metric perturbations, and continuity equations for matter components. These equations govern how small perturbations grow or decay as the Universe expands. Once the perturbations are evolved, CLASS calculates the relevant cosmological observables, such as the CMB power spectrum or the matter power spectrum [64]. These are derived from the evolved perturbations and can be directly compared to observational data. Subsequently, CLASS is able to output the computed observables in a format that can be used for further analysis, such as comparing with observational data or performing statistical analysis to constrain cosmological parameters [63].

In the baseline code, CLASS has inbuilt the w_0CDM model as well as the CPL model. However, the JBP, GE, BA and OSCILL models are not in CLASS. So, in this project, CLASS had to be modified for the other four wCDM models to be implemented. Additional code was added to the source code, which is written using the programming language C, to add the new models specifically in the section of the background w_{fld}. New cases were added one for each model. The choice of using cases for the implementation of the models was taken due to its simplicity and for it to be easy to switch from one model to the other by specifying which parametrisation to use. Each case includes the equation of state, the derivative of w with respect to a for the computation of the adiabatic sound speed in Eq. 2.47 as well as the integral term of w for the calculation of the Friedmann equation in Eq. 2.12 of each model. Each equation was shown and explained in Chapter 2. Pointers were assigned to each equation in each model. This was done to allow direct access to memory locations, which can lead to more efficient memory usage.

Specifically for the OSCILL model, its Friedmann equation, which was shown in Chapter 2 in Eq. 2.127, contains the Ci function [76], which is expressed as

$$Ci(x) = \int_x^\infty \frac{\cos(t)}{t} dt \, . \tag{3.6}$$

Unfortunately, CLASS does not have this function built into the base code. Therefore, a new file was added to the source code to handle this function by coding a numerical integrator. The code from this was taken from the Numerical Recipes in C by W. H. Press, et al [114]. However, the library complex.h which was used in the book was outdated, since from the time that the book was published, the library was updated and changes were made. The complex.h library was needed as it has the implementation of complex numbers.

So, the code from the book had to be adjusted and updated to work with the updated library. A new file in the source folder was added and named cisi.c. This

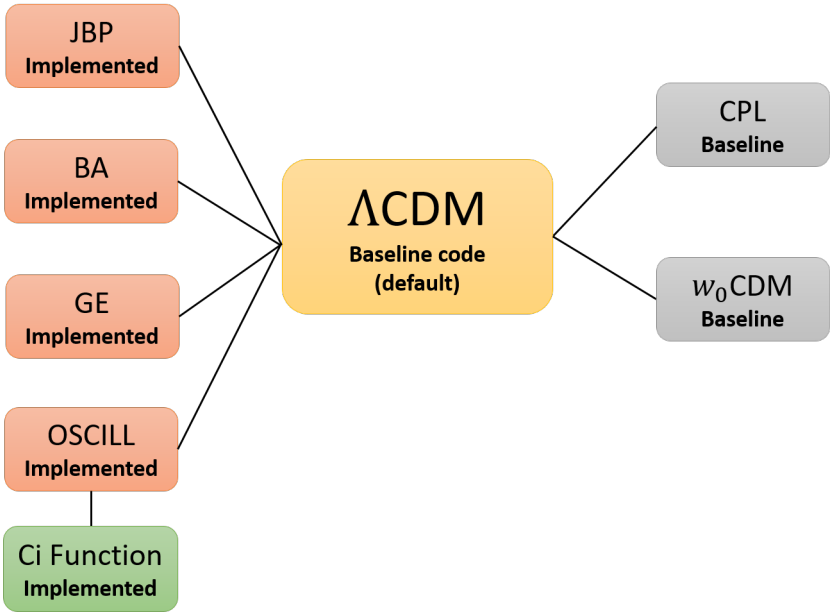

Figure 3.1: A diagram of all the models showing which ones were already inbuilt in CLASS and which models were not inbuilt and had to be implemented.

new file contains the updated code of the numerical integration of Ci function. Since a new file was added to the source folder, a header in the 'include' folder of CLASS of this numerical integral for the Ci function was needed to declare the function. The header file [115] is important as it enables the reusability of the function across different parts of CLASS without having to rewrite or duplicate the code. Therefore, a new header file cisi.h was added to the include folder. Whenever new files were added to CLASS, the make file had to be adjusted so that it includes the new files. This is so when CLASS is compiled, CLASS also compiles the new files. Fig 3.1 shows the ΛCDM model in the yellow box, which is inbuilt into the baseline code of CLASS and is automatically set as the default model. The w_0CDM and the CPL parametrisation models, shown in the grey boxes, are also in the baseline code of CLASS. The red boxes are the parametrisation models (JBP, GE, BA, OSCILL) that are not inbuilt into the CLASS code and had to be implemented by adding code to the source file of CLASS. Specifically for the OSCILL model, the Ci function had to be implemented as it is not inbuilt into CLASS.

The DESI data does not manage to constrain H_0 on its own. However, it does manage to constrain $H_0 r_d$, where r_d is the sound horizon at the drag epoch, which is when baryonic matter stopped moving. Hence, another parameter had to be

added to the CLASS code as the parameter $H_0 r_d$ is not inbuild in the baseline code. The implementation of the additional parameter was done by going into the .pyx file that CLASS has and adding an elif with the name of the parameter, as well as its equation in the derived parameter section. Then the name of the new parameter had to be added to the header file of the background data. After all this, the new parameter $H_0 r_d$ was added to CLASS.

3.2.2 | MontePython

MontePython[4] is a software package designed for Bayesian inference using Markov Chain Monte Carlo (MCMC) methods. MontePython is a widely used cosmological parameter estimation code that combines MCMC techniques with theoretical predictions from cosmological models [22]. This simulator works in conjunction with another simulator as the computation of the theoretical predictions is required for MontePython to work. For this research, CLASS was used to make the theoretical predictions, as discussed in the previous section, while MontePython was responsible for plotting the results of the wCDM models.

This simulator uses Bayesian statistics which is a statistical approach that involves updating the probability of a model based on the data [106]. Bayesian analysis is based on Bayes' theorem [68, 100], which is defined as

$$P(\Theta|\mathcal{D}) = \frac{P(\mathcal{D}|\Theta)P(\Theta)}{P(\mathcal{D})}\,, \tag{3.7}$$

where Θ are the model's free cosmological parameters, $\mathcal{D}$ represents the data, $P(\Theta|\mathcal{D})$ is the posterior probability which is the updated probability of the parameters given the observational data. $P(\mathcal{D}|\Theta)$ represents the likelihood. In other words, it is the probability of observing the data given the parameters. $P(\Theta)$ is known as the prior, meaning that is it the initial probability of the parameters before observing the data. $P(\mathcal{D})$ is the evidence, the overall probability of the data, and it acts as a normalization factor [13].

MCMC generates a number at random and assumes that it has the highest probability [107]. It then chooses the subsequent value and determines if the subsequent value has a better probability after plotting it as a normalisation curve. The value would be regarded as having the highest probability if its probability was higher than that of the initial value [39]. The process was then repeated for the

[4]MontePython can be downloaded using the GitHub link:
https://github.com/brinckmann/montepython_public.git

following value until it had a lower probability than the preceding value. Additionally, this analysis will result in selection criteria that will enable us to make certain judgements [45].

A crucial characteristic of an MCMC is that it converges to a stationary position in which each subsequent element of the chain represents a sample from the distribution; as a result, it converges to the posterior $P(\Theta|\mathcal{D},\mathcal{H})$, where $\mathcal{H}$ represents the hypothesised model [13]. The standard quantities of interest can be calculated in this way. When the complexity of the problem rises, this technique becomes significantly faster since the number of points needed to produce improved estimates in MCMC tends to scale linearly with the number of parameters in the model. A series of delta functions provided are used to approximate the density [58].

$$P(\Theta|\mathcal{D},\mathcal{H}) \simeq \frac{1}{N}\sum_{i=1}^{N}\delta(\Theta-\Theta_i)\,, \tag{3.8}$$

where N denotes the number of points in the chain and Θ_i represents the observable data. Thus, the posterior mean can be evaluated by

$$\langle\Theta\rangle = \int \Theta P(\Theta,\mathcal{H}|\mathcal{D})d\Theta\,, \tag{3.9}$$

$$\langle\Theta\rangle \simeq \frac{1}{N}\sum_{i=1}^{N}\Theta_i\,, \tag{3.10}$$

where $\simeq$ is utilised because the samples Θ_i are generated from the posterior by numerical construction, and where the integral intervals are considered to be $[a,b]$, which can be partitioned into n evenly spaced points depending on the observational sample and size of the nested [13]. Hence, with Simpson's technique, any integral can be estimated as

$$\langle f(\Theta)\rangle = \int f(\Theta)P(f(\Theta),\mathcal{H}|\mathcal{D})df(\Theta)\,, \tag{3.11}$$

$$\langle f(\Theta)\rangle \simeq \frac{1}{N}\sum_{i=1}^{N}f(\Theta_i)\,. \tag{3.12}$$

A representative set of samples from the distribution is drawn over time using a random walk in the parameter space created by the MCMC technique. Hence, in order to create a new point Θ_{i+1} it must depend on the previous point Θ_i. Accepting or rejecting Θ_{i+1} depends on whether this new point better suits the data for the model or not. Since it is possible that, if steps with better probability are accepted, we could be converging towards a local maximum in our parameter

space, we may accept this new step with a specific probability even if it is worse than the previous one [13].

For this project, the Metropolis-Hastings algorithm [91] is used, which proposes new points based on a proposal distribution and accepts/rejects them based on the ratio of posterior probabilities. This means that this kind of method requires starting from a random pivot point θ_i, with an associated posterior probability $p_i = p(\theta_i|\mathcal{D}, \mathcal{H})$. Next, given a proposed distribution $q(\theta_i, \theta_c)$, a candidate variable θ_c is suggested to be employed as a generator of new random points in the series [16]. The likelihood of accepting the new point may then be determined by

$$p(acceptance) := min\left[1, \frac{p_c q(\theta_c, \theta_i)}{p_i q(\theta_i, \theta_c)}\right] . \tag{3.13}$$

The approach simplifies the Metropolis algorithm with a symmetric suggested distribution [91, 46] to be

$$p(acceptance) = min\left[1, \frac{p_c}{p_i}\right] . \tag{3.14}$$

Consequently, the following procedures may be used to describe the whole algorithm [39]:

- 1. Select a random initial condition θ_i in the parameter space, and use Eq. 3.13 to calculate the posterior distribution.
- 2. Create a new candidate in the parameter space based on a proposal distribution, and then use Eq. 3.14 to calculate the associated posterior distribution.
- 3. Using Eq. 3.13 and the Metropolis-Hastings algorithm, accept or reject the new point.
- 4. Reiterate the preceding point in the sequence if the point is rejected.
- 5. Steps 2-4 are repeated until the chain converges which is determined by the Gelman–Rubin criterion [13]).

The Gelman–Rubin diagnostic [112], also known as the Gelman-Rubin convergence diagnostic or $\hat{R}$ statistic, is a method used in Bayesian statistics, which assesses whether multiple MCMC chains have converged to the same distribution. When running MCMC, it is essential to determine if the chains have converged

to the target distribution, meaning that the results are reliable and can be used for statistical inference. The method involves running multiple MCMC chains independently, each initialized with different starting values. The idea is to compare the behaviour of these multiple chains to assess convergence [39]. It measures the variability within each individual chain as well as the variability between the different chains. This is done by first calculating the mean value of an arbitrary chain j,

$$\bar{x}_j = \frac{1}{L}\sum_{i=1}^{L} x_i^{(j)} \,, \tag{3.15}$$

where L is the number of points in the chain. The mean value is calculated for each chain so then the mean of all chains is computed by the equation,

$$\bar{x}_* = \frac{1}{J}\sum_{j=1}^{J} \bar{x}_j \,, \tag{3.16}$$

where J is the total number of chains. Since the mean value of each chain and the mean of the means of all the chains were computed, the variance of the means of the chains could then be calculated,

$$B = \frac{L}{J-1}\sum_{j=1}^{J} (\bar{x}_j - \bar{x}_*)^2 \,. \tag{3.17}$$

Then, across all chains the average variances of the individual chains would be computed using the equation [57]:

$$W = \frac{1}{J}\sum_{j=1}^{J}\left[\frac{1}{L-1}\sum_{i=1}^{L}(x_i^{(j)} - \bar{x}_j)^2\right] \,. \tag{3.18}$$

Therefore, the Gelman-Rubin statistics, $\hat{R}$, is estimated as

$$\hat{R} = \frac{\frac{L-1}{L}W + \frac{1}{L}B}{W} \,. \tag{3.19}$$

In Eq. 3.19, when B tends to zero and L tends to infinity, $\hat{R}$ tends to 1. The Gelman-Rubin statistic $\hat{R}$ compares the estimated between-chain variance to the within-chain variance [112]. If all chains have converged to the same distribution, the between-chain and within-chain variances should be roughly the same, and $\hat{R}$ should be close to 1. If $\hat{R} > 1.1$, it means that the chains have not yet converged, and more iterations or further adjustments may be needed. The disadvantage of this is that it requires running multiple chains, which can increase computational

cost. Also, it assumes that the chains are long enough to represent the stationary distribution, and it might not always detect issues like slow mixing [46]. This analysis is crucial as it ensures that the parameter space has been thoroughly explored and that the results of the analysis are reliable.

After making sure that the MCMC chain has converged, the burn-ins of the chains need to be removed before plotting the results. At the beginning of an MCMC run, the chain may start far from the target distribution. The early samples might not be representative of the desired distribution, as the chain is still exploring the parameter space [16]. This initial phase of the chain is called burn-ins and is important to remove to ensure that the remaining samples used for analysis are drawn from the true stationary distribution, rather than being influenced by the starting conditions. The purpose of burn-in is to allow the chain enough time to converge to the stationary distribution. By discarding these initial samples, the risk of including biased or non-representative samples in your final analysis is minimized. Including samples from the burn-in period in the final analysis could lead to inaccurate estimates of parameters, higher variance, and potentially misleading inferences. The amount of burn-ins that need to be removed depends on the length of the chain. However, it is often suggested to remove roughly 10% to 30% of the chain.

MontePython uses a param file to be able to run an MCMC chain [22]. This file contains the parameters to be varied during the MCMC process, as well as their ranges, priors, and any fixed parameters. The param file starts with the list of the likelihoods that are going to be used in the runs. The likelihoods are the chosen data sets. In this research, they are the PR3, PR4, CC, SN+SH0ES and BAO transverse data sets. Each combination of the data sets requires its own param file. To explore fully the wCDM models, the models are going to be tested with late-time data on its own, to see the results that the wCDM models would produce when they only have information on the late Universe. Since there are four different late-time data combinations, CC and SN+SH0ES will be grouped together, and the models will produce results only on those two data combinations. This is done so that the study of late-time is isolated and the BAO data does not affect the models. Another reason is to then analyse the effect that the BAO data has on the wCDM models with respect to the parameters and how they are shifted, if not at all. Then the models are to be tested with CC, SN+SH0ES and BAO, then, with DESI instead of BAO. This is to compare the two BAO data so that the better BAO data is chosen to be combined with early-time data later on. After that, the wCDM models are tested using only early-time data. This is done so that the two Planck data can be compared. Then, the late-time data of CC and SN+SH0ES are added to the Planck data so that the effects of the late-time

data with the tested models can be analysed without the influence of the BAO data. Finally, the better BAO data will be added.

After the likelihoods have been specified, the parameters are then to be defined. Each parameter is specified with an array containing: the mean value, the minimum value, the maximum value, the standard sigma deviation, the scale and the type of parameter (for instance 'cosmo' for cosmological parameters), 'nuisance' for nuisance parameters, and 'derived' for derived parameters. For CLASS and MontePython, parameters are categorized into three main types: cosmological parameters, derived parameters, and nuisance parameters.

Cosmological parameters are the fundamental parameters that describe the physical properties of the Universe. These parameters are directly varied during the MCMC process to fit observational data. For the ΛCDM model, the cosmological parameters were w_{cdm}, w_b, θ_s, τ_{reio}, A_s and n_s [62, 37]. Since wCDM is an extension of the standard model, the wCDM models use all the six ΛCDM parameters to describe the power spectrum. However, since the wCDM relaxes the assumption that $w = -1$ all throughout the history of the Universe, by turning w into a free parameter, it requires two additional cosmological parameters: w_0; and w_a. The parameter w_0 on its own being a free parameter makes w a constant but different from -1. The parameter w_a being a free parameter, turns w into a dynamical parameter that varies in time depending on the chosen model. The parameter w_0 and w_a are readily in built into CLASS and their default values in CLASS, of w_0 and w_a are fixed values of -1 and 0 respectively. Thus, since the wCDM models, w_0 in the case of the w_0CDM model while both w_0 and w_a for the other five reprametrisation models are varying, they were set to be free parameters by defining w_0 and w_a in the param file as cosmological parameters depending on the model.

Derived parameters are quantities that are not directly varied in the MCMC but are calculated from the cosmological parameters during the analysis [64]. They are important because they often provide more intuitive or direct interpretations of the cosmological model and can be directly compared to observational data. Therefore, for this project, H_0 was taken as a derived parameter.

On the other hand, nuisance parameters are those that are not of direct cosmological interest but are included in the analysis because they describe systematic effects or other influences that can impact the observational data [63]. These parameters are essential for accurately modelling the data and minimizing systematic biases. Hence, the nuisance parameters depend on the chosen data sets. For instance, PR3 and PR4 have different nuisance parameters and SN+SH0ES also

has a nuisance parameter.

After defining the parameters, the cosmo arguments needed to be set. These are parameters passed to CLASS that need to be fixed to non-default values. Since there are five models that have a time-dependent w, and they were implemented using cases. Each model required its own case which contained its equation of state so that it can be taken for the computation of the theoretical prediction made by CLASS. Each case had to be specified using cosmo arguments [64].

Finally, MCMC parameters like the number of steps and jumping factor are also included. In the research, the number of steps was set to 400000, but if the chain converged before all the steps were taken, the run was stopped. The convergence of the chain was determined by the Gelman-Rubin statistics as previously discussed in this Chapter. The jumping factor is a multiplier that influences the step size of the MCMC sampling process for each parameter. It adjusts how far the MCMC sampler "jumps" in the parameter space with each proposed move, directly affecting the convergence speed and acceptance rate of the sampling process [22].

A jumping factor greater than 1 increases the step size, resulting in larger jumps in the parameter space, while a jumping factor less than 1 decreases the step size, resulting in smaller jumps [46]. A well-chosen jumping factor helps achieve a balance between the acceptance rate and the exploration efficiency of the parameter space [22]. A high jumping factor might lead to a low acceptance rate, causing the chain to reject most proposals and thus slow down the convergence. A low jumping factor might result in too small steps, increasing the acceptance rate but slowing down the exploration and mixing of the chain. Selecting the right jumping factor is often done by experimenting with different values and monitoring the acceptance rate of the chain.

The acceptance rate is the percentage of proposed parameter updates that are accepted by the sampler during the chain's evolution. It serves as an important diagnostic metric to evaluate the performance of the MCMC algorithm and helps determine whether the parameter space is being explored efficiently [46]. An ideal acceptance rate is typically around $0.2 - 0.3$, which usually indicates good mixing and efficient sampling. The equation of the acceptance rate is

$$\text{Acceptance rate} = \frac{\text{Total Number of Accepted Steps}}{\text{Total Number of Steps}} . \tag{3.20}$$

If the steps are too large, the proposed points may fall into regions with low likelihood or prior density, leading to a low acceptance rate. If the steps are too small,

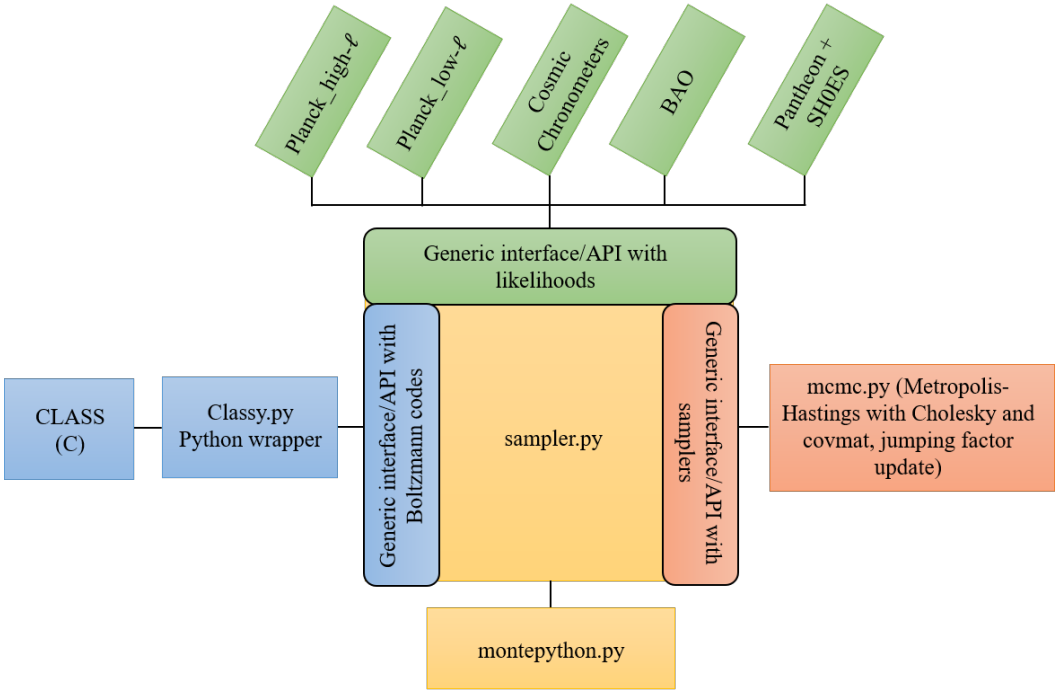

Figure 3.2: A broad picture of how CLASS and MontePython work together using the chosen data sets. [22]

the chain accepts more moves but explores the space slowly, resulting in a high acceptance rate but poor mixing. If the acceptance rate is too low (< 0.2), it suggests that the jumping factor is too large. Consequently, if the acceptance rate is too high ($> 0.3 - 0.5$), it indicates that the jumping factor is too small, and the chain might not be exploring the parameter space effectively [22]. The value of the jumping factor depends on the model and the combination of data sets that the chain has. So, for every run, the acceptance rate was monitored in the log file which Montepython generates. This file updates every time MontePython calculates the Gelman-Rubin statistics for the run. Fig. 3.2 shows pictorially how MontePython and CLASS work together for the achievement of the results of each model. The figure shows that the likelihoods which are determined in the param file, in this case, Planck, CC, SN+ and BAO data sets, are sampled to another simulator in this case CLASS to make the theoretical predictions using Boltzmann equations, according to each model. CLASS has a Python wrapper which makes it interact seamlessly with MontePython which is Python-based. The param file also defines priors for each parameter, reflecting prior beliefs or constraints before considering the new data. Using MCMC, MontePython generates samples from the posterior distribution. This is done by proposing new

sets of parameters, calculating their likelihoods, and deciding whether to accept or reject them based on the Metropolis-Hastings algorithm.

The Planck likelihood was added to the likelihood folder of MontePython and the data of it was added to the data folder of MontePython as they are publicly available. Since DESI data was used in this research, the likelihood had to be coded, as only the data is available publicly. Subsequently, the testing of this new likelihood was required to make sure that it was correctly implemented by comparing the values that the code produced to the values found in the paper. Therefore, the DESI likelihood had to be tested on its own. The DESI data has three different types of data; $\frac{D_M}{r_d}$, $\frac{D_V}{r_d}$ and $\frac{D_H}{r_d}$ so the data and the covariance matrix and each type of data was separated. After loading the data, a for loop was needed and for each type, the code calculated its own values of $\frac{D_M}{r_d}$, $\frac{D_V}{r_d}$ and $\frac{D_H}{r_d}$ by using Eq. 3.3, Eq. 3.4 Eq. 3.2 respectively, so that they would be compared to the observed data that was obtained from DESI, using the equation

$$residuals = data_{calculated} - data_{observed}\,, \tag{3.21}$$

where $data_{calculated}$ is the calculated values of $\frac{D_M}{r_d}$, $\frac{D_V}{r_d}$ and $\frac{D_H}{r_d}$ and $data_{observed}$ is the observed data from DESI. This was needed to be able to compute the χ^2 by using Eq. 3.1. Since DESI on its own does not manage to constrain H_0, the paper uses priors of BBN and $100\theta_s$. The paper defines BBN as $\omega_b = 0.02218 \pm 0.00055$ and $100\theta_s = 1.04109 \pm 0.00030$ [2] so the same values were used for the implementation of these likelihoods in this research. The likelihood was tested by comparing the values produced by the paper to the values that were produced by the implemented likelihood.

For the plotting of the Monte Carlo samples, that MontePython produced, GetDist[5] was used as it is simpler to select which runs need to be plotted as well as overlapping graphs for the ability to compare results [65]. It is also easier to set the number of burnins that were required to be removed and modify the graphs as needed depending on the results that were obtained.

3.3 | Statistical Analysis

To be able to determine which model fits the data better or if the wCDM models fit the observational data better than the standard model, statistical criteria are needed. Akaike Information Criterion (AIC) and Bayesian Information Criterion

[5]The link to the installation of GetDist can be found in the link: https://getdist.readthedocs.io/en/latest/intro.html

(BIC) were taken as measures for how precise each model is compared to the observational data. This is done to more accurately analyse the performance of each model compared to the ΛCDM. AIC [6] was developed by Hirotugu Akaike is represented by the equation,

$$\mathrm{AIC} = -2\ln(L_{\mathrm{MAX}}) + 2n\ , \tag{3.22}$$

where L_{MAX} is the likelihood function's maximum value for each model, data set, and prior combination, and n is the total number of parameters used in the estimate procedure. AIC provides a way to assess the quality of a model relative to other models by considering both the goodness of fit and the complexity of the model. Lower AIC values represent greater performance when compared to combinations of observational data sets. As shown in Eq. 3.22, this analysis penalizes model complexity, specifically the number of parameters (n). This is done because models with more parameters will always fit the data better, potentially leading to overfitting. Therefore, the term $2n$ ensures that the AIC score discourages overly complex models. On the other hand, AIC promotes models with a better fit to the data, specifically higher likelihood values (L_{MAX}). Consequently, the term $-2\ln(L_{\mathrm{MAX}})$ rewards models that better explain the observed data, as higher likelihoods result in lower AIC values.

BIC [97] was developed by Gideon Schwarz and is derived from a Bayesian perspective. The criterion is closely related to AIC but places a stronger emphasis on penalizing complexity compared to AIC. Hence, the BIC is described as

$$\mathrm{BIC} = -2\ln(L_{\mathrm{MAX}}) - n\ln(m)\ , \tag{3.23}$$

where m is the combined sample size for the observational data. Additionally, this variant of the AIC imposes a penalty on models with many parameters to estimate, which is more significant in BIC. The term $n\ln(m)$ grows with both the number of parameters and the number of observations. This means that as the dataset size increases, the penalty for adding parameters becomes larger, discouraging overfitting, resulting in this criterion to penalise the model for it. Similar to the AIC, BIC promotes models that provide a better fit to the data, through the term $-2\ln(L_{\mathrm{MAX}})$

The BIC could be considered as a better indicator of how well AIC performs when applied to observational data due to the clear appearance of the number of points in a data collection, thus imposing a heavier penalty for the number of parameters than AIC which helps prevent overfitting, especially in large datasets. AIC is more suitable when the goal is to identify a model with a good predictive performance, while BIC is often preferred for finding the true model among a set of

candidates. Also, BIC is more conservative than AIC when it comes to adding parameters, often favouring simpler models, especially when the sample size is large. Both AIC and BIC are used to compare different models; the model with the lowest AIC or BIC is typically chosen as the best model.

3.3.1 | Conclusion

For this project, early-time data and late-time data are used, as the wCDM models will be tested using combinations of these data sets to obtain a complete analysis of the results of the models. For the early-time data, Planck data containing CMB data was used, specifically PR3 and PR4. From PR3, the data of low- l TT, low-l EE and high-l TT+TE+EE were chosen, while from PR4, Lollipop of low-l TT and Hillipop of high-l TT+TE+EE were taken. For the late-time data, CC, SN+SH0ES, BAO transverse and DESI BAO data were chosen. After choosing the data sets, simulations are required to test the wCDM parameterizations and to plot the results. CLASS is a Boltzmann code that allows for the precise calculation of the cosmic microwave background anisotropies and it was chosen to make the theoretical predictions of the models. CLASS had to be modified to implement the models that are to be tested using cases as they are not implemented in the code's baseline. MontePython, on the other hand, uses Markov Chain Monte Carlo for parameter inference, to extract cosmological parameters from observational data effectively by analysing the probability of the parameter space and choosing the most likely value using Metropolis-Hastings. MontePython was used in this project to plot the results of the wCDM parametrisation models that were discussed in Chapter 2. Likelihoods of Hillipop, Lollipop and DESI were added to MontePython. MontePython requires a param file which contains information about the parameters. Each model with a particular combination of data sets required its own param file. In the param file, which wCDM model CLASS needs to take was specified and also w_0 and w_a were set to be cosmological parameters depending on the model instead of them being fixed to -1 and 0 which is the default. Now, since the data sets were determined and the simulators in this case CLASS and MontePython, were modified, the results of the reparametrisation models of wCDM were achieved after the chains converged which was determined by Gelman-Rubin statistics. Their plots, that were generated by GetDist, as well as their analysis, are shown and discussed in the next Chapter.

4

Data Analysis

This chapter presents the results derived from the wCDM reparametrisation models. By examining these results, conclusions about the models can be made from the correlations produced between the parameters and how they would correspond to the evolution of the Universe. The assessment of how the models respond to the different observational datasets will be made with respect to the wCDM parameters, the H_0 parameter as well as the σ_8 parameter by addressing the theoretical expectations and their alignment or deviations from the ΛCDM model. This chapter will also emphasize the strengths and limitations of each wCDM model for each data combination that was used.

From the theoretical predictions of each model (w_0CDM, CPL, JBP, GE, BA, OSCILL) made by CLASS, MontePython was able to make corner plots and achieve values using different data combinations. For each model four tables were made that contain the values that were achieved from each model when using different data sets: one table to show the values when using only background data CC + SN+SH0ES + BAO and CC + SN+SH0ES + DESI, another table to show values that were obtained when using early-time data of PR3 and PR4, a third table to show PR3 + CC + SN+SH0ES and PR4 + CC + SN+SH0ES, and a fourth table to show the model when using PR3 + CC + SN+SH0ES + DESI and PR4 + CC + SN+SH0ES + DESI. The tables are split up into 3 sections: the sampled parameters, derived parameters and statistical criteria depending on the chosen data set combinations.

The sampled parameters in the first table are Ω_m, w_0 and w_a (depending on the model) since without early time data, the six ΛCDM parameters cannot be constrained. The sampled parameters for the other three tables of each model contain the six ΛCDM parameters that are ω_b, ω_{cdm}, $100\theta_s$, $\ln(10^{10}A_s)$, n_s and τ_{reio}, which

are the parameters that the standard model uses to describe the CMB power spectrum as discussed in Chapter 2, as well as the additional parameter w_0 for the w_0CDM model and w_0 and w_a for the other five parameterisation models. The second section of all the tables is dedicated to the derived parameters; in the first table the only derived parameter is H_0 as σ_8 cannot be constrained with only late-time data. For the rest of the tables, since early-time data was used, the derived parameter section includes the values for H_0 and σ_8. For these two sections, all of the three tables of each model have the best-fit value and the mean value, and the 1σ deviations of the mean value are also shown. On the other hand, the last section of the tables is the χ^2 statistics; the first column in this section has the name of each statistical criteria, χ^2, ΔAIC and ΔBIC, and the second column has the value for each statistics. The ΔAIC and ΔBIC are the differences between the values of the AIC and BIC of the parameterisation model and the values of the AIC and BIC of the ΛCDM where the values of the ΛCDM model are found in the Appendix. Thus, conclusions about whether or not the model is statistically better than the standard model in cosmology can be made.

Corner plots were used for the assessment of the tested models. Corner plots are a widely used visualization tool in Bayesian statistics and data analysis, and are generated from the MCMC runs with MontePython. It provides a visual summary of the parameter space of the reparametrization model. To create the corner plot, the MCMC samples are marginalized over all parameters except the two being considered in a given 2D plot or the one being considered in the 1D histogram. Marginalization is the process of integrating over the other parameters to focus on the distribution of interest. For each pair of parameters, a 2D contour plot shows the joint probability distribution. The contours often represent regions of 68 % (1σ) and 95 % (2σ) confidence levels. These contours highlight how strongly correlated or independent different parameters are in the wCDM models. The diagonal elements of the corner plot are 1D curves that show the marginalized posterior distributions for each parameter. The peak of the curve indicates the most probable value, while the width gives a sense of the parameter's uncertainty.

Thus, three corner plots for each model were plotted in total to be able to make conclusions about the model and to be able to make conclusions about the recently released data set, PR4, and the previously released data set, PR3, as well as making conclusions on the different BAO data. The first corner plot was generated overlapping the results obtained by the model when late-time data only is used; the grey corner plot shows the wCDM parameterisation model when CC + SN+SH0ES data was used; the red corner plot showing when BAO data was used; and the blue corner plot showing the model when DESI was used. The

second graph was rendered showing two overlapping corner plots of the wCDM parameterizations when only CMB data was used; PR3 shown in red, and PR4 shown in blue, to make conclusions on the model when using only early-time data and to compare the two Planck data. The third corner plot was made by overlapping the results achieved by the model using PR3 + CC + SN+SH0ES represented by a green corner plot, PR4 + CC + SN+SH0ES represented by a grey corner plot, PR3 + CC + SN+SH0ES + DESI shown by a red corner plot and PR4 + CC + SN+SH0ES + DESI shown as a blue corner plot to be able to see the effect that the addition of late-time data without BAO data has on the model and its results as well as the effect the BAO data has on the models.

Each model was tested using only early-time data. However, the chosen wCDM models only affect the late Universe. This means that it was expected that by using only early-time data the models would not be able to be constrained so there would be degeneracies, especially with the parameters of w_0, w_a and H_0. The models require late-time data for them to be constrained properly. The models were tested using only early-time data mainly to compare the two Planck data sets. Also, the data set combinations were tested with the standard model and graphs were also made (these plots can be seen in the Appendix A). In Fig. A.1 it was noticed that the DESI data obtained higher values of Ω_m and lower values of H_0. Also, the posteriors were smaller when DESI was used than when the older BAO data was used, showing that it constrains the data better. Fig. A.2 showed that PR4 had narrower posteriors than the posteriors of PR3 showing that the newer Planck data constrains better than the PR3 data set. These differences were expected to be seen when these data combinations were used in the wCDM parameterisation models.

4.1 | The Constant model

The constant model or the w_0CDM model is a model that takes w to be constant but not necessarily equal to -1. The results that were generated when using this parameterisation can be seen in Table S1, Table S2, Table S3, and Table S4.

Three corner plots were generated for better visualisation of the results shown in Table S1, Table S2, Table S3, and Table S4. Fig. 4.1 shows the constant model when only late-time data was used for the comparison of the different BAO data. As expected, when the DESI data was added, higher values of Ω_m and lower values of H_0 were obtained, meaning that the Universe is expanding at a slower rate. The parameter Ω_m represents the matter density of the Universe. Therefore, a higher value of Ω_m means that the gravitational pull is larger. Thus, more time

Parameters	CC + SN+SH0ES		CC + SN+SH0ES BAO		CC + SN+SH0ES DESI	
	Best-fit	Mean	Best-fit	Mean	Best-fit	Mean
Sampled Parameters						
Ω_m	0.270	$0.270^{+0.052}_{-0.042}$	0.273	$0.274^{+0.013}_{-0.043}$	0.317	$0.318^{+0.011}_{-0.012}$
$w_{0,w0CDM}$	-0.88	$-0.89^{+0.12}_{-0.10}$	-0.888	$-0.894^{+0.043}_{-0.040}$	-1.054	$-1.056^{+0.036}_{-0.034}$
Derived Parameters						
H_0	72.35	72.34 ± 0.88	72.35	$72.33^{+0.86}_{-0.87}$	71.43	$71.46^{+0.81}_{-0.82}$
χ^2 **Statistics**						
χ^2_{min}		1309		1322		1332
ΔAIC		0.91		-4.38		-0.65
ΔBIC		6.37		1.09		4.81

Table S1: The values of the w_0CDM model using only background data obtained from CLASS and MontePython simulations.

Parameters	PR3		PR4	
	Best-fit	Mean	Best-fit	Mean
Sampled Parameters				
ω_b	0.02247	$0.02239^{+0.00015}_{-0.00016}$	0.02229	0.02224 ± 0.00013
ω_{cdm}	0.1191	0.1197 ± 0.0014	0.1184	0.1188 ± 0.0012
$100\theta_s$	1.0420	$1.0419^{+0.00030}_{-0.00031}$	1.0418	1.0418 ± 0.00025
$\ln(10^{10}A_s)$	3.054	$3.042^{+0.016}_{-0.017}$	3.0366	3.0383 ± 0.014
n_s	0.9654	$0.9651^{+0.0043}_{-0.0045}$	0.9691	$0.9674^{+0.0042}_{-0.0041}$
τ_{reio}	0.0574	$0.0592^{+0.0078}_{-0.0087}$	0.0593	$0.0576^{+0.0062}_{-0.0063}$
$w_{0,w0CDM}$	-2.30	$-1.92^{+0.29}_{-0.48}$	-1.24	$-1.14^{+0.20}_{-0.26}$
Derived Parameters				
H_0	115.45	$100.16^{+20.00}_{-10.00}$	75.41	$72.00^{+8.00}_{-7.00}$
σ_8	1.17	$1.07^{+0.14}_{-0.06}$	0.871	$0.840^{+0.071}_{-0.060}$
χ^2 **Statistics**				
χ^2_{min}		2766		30570
ΔAIC		-4.40		1.80
ΔBIC		10.04		9.90

Table S2: The values of the w_0CDM model obtained from the chosen simulations when only Planck data was used.

Parameters	PR3 CC + SN+SH0ES		PR4 CC + SN+SH0ES	
	Best-fit	Mean	Best-fit	Mean
Sampled Parameters				
ω_b	0.02251	0.02252 ± 0.00015	0.02224	0.02235 ± 0.00012
ω_{cdm}	0.1179	0.1185 ± 0.0013	0.11833	0.1176 ± 0.0011
$100\theta_s$	1.04210	1.04207 ± 0.00029	1.04180	1.0420 ± 0.0039
$\ln(10^{10}A_s)$	3.049	$3.050^{+0.014}_{-0.015}$	3.041	3.041 ± 0.014
n_s	0.9705	$0.9693^{+0.0042}_{-0.0047}$	0.9684	0.9703 ± 0.0039
τ_{reio}	0.0577	$0.0583^{+0.0075}_{-0.0073}$	0.0616	0.0594 ± 0.0062
$w_{0,w0CDM}$	-1.034	$-1.053^{+0.026}_{-0.025}$	-1.062	-1.049 ± 0.024
Derived Parameters				
H_0	69.40	$69.80^{+0.67}_{-0.70}$	69.74	69.76 ± 0.66
σ_8	0.816	0.823 ± 0.011	0.823	$0.818^{+0.011}_{-0.010}$
χ^2 **Statistics**				
χ^2_{min}		4107		31900
ΔAIC		-4.44		-1.40
ΔBIC		3.60		6.96

Table S3: The values of the w_0CDM model obtained from the two Planck data when CC and SN+SH0ES data were added.

was required for dark energy to dominate in the Universe and, consequently, more time was required for the Universe to transition from decelerated to accelerated expansion [37]. It is seen that the DESI data also produced lower values of $w_{0,w0CDM}$. While, the addition of the BAO data did not affect the parameters except for constraining the parameters Ω_m and $w_{0,w0CDM}$ better and, as a result, the parameters are more well-defined. There is a correlation between Ω_m and H_0 when DESI or BAO data was added to the CC and SN+SH0ES data while an anti-correlation between Ω_m and $w_{0,w0CDM}$ is seen in all the data combinations. This is expected as if Ω_m increases then the expansion of the Universe is slowed down due to the gravitational attraction [81]. Thus, to counter this effect and match the observational distances, the value of H_0 would need to be higher and, subsequently, the value of $w_{0,w0CDM}$ would be more negative. There is another anti-correlation between H_0 and $w_{0,w0CDM}$ seen when DESI or BAO data was added to the late-time data. At late times, when the Universe becomes radiation dominated, the equation of state w affects H_0 the most, such that the more negative $w = w_{0,w0CDM}$ is, the higher the value of H_0 will be.

When looking at Table S1 it can be concluded that the w_0CDM model does not limit to the ΛCDM model regardless of the inclusion of the DESI and BAO data

Parameters	PR3 CC + SN+SH0ES + DESI		PR4 CC + SN+SH0ES + DESI	
	Best-fit	Mean	Best-fit	Mean
Sampled Parameters				
ω_b	0.02258	0.02256 ± 0.00014	0.02245	0.02236 ± 0.00012
ω_{cdm}	0.1176	$0.1180^{+0.0011}_{-0.0010}$	0.11704	$0.11742^{+0.00092}_{-0.00090}$
$100\theta_s$	1.04220	1.04210 ± 0.00029	1.04200	$1.04200^{+0.00024}_{-0.00025}$
$\ln(10^{10}A_s)$	3.056	$3.054^{+0.015}_{-0.020}$	3.041	3.040 ± 0.015
n_s	0.9747	$0.97033^{+0.0040}_{-0.0039}$	0.9709	$0.9707^{+0.0035}_{-0.0036}$
τ_{reio}	0.0623	$0.0606^{+0.0073}_{-0.0099}$	0.0614	$0.0597^{+0.0063}_{-0.0067}$
$w_{0,w0CDM}$	-1.038	$-1.049^{+0.026}_{-0.024}$	-1.043	-1.046 ± 0.024
Derived Parameters				
H_0	69.70	69.86 ± 0.61	69.89	$69.76^{+0.63}_{-0.62}$
σ_8	0.820	$0.823^{+0.011}_{-0.013}$	0.813	0.816 ± 0.010
χ^2 **Statistics**				
χ^2_{min}		4122		31920
ΔAIC		-3.24		-1.00
ΔBIC		4.80		7.36

Table S4: The values of the w_0CDM model obtained from the two Planck data when DESI was added to the CC and SN+SH0ES data.

as it can be seen that $w_{0,w0CDM}$ is not 1σ away from -1 which is the value of the standard model. It can be noticed that the uncertainties of $w_{0,w0CDM}$ are larger when any BAO data is not included. This is to be expected because the parameter varies only at the late Universe so the more late-time data it has the better the data can constrain the model. The value of H_0 in all the late-time data combinations is within the expected range of past research which estimates that the value of the parameter is between $67 - 75$ Km s^{-1} Mpc^{-1} [2, 90, 118, 3, 87]. The uncertainties of H_0 are small which was expected as wCDM parameterization models require late-time data for the models to be constrained. The constant model fits the data of CC + SN+SH0ES + DESI and CC + SN+SH0ES + BAO better than the ΛCDM model when the AIC criteria was taken. However, in the case of the BIC criteria, the standard model is statistically better. Between the two data set combinations that contain BAO data, the constant model seems to fit the data combination that contains the older BAO data than the DESI data. In Fig. 4.1 it can be seen that the posteriors of the w_0CDM model when DESI was included are the smallest out of the three overlapping corner plots. Smaller posteriors indicate that the parameter estimates for the variables are well-constrained, meaning the data provides strong information to pinpoint the parameter values with little uncertainty. In the case of corner plots [107], this means the posterior distributions

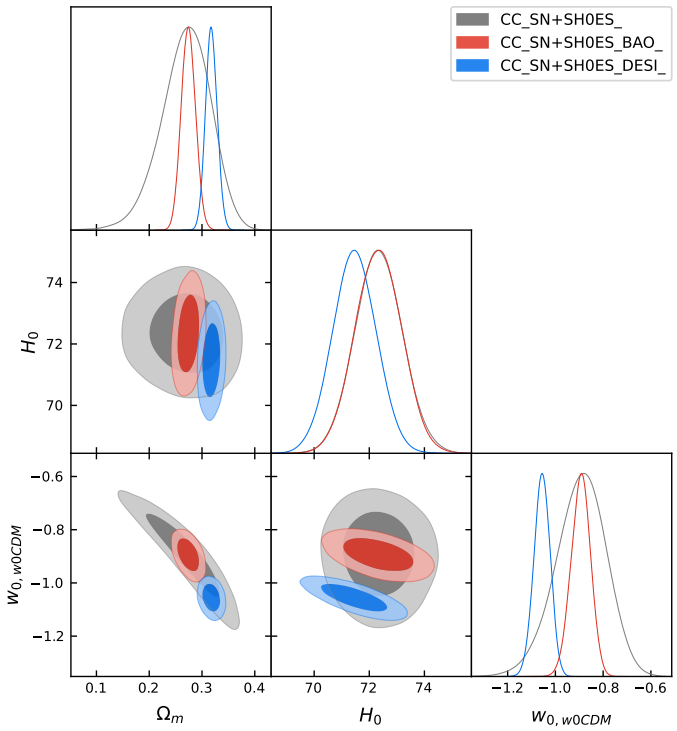

Figure 4.1: Three overlapping corner plots showing the constant model when only using late-time data. The grey corner plot shows when CC + SN+SH0ES data was used, the red corner plot shows the parameterisation when CC + SN+SH0ES + BAO was used and the blue corner plot shows the model when CC + SN+SH0ES + DESI was used.

for the parameters are narrow and peaked, which can result from strong prior information or highly informative data. This means that the DESI data constrains the model better than the previously released BAO data. Therefore, the DESI data will be used instead of the older BAO data. It can also be seen that the posteriors that were obtained with the CC + SN+SH0ES + DESI data combination and the CC + SN+SH0ES data combination are on top of each other. This means that there are no tensions between the datasets, as the posteriors are 1σ away from each other and the rest of the wCDM models are expected to follow this trend.

We now move on to comparing the two Planck data sets, PR4 and PR3. Fig. 4.2 was generated to show the constant model when only early-time data was used. By comparing the two CMB data sets, it can be seen that the area of the 2D off-diagonal panels is significantly smaller for PR4 than for PR3. Smaller confidence regions in the off-diagonal panels often result in a weaker correlation between

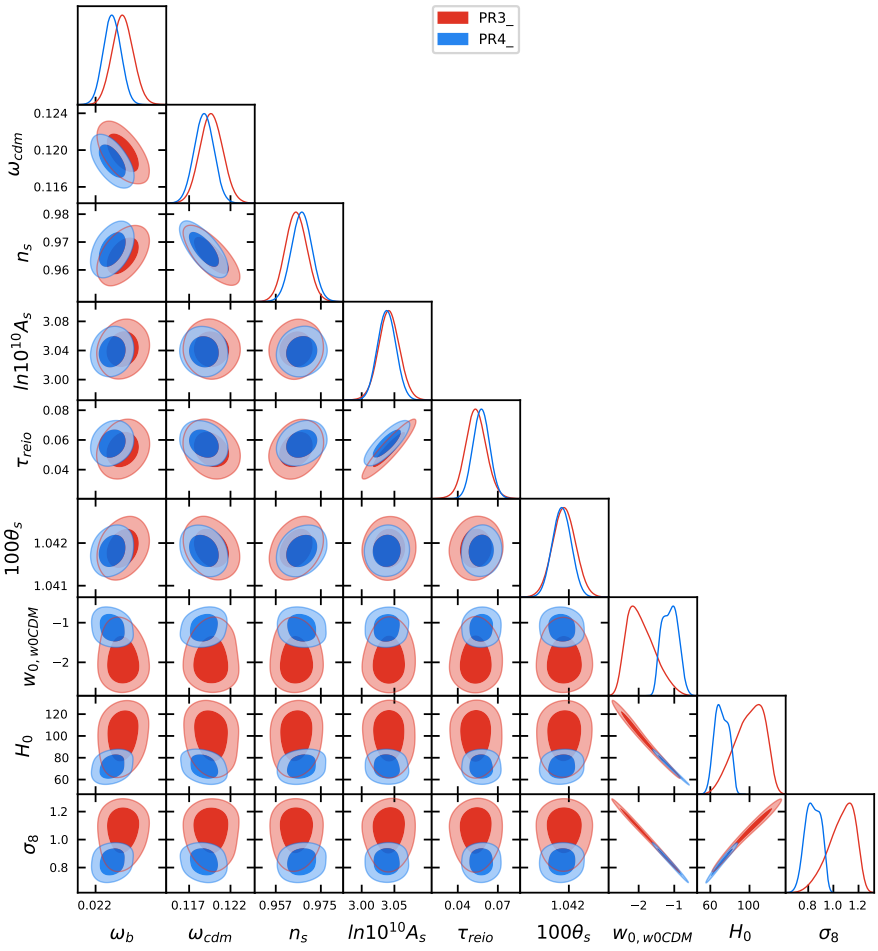

Figure 4.2: A graph of the w_0CDM model with PR3 and PR4 alone seen in red and blue respectively.

the variables [107]. This means that there is less dependency or relationship between the variables being plotted against each other. Similar to DESI, since PR4 has smaller posteriors, the newer CMB data set constrains the model better than PR3. Also similar to the previous graph, the posteriors that were obtained from the newer Planck data intersect the posteriors that were retrieved from the previously released Planck data in a way that they show that the newer Planck data is 1σ away from PR3. Subsequently, there are no tensions between the two Planck datasets. Fig. 4.2 also shows that PR4 obtained lower values of ω_b and ω_{cdm} while higher values of n_s and τ_{reio} than PR3. The parameter ω_b represents the physical density of baryonic matter [10]. Thus, a lower value of ω_b reduces the abundance of light elements like helium and deuterium formed in the early Universe, as there are fewer baryons available for nuclear reactions. Baryons enhance the odd-numbered acoustic peaks in the CMB temperature power spectrum due to their gravitational coupling with photons [81]. Baryons play a key role in the formation of galaxies and clusters. Lower ω_b results in less baryonic matter, affecting star formation rates and the distribution of gas in galaxies. The parameter ω_{cdm} represents the physical density of cold dark matter. Therefore, a lower ω_{cdm} reduces the amount of dark matter available, weakening the gravitational potential wells [37]. This leads to a slower growth of structures, leading to less clustering. A higher value of n_s amplifies small-scale density perturbations, leading to increased clustering of matter on small scales and more efficient galaxy and cluster formation [10]. The optical depth to reionization, τ_{reio}, quantifies the fraction of CMB photons that were scattered by free electrons during the reionization epoch. A higher τ_{reio} implies earlier reionization, likely driven by more abundant or more efficient ionizing sources such as early stars, galaxies, or quasars [5]. Discrepancies are seen in the two 1D curves for the $w_{0,w0CDM}$, H_0 and σ_8 parameters as well as degeneracies when the recently released Planck data was used. The degeneracies with the three parameters show that there is one highest peak which is the most likely value of the parameters. However, the other peak shows that there is another possible value that is less likely. $w_{0,w0CDM}$ and H_0 are nearly perfectly anti-correlated and H_0 and σ_8 are almost perfectly correlated in both data sets. Since H_0 and $w_{0,w0CDM}$ are anti-correlated with each other and H_0 and σ_8 are correlated then, $w_{0,w0CDM}$ and σ_8 are almost perfectly anti-correlated with each other as seen in Fig. 4.2.

When comparing the values in Table S2, the value of $w_{0,w0CDM}$ using the PR4 data set is 1σ away from -1 which is the assumed value in the ΛCDM model. Hence, the constant parameterisation limits to the standard model when the newer Planck data was used. Unfortunately, this is not the case when the previously released Planck data set was used, as $w_{0,w0CDM}$ is not 1σ away from -1. The value of H_0 with the recently released data set agrees with past research.

However, this is not the case when the older Planck data set was taken, as the value of H_0 is higher than the expected range and the uncertainties of this parameter are significantly larger than in PR4.

In past research, the value of σ_8 varies depending on which data set is used. Large-scale structure surveys such as KiDS [88] found slightly lower values of σ_8, around $0.75 - 0.80$ while higher values were found in the DESI survey [2] varying between $0.80 - 0.84$. Planck 2018 [5] obtained a value for σ_8 of 0.811 ± 0.006. Hence, from Table S2, it can be seen that the value of σ_8 that was obtained from the previously released CMB data set is higher than the expected range which is $0.7 - 0.9$ while the value of σ_8 from the newer Planck data is within the expected range. When looking at the values that were obtained from the AIC and BIC criteria, it can be seen that the constant model only achieved one negative value which was when PR3 was used and the AIC criteria was taken. Only that time was the w_0CDM model statistically better than the standard model. The rest of the ΔAIC and ΔBIC show that the ΛCDM model fits the data better than the constant reparameterisation. The AIC shows that PR3 is statistically better than PR4 while the BIC shows that PR4 is statistically better.

Now, we add the late-time data of CC + SN+SH0ES to the previous early-time data results to produce results that should be more constrained. The results are shown pictorially in a graph seen in Fig. 4.3 showing two overlapping corner plots. Without the need for the BAO data, CC and SN+SH0ES managed to constrain the w_0CDM parametrisation as unlike the previous graph, no degeneracies are seen in the parameters of H_0, σ_8 and $w_{0,w0CDM}$. In fact, the additional data was enough to remove any differences that there were with the H_0 and $w_{0,w0CDM}$ parameters, between the two Planck data sets, such that now the 1D curves overlap each other. The anti-correlation between $w_{0,w0CDM}$ and H_0 is still preserved but it is less defined than in the previous plot. Also, the correlation between H_0 and σ_8 and the anti-correlation between σ_8 and $w_{0,w0CDM}$ are also still preserved from the previous graph although they are also less defined. There are now differences in the value of $\ln(10^{10}A_s)$ when different Planck data was used that was not there when the early-time data was used on their own. On the other hand, the CC and SH+SH0ES data shifted the values of n_s and τ_{reio} such that the differences in their values when using the two Planck data decreased. However, PR4 constrained the τ_{reio} parameter better than PR3, as PR4 has a slightly narrower 1D curve than PR3.

The addition of the DESI only affected slightly the results when PR3 was used. The parameters ω_{cdm} and n_s were pushed to slightly higher and lower values, respectively when DESI was included. For the rest of the parameters the 1D curves

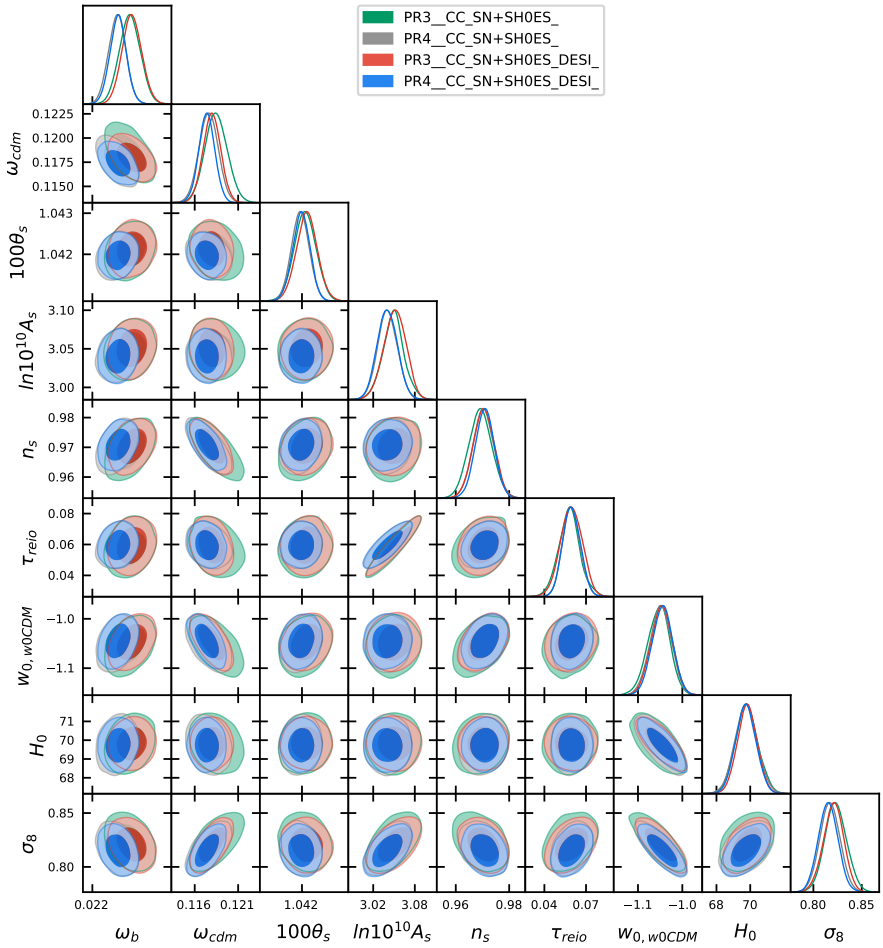

Figure 4.3: A graph showing the constant model when CC + SN+SH0ES was used in conjunction with one of the Planck data sets; PR3 seen in the green corner plot or PR4 seen in the grey corner plot. Then CC + SN+SH0ES + DESI was used together with; PR3 seen in the red corner plot or PR4 seen in the blue corner plot.

of PR3 + CC + SN+SH0ES seen in green overlap the 1D curves of PR3 + CC + SN+SH0ES + DESI seen in red. On the other hand, the DESI data did not seem to affect the newer CMB data, as the 1D curves of PR4 + CC + SN+SH0ES seen in grey overlap the 1D curves of PR4 + CC + SN+SH0ES + DESI seen in blue. Even for $w_{0,w0CDM}$, $w_{a,w0CDM}$, H_0 and σ_8, the DESI data did not affect the constant model despite the fact that when only late-time data was used the DESI data in Fig. 4.1, the values of H_0 and $w_{0,w0CDM}$ were pushed to lower values. Similar to the previous plot, the posteriors are smaller for when the recently released early-time data was used than when the previously released data set was used. This shows that the PR4 data set is more constrained and more well-defined despite the late-time data of CC and SH+SH0ES being added to the two Planck data. Also, the DESI data constrained the data even more by obtaining smaller posteriors and so the w_0CDM model obtained the smallest posteriors when the PR4 + CC + SN+SH0ES + DESI data combinations was taken. Also, as seen in the previous two graphs, Fig. 4.3 shows the posteriors to be overlapping or intersecting each other, showing that with the constant model there are no tensions with the datasets.

When looking at Table S3 and Table S4, it can be seen that the w_0CDM parameterisation is no longer 1σ away from the ΛCDM model when late-time data was added. The value of H_0 for the data combinations is around 69 Km $s^{-1}Mpc^{-1}$, showing that the CC and SH0ES lowered slightly the values of H_0 and σ_8 that were obtained when only using early-time. In the case of PR4 + CC + SN+SH0ES, the addition of the late-time data lessened the uncertainties of H_0 and σ_8 parameters, showing that with the additional data, the recently released Planck data is well-defined for that parameter. When looking at the AIC and BIC in Table S3 it can be concluded that for the AIC and BIC for all data combinations that were used, the w_0CDM model is statistically better than the ΛCDM model as all the four values are negative. This is not the case for the BIC as positive values are seen, meaning that when taking the BIC criteria, the standard model in cosmology fits the data better than this parameterisation model. It also can be noted that the AIC and BIC are lower for the PR3 + CC + SN+SH0ES data combination than for the other data combinations, showing that the w_0CDM fit the data better when the PR3 model was used than when PR4 was used and when DESI data is not included. When comparing the values of the statistical criteria that were obtained in Table S2 to Table S2, as expected the values show that the w_0CDM model fit the data better when late-time data was added than when only early-time data was used. This is due to the w_0CDM parameterisation being more constrained when more data is sampled, and so the model now has information on the late-time Universe.

Parameters	CC + SN+SH0ES		CC + SN+SH0ES BAO		CC + SN+SH0ES DESI	
	Best-fit	Mean	Best-fit	Mean	Best-fit	Mean
Sampled Parameters						
Ω_m	0.12	$0.26^{+0.11}_{-0.06}$	0.274	$0.273^{+0.017}_{-0.016}$	0.326	$0.326^{+0.011}_{-0.012}$
$w_{0,CPL}$	-0.81	$-0.88^{+0.12}_{-0.09}$	-0.902	$-0.895^{+0.074}_{-0.089}$	-0.857	$-0.861^{+0.081}_{-0.085}$
$w_{a,CPL}$	0.62	$-0.14^{+1.10}_{-0.29}$	0.08	$0.00^{+0.60}_{-0.49}$	-1.14	$-1.14^{+0.49}_{-0.43}$
Derived Parameters						
H_0	72.46	$72.31^{+0.92}_{-0.91}$	72.27	$72.36^{+0.90}_{-0.87}$	71.67	$71.68^{+0.79}_{-0.80}$
χ^2 **Statistics**						
χ^2_{min}	1309		1322		1325	
ΔAIC	0.63		-2.39		-5.69	
ΔBIC	13.55		8.54		5.24	

Table S5: The CPL values using only CC + SN+SH0ES + BAO without any early time data.

4.2 | Linear model

Now taking a look at the case if w has a linear form, known as the CPL model, the values obtained by this model when sampling it through CLASS and MCMC are shown in Table S5, Table S6, Table S7, and Table S8. The tables show the best-fit and mean value of the sampled and derived parameters and also the χ^2 statistics.

A graph showing three overlapping corner plots when taking the linear model when only late-time data was used was generated, seen in Fig. 4.4. Similar to the previous model, the DESI data produced higher values of Ω_m and lower values of H_0 and $w_{a,CPL}$. The value of $w_{0,CPL}$ is slightly lowered when the BAO data was used. When the older BAO data was used, it made the parameter Ω_m more well-defined as the CC and SN+SH0ES data alone were not able to constrain the parameter when the CPL model was taken. This is expected due to the fact that the CPL parameterisation affects the late Universe so the additional late-time data would help constrain the model better. The older BAO data did not make any differences with the H_0 parameter while constraining more the $w_{a,CPL}$. Correlations are seen in Fig. 4.4, between H_0 and Ω_m when BAO or DESI was added to the late-time data, which was also seen in the previous model, but unlike the linear model, instead of an anti-correlation between $w_{0,CPL}$ and Ω_m a correlation is seen between them. This is due to the equation of state being different for the linear model than for the constant model. As discussed in Chapter 2, the linear model, $w_{0,CPL}$ represents the value of w at current times while $w_{a,CPL}$ is responsi-

Parameters	PR3		PR4	
	Best-fit	Mean	Best-fit	Mean
Sampled Parameters				
ω_b	0.022498	0.022379 ± 0.00016	0.02218	0.02225 ± 0.00013
ω_{cdm}	0.1188	0.1198 ± 0.0014	0.1191	0.1187 ± 0.0012
$100\theta_s$	1.0418	1.0419 ± 0.00031	1.04170	1.04180 ± 0.00025
$\ln(10^{10} A_s)$	3.0499	3.043 ± 0.016	3.036	$3.039^{+0.014}_{-0.015}$
n_s	0.9661	0.9647 ± 0.0044	0.9680	0.9677 ± 0.0041
τ_{reio}	0.0582	0.0538 ± 0.0078	0.0565	$0.0581^{+0.0060}_{-0.0068}$
$w_{0,CPL}$	-1.01	$-1.01^{+0.30}_{-0.44}$	-0.93	$-1.23^{+0.16}_{-0.22}$
$w_{a,CPL}$	-3.09	$-1.40^{+2.90}_{-1.20}$	-0.58	-0.05 ± 0.39
Derived Parameters				
H_0	87.88	$77.00^{+9.00}_{-10.00}$	69.74	$74.84^{+7.74}_{-7.40}$
σ_8	0.983	$0.907^{+0.074}_{-0.073}$	0.830	$0.87^{+26.40}_{-0.17}$
χ^2 **Statistics**				
χ^2_{min}		2766		30570
ΔAIC		-3.08		2.80
ΔBIC		13.00		19.41

Table S6: The values of the CPL model that were obtained from CLASS and MontePython using PR3 or PR4.

ble for the rate at which the value of w changes from early-time to current times. Therefore, the higher the value of Ω_m is, the higher the value of H_0 had to be at early times to counteract the increase in matter in the Universe, and so in the early Universe, w had to have a lower value. Thus, the value of $w_{a,CPL}$ needs to be more negative for the value of w to be equal to $w_{0,CPL}$ resulting in an anti-correlation between $w_{a,CPL}$ and Ω_m as seen in Fig. 4.4 in all the late-time data combinations. Due to this anti-correlation, a correlation between $w_{0,CPL}$ and Ω_m is obtained when CC + SN+SH0ES + DESI or CC + SN+SH0ES + BAO data combination was used, instead of an anti-correlation like the previous model. Similar to the previous model, an anti-correlation between $w_{0,CPL}$ and H_0 is seen in the CPL model when CC + SN+SH0ES + DESI and CC + SN+SH0ES + BAO were used. There is also another anti-correlation between the parameters $w_{a,CPL}$ and $w_{0,CPL}$ when DESI or BAO data was used. This is because of the equation of w of the linear parameterisation, from the equation if $w_{0,CPL}$ has a higher value then $w_{a,CPL}$ needs to be more negative as the gradient of w from early-times to current times would be higher.

From Table S5, it can be seen that when CC + SN+SH0ES + BAO was used, the CPL model achieved a value of $w_{a,CPL}$ that was 0, which is exactly the value of

Parameters	PR3 CC + SN+SH0ES		PR4 CC + SN+SH0ES	
	Best-fit	Mean	Best-fit	Mean
Sampled Parameters				
ω_b	0.02247	0.02246 ± 0.00015	0.02238	0.02232 ± 0.00012
ω_{cdm}	0.1195	0.1193 ± 0.0013	0.1177	0.1180 ± 0.0011
$100\theta_s$	1.04190	$1.04200^{+0.00031}_{-0.00030}$	1.0420	1.04191 ± 0.00026
$\ln(10^{10}A_s)$	3.051	$3.047^{+0.017}_{-0.019}$	3.043	3.038 ± 0.014
n_s	0.9680	0.9672 ± 0.0044	0.9695	0.9695 ± 0.0038
τ_{reio}	0.0574	$0.0561^{+0.0080}_{-0.0092}$	0.0579	$0.0585^{+0.0058}_{-0.0066}$
$w_{0,CPL}$	-0.829	$-0.816^{+0.078}_{-0.064}$	-0.745	-0.766 ± 0.081
$w_{a,CPL}$	2.23	$2.12^{+0.74}_{-0.66}$	-1.32	$-1.29^{+0.42}_{-0.36}$
Derived Parameters				
H_0	71.65	$70.97^{+0.71}_{-0.74}$	70.40	70.57 ± 0.69
σ_8	0.856	$0.846^{+0.013}_{-0.012}$	0.830	$0.832^{+0.010}_{-0.011}$
χ^2 **Statistics**				
χ^2_{min}		4089		31890
ΔAIC		-20.16		-14.40
ΔBIC		-4.08		2.32

Table S7: The values of the CPL model when using PR3 and PR4 with CC and SN+SH0ES data.

the standard model, when CC + SN+SH0ES + DESI was used the CPL model achieved a value of $w_{a,CPL}$ that was far away from the standard model with a value of -1.14 while when only CC + SN+SH0ES was used, $w_{a,CPL}$ is 1σ away from the value of the standard model. This was expected, as in the DESI paper [2], when the CPL model was tested with the data, it did not limit to the ΛCDM model as it obtained a value of < -1.32 for the w_a parameter. Also, the value of $w_{0,CPL}$ is not 1σ away from -1 for all data combinations. With the AIC criteria, the CPL model is statistically better than the standard model when CC + SN+SH0ES + DESI and when CC + SN+SH0ES + BAO were used, but for the BIC criteria, the standard model is statistically better. When comparing the two data combinations, the CPL model fits the CC + SN+SH0ES + DESI data better than the other data combinations. Also, when comparing the posteriors of the CPL model when CC + SN+SH0ES + DESI and when CC + SN+SH0ES + BAO data combinations were used, it shows that the data combination that contains the DESI data obtained smaller posteriors than the previous BAO data. This means that the DESI data constrains the linear model better than the older BAO data. Subsequently, the DESI data will be used for the BAO data instead of the previously released BAO data. Following the trend of the constant model, the

Parameters	PR3 CC + SN+SH0ES + DESI		PR4 CC + SN+SH0ES + DESI	
	Best-fit	Mean	Best-fit	Mean
Sampled Parameters				
ω_b	0.02250	0.02244 ± 0.00014	0.02222	0.02228 ± 0.00012
ω_{cdm}	0.1202	$0.1197^{+0.0012}_{-0.0011}$	0.1184	0.1187 ± 0.0010
$100\theta_s$	1.04190	1.04200 ± 0.00030	1.04190	$1.04180^{+0.00025}_{-0.00023}$
$\ln(10^{10}A_s)$	3.036	$3.046^{+0.016}_{-0.017}$	3.036	$3.038^{+0.014}_{-0.015}$
n_s	0.9668	$0.9662^{+0.0037}_{-0.0043}$	0.9677	$0.9677^{+0.0039}_{-0.0037}$
τ_{reio}	0.0524	$0.0555^{+0.0075}_{-0.0081}$	0.0546	$0.0575^{+0.0059}_{-0.0066}$
$w_{0,w0CDM}$	-0.854	$-0.848^{+0.066}_{-0.074}$	-0.854	$-0.858^{+0.060}_{-0.066}$
$w_{a,CPL}$	-0.90	$-0.93^{+0.37}_{-0.27}$	-0.84	$-0.84^{+0.32}_{-0.24}$
Derived Parameters				
H_0	69.76	$69.91^{+0.63}_{-0.62}$	69.78	$69.77^{+0.58}_{-0.61}$
σ_8	0.824	$0.836^{+0.012}_{-0.013}$	0.826	$0.828^{+0.011}_{-0.010}$
χ^2 **Statistics**				
χ^2_{min}		4111		31910
ΔAIC		-12.08		-8.20
ΔBIC		4.00		8.52

Table S8: Values of the linear model obtained from the two Planck data with CC, SN+SH0ES and DESI data.

graph shows that there are no tensions between the CC + SN+SH0ES with the CC + SN+SH0ES + DESI as the posteriors that were achieved from when DESI was added are found to be on top of the posteriors that were calculated when the CC + SN+SH0ES data was used on its own.

For the analysis of the two Planck likelihoods, Fig. 4.5 showing two corner plots of the linear model when only early-time data was plotted. At first glance, it can be pointed out that degeneracies are seen with the parameters of $w_{0,CPL}$ and $w_{a,CPL}$ in both CMB data sets, showing that early-time data is not enough to constrain the linear model. This was expected as discussed in Chapter 2; the CPL model varies w in the late Universe while during the early Universe, the w parameter is constant. So only having early-time data would not be able to make correct predictions of the model as it would have missing information regarding the late Universe. Consequently, the linear parameterisation requires late-time data of the $w_{0,CPL}$ and $w_{a,CPL}$ parameters to be constrained. Unlike in the previous model, no degeneracies can be seen with the parameters of H_0 and σ_8 as their 1D curves are well-defined. Higher values of ω_b and ω_{cdm} are seen for the older dataset when compared to the newer data set. As for the parameters n_s and τ_{reio}, the PR4

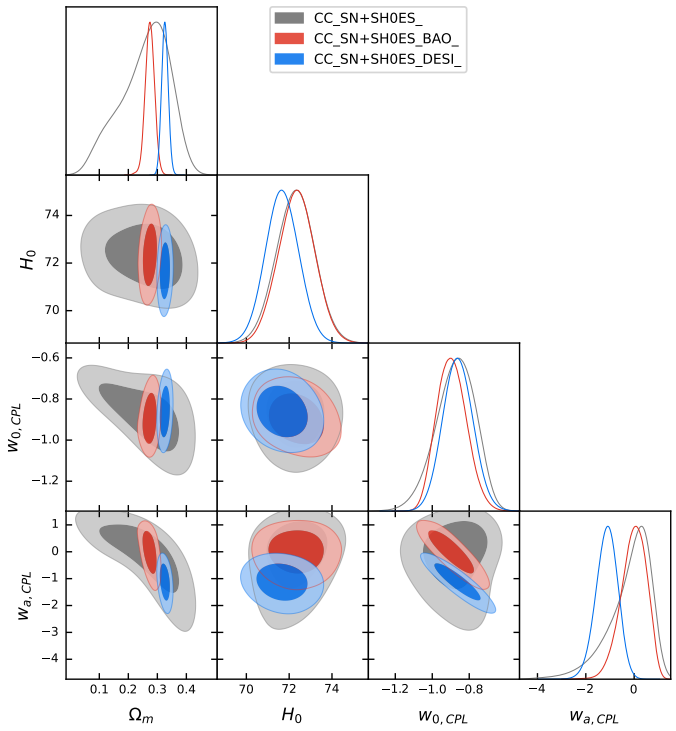

Figure 4.4: A graph of the linear model when taking the two late-time data combinations only made with GetDist. The CC + SN+SH0ES data set is shown in the grey corner plot, the CC + SN+SH0ES + BAO data set is shown in the red corner plot while the CC + SN+SH0ES + DESI data set is shown in the blue corner plot.

data obtained higher values. The parameters $100\theta_s$ and $\ln(10^{10}A_s)$ are nearly the same for the two data sets. Following the trend of the linear model, a strong correlation can be seen between H_0 and σ_8 in both Planck data sets. However, the anti-correlation between $w_{0,CPL}$ and $w_{a,CPL}$ is only seen with PR3, while both CMB data sets show an anti-correlation between $w_{0,CPL}$ and H_0. Contrary to the w_0CDM model, the CPL model does not have anti-correlations between H_0 and $w_{0,CPL}$ and between $w_{0,CPL}$ and σ_8 which were seen in the constant model. When comparing the posteriors of the linear model from the two Planck datasets, the PR4 dataset obtained smaller posteriors than when PR3 was used, and the posteriors overlap each other. This means that the PR4 constrains the linear model better, and PR4 is 1σ away from PR3, meaning that there are no tensions between the datasets, which is what was seen in the constant model.

From Table S6, it can be noted that when PR3 was used, the linear model limits to the ΛCDM model as both values of $w_{0,CPL}$ and $w_{a,CPL}$ are 1σ away from -1

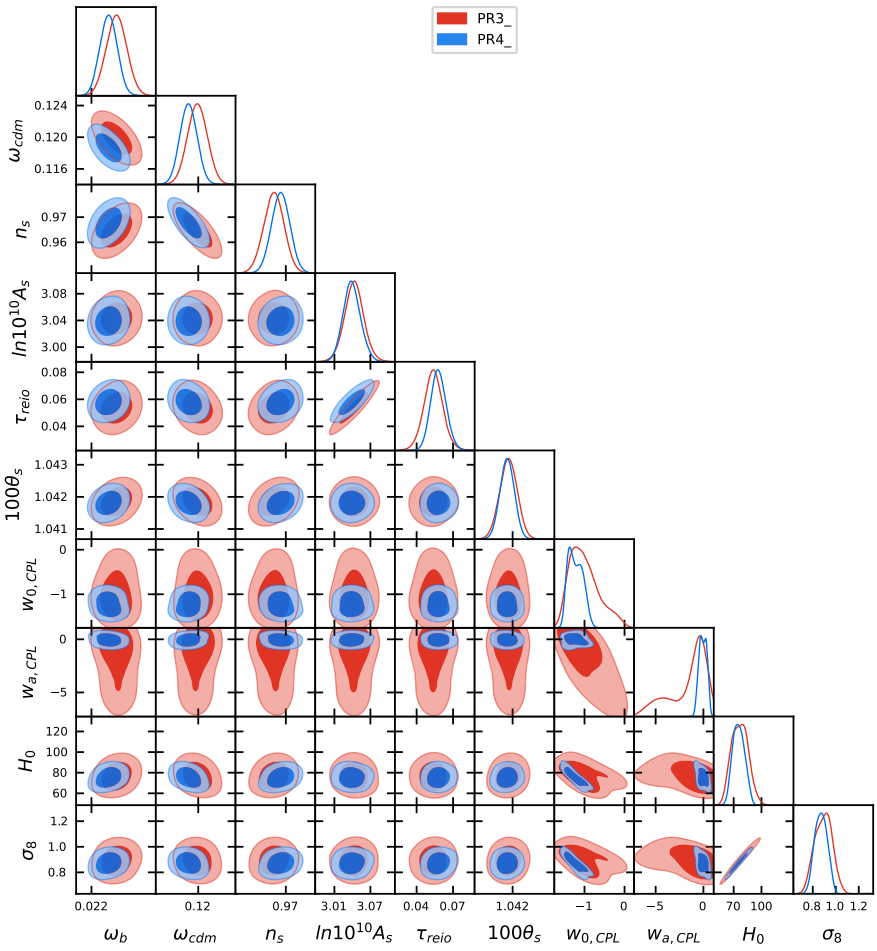

Figure 4.5: A graph showing the CPL model when using only the two Planck CMB data. The red corner plot shows when the PR3 was used and the blue corner shows when the PR4 was used.

and 0 respectively, which are the values of the ΛCDM model. However, when the newer Planck data was used the CPL model no longer limits to the standard model as only $w_{a,CPL}$ is 1σ away from 0. Large uncertainties are seen for the parameters H_0 and σ_8, and the values of these two parameters are outside the expected range of values obtained from past research when the previously released data set was used. On the other hand, when the newer CMB data set was used, both H_0 and σ_8 are within the range of past research. When comparing the AIC and BIC of the CPL model to the AIC and BIC of the ΛCDM model, only one negative value was achieved which was when the PR3 was used and the AIC criteria was taken. This shows that only in that case was the linear model statistically better than the standard model. Otherwise, the values show that the standard model fits the data better than the linear model. Then by comparing the four values of ΔAIC and ΔBIC, it can be concluded that the CPL parameterisation fits the PR3 data better than the PR4 data.

Then, the late-time data sets, CC and SN+SH0ES, were added to the Planck data seen in Fig. 4.6 so that the linear model has information on the late Universe for more accurate values of the parameters. When PR4 was used, the CPL model produced lower values of ω_b, ω_{cdm}, $100\theta_s$ and $\ln(10^{10}A_s)$ and higher values of n_s. The recently released Planck data set helped constrain the τ_{reio} parameter better than when PR3 data was used, as a narrower 1D curve is seen when PR4 was used. When looking at the $w_{0,CPL}$ and $w_{a,CPL}$, it can be seen that the linear model obtained degeneracies when the previously released CMB data was used, as two peaks are seen in the parameters' 1D curves. This means that the addition of the CC and SN+SH0ES data was not enough to constrain the model and remove the degeneracies that were seen in the previous model when only early-time data was used. The curves show that the largest peak shows the most probable values of $w_{0,CPL}$ and $w_{a,CPL}$. However, the smaller peak shows that there are other possible values of $w_{0,CPL}$ and $w_{a,CPL}$ which are not as likely, but the possibility is high enough that there are uncertainties with the value of these two parameters. This uncertainty is not seen when PR4 was used, as one peak is seen in the two parameters, showing clearly which value of $w_{0,CPL}$ and $w_{a,CPL}$ the CPL model predicts. This means that when the PR4 data was used, the addition of the CC and SN+SH0ES data was enough to constrain the linear model and remove the degeneracies seen in the previous plot. When PR4 data was used, the CPL model obtained a lower value of $w_{a,CPL}$ and a higher value of $w_{0,CPL}$. Two overlapping 1D curves are seen indicating that the linear model obtained the same H_0 parameter even though the Planck data was updated. For the σ_8 parameter, when the recently released CMB data was used, the CPL model achieved a lower value than when the PR3 data was used.

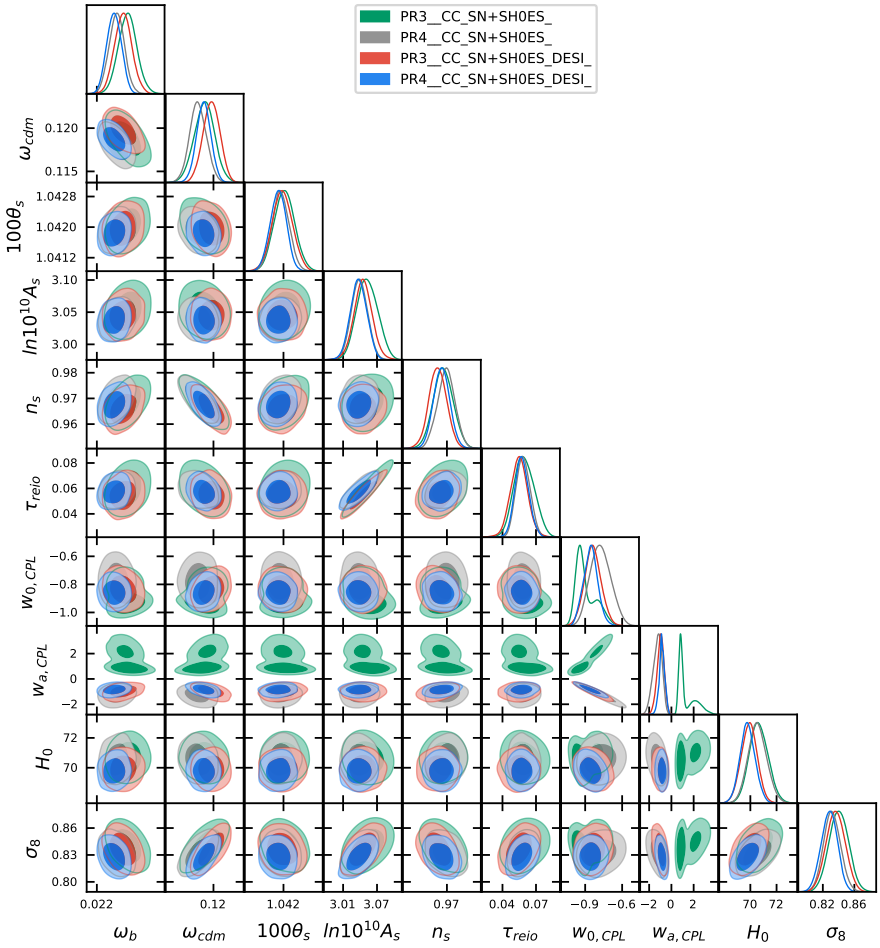

Figure 4.6: A graph of the CPL model using the two Planck early time data while also using combinations of late time data. The green corner plot shows the CPL model when PR3 + CC + SN+SH0ES data was used, and the grey corner plot shows the linear model when PR4 + CC + SN+SH0ES data was used. The red corner plot shows the model when using PR3 + CC + SN+SH0ES + DESI, and the blue corner plot shows when PR4 + CC + SN+SH0ES + DESI was used.

Then DESI data was added, which is also shown in Fig. 4.6. The addition of the BAO data shifted the parameters ω_b, ω_{cdm} and n_s to lower values. When PR4 data was used, the addition of DESI did not affect the CPL's results of $100\theta_s$, $\ln(10^{10}A_s)$ and τ_{reio}. This did not occur when PR3 was used, as it can be seen that the results of the CPL parametrisation were affected when BAO data was added by shifting the values of these three parameters to lower values. The DESI data helped constrain the model by removing the degeneracies that occurred in the parameters $w_{0,CPL}$ and $w_{a,CPL}$ when PR3 was used. In Fig. 4.4, which showed the CPL model when only using late-time data, the graph showed that DESI lowered the value of H_0 and $w_{a,CPL}$ while $w_{0,CPL}$ was not affected. Therefore, it was expected that the DESI data would affect the CPL model the same way. However, the DESI data decreased the differences between the values of $w_{0,CPL}$ and $w_{a,CPL}$ that were seen in the previous graph. The addition of the newer BAO data, lowered the value of $w_{0,CPL}$ and slightly increased the value of $w_{a,CPL}$ when PR4 was considered, while the opposite effect occurred when PR3 was used. For the H_0 parameter, as expected, the DESI data lowered the value regardless of which Planck data was used. Moving on to the σ_8 parameter, the DESI data slightly shifted the parameter's values to lower values.

The correlation between H_0 and σ_8 that was seen in Fig. 4.5 is now also seen in Fig. 4.6 regardless of the data combinations that were taken. However, it is not as strong as when only early-time data was used. The anti-correlation that was seen in the previous graph, between $w_{0,CPL}$ and $w_{a,CPL}$ when only PR3 was used, was also seen only late-time data was used with DESI in Fig. 4.4. This anti-correlation is seen again in Fig. 4.6, except for when the PR3 + CC + SN+SH0ES data combination was used. When PR3 + CC + SN+SH0ES data was taken, instead of the expected anti-correlation, the linear model produced a correlation between $w_{a,CPL}$ and $w_{0,CPL}$. The linear model produced two other anti-correlations one between $w_{a,CPL}$ and σ_8 and another one between $w_{a,CPL}$ and H_0. The only time these anti-correlations were not seen is when the CPL model was tested with PR3 + CC + SN+SH0ES data, as no correlations are seen. When the DESI data was added, the CPL model shows an anti-correlation between $w_{0,CPL}$ and H_0 which is not visible when only CC and SN+SH0ES were taken as the late-time data. This was expected as this anti-correlation was not produced when only CMB data was taken and when CC + SN+SH0ES was taken, but was seen when CC + SN+SH0ES + DESI was taken seen, in Fig. 4.5 and Fig. 4.4 respectively. In general, the linear model obtianed the smallest posteriors when the PR4 + CC + SN+SH0ES + DESI was used. This was expected as DESI obtained the smallest posteriors when only late-time data was used in Fig. 4.4, and PR4 obtained the smallest posteriors when only early-time data was used in Fig. 4.5. It can also be seen that like in the constant model, the linear model does not show any tensions

between the dataset combinations.

Immediately, by looking at Table S7 and Table S8 it can be concluded that the linear model does not limit to the ΛCDM model despite the addition of late-time data. As neither $w_{0,CPL}$ nor $w_{a,CPL}$ are 1σ away from 0 and -1 respectively. The addition of the late-time data lowered the uncertainties of H_0 and σ_8 that were seen when only CMB data was used. Also, the addition of the late-time data lowered the values of the two parameters and are within the expected range in all four data combinations. When looking at the ΔAIC and ΔBIC it is concluded that when the PR3 + CC + SN+SH0ES data combination was used, the linear model is statistically better than the standard model as negative values are seen when taking both criteria. In the case of the other data combinations, the table shows that negative values were achieved only when the AIC criteria was taken, meaning that for the AIC, the CPL parametrisation fits the data better than the ΛCDM model. On the other hand, when taking the BIC criteria, positive values are seen, apart from the PR3 + CC + SN+SH0ES data combination. This shows that for the other three data combinations, the ΛCDM model remains to be the better model. Out of all four data combinations, it looks like the CPL model fit the PR3 + CC + SN+SH0ES data the best, as when that data combination was taken, the linear parametrisation model achieved the lowest values of AIC and BIC.

4.3 | Quadratic Model

The quadratic model, also referred to as the JBP parametrisation model assumes that w varies quadratically at current and late times but is constant at early times. From the chosen simulations results were obtained for this model and the values are shown in three tables: Table S9, Table S10, Table S11, and Table S12, where the tables show the values of the parameters and the value of the statistical criteria.

First, the JBP parametrisation was tested by using background data only, once CC and SN+SH0ES, then using CC and SN+SH0ES with the older BAO and another time using CC and SN+SH0ES with DESI BAO data. Therefore, a corner plot was made overlapping the three results as seen in Fig. 4.7. The graph shows that when the CC + SN+SH0ES data was used, the $w_{a,JBP}$ parameter and Ω_m were not constrained well as a wide 1D curve is seen showing multiple values having similar probability. The JBP model did not have any degeneracies when BAO or DESI were used. It is clearly seen that the DESI produced smaller posteriors than the other data combinations, showing that the JBP is more well defined when

Parameters	CC + SN+SH0ES		CC + SN+SH0ES BAO		CC + SN+SH0ES DESI	
	Best-fit	Mean	Best-fit	Mean	Best-fit	Mean
Sampled Parameters						
Ω_m	0.225	$0.242^{+0.098}_{-0.063}$	0.270	$0.273^{+0.015}_{-0.016}$	0.322	0.324 ± 0.011
$w_{0,JBP}$	-0.89	$-0.90^{+0.12}_{-0.10}$	-0.93	$-0.91^{+0.10}_{-0.11}$	-0.83	$-0.84^{+0.11}_{-0.09}$
$w_{a,JBP}$	0.73	$0.28^{+1.40}_{-0.85}$	0.31	$0.15^{+0.96}_{-0.85}$	-1.71	$-1.64^{+0.64}_{-0.82}$
Derived Parameters						
H_0	72.47	72.40 ± 0.89	72.29	$72.36^{+0.87}_{-0.88}$	71.49	$71.48^{+0.80}_{-0.81}$
χ^2 **Statistics**						
χ^2_{min}	1309		1322		1327	
ΔAIC	0.61		-0.38		-3.71	
ΔBIC	13.52		1.09		7.22	

Table S9: The values of the JBP model when using only late-time data.

Parameters	PR3		PR4	
	Best-fit	Mean	Best-fit	Mean
Sampled Parameters				
ω_b	0.02231	$0.02238^{+0.00015}_{-0.00016}$	0.02233	$0.02224^{+0.00013}_{-0.00014}$
ω_{cdm}	0.1204	0.1200 ± 0.0014	0.11830	0.11876 ± 0.00013
$100\theta_s$	1.04190	1.04190 ± 0.00030	1.04190	$1.04180^{+0.00025}_{-0.00026}$
$\ln(10^{10}A_s)$	3.061	$3.046^{+0.018}_{-0.016}$	3.040	$3.040^{+0.015}_{-0.014}$
n_s	0.9668	0.9652 ± 0.0046	0.9700	$0.9673^{+0.0043}_{-0.0039}$
τ_{reio}	0.0619	$0.0550^{+0.0081}_{-0.0083}$	0.0589	0.0575 ± 0.0062
$w_{0,JBP}$	-1.49	$-1.31^{+0.09}_{-0.19}$	-1.32	$-1.19^{+0.14}_{-0.32}$
$w_{a,JBP}$	-0.03	$0.34^{+0.75}_{-0.41}$	0.64	$0.17^{+0.50}_{-0.24}$
Derived Parameters				
H_0	82.96	$75.40^{+5.64}_{-4.33}$	74.88	$73.00^{+10.00}_{-6.00}$
σ_8	0.959	$0.882^{+0.050}_{-0.034}$	0.867	$0.848^{+0.089}_{-0.043}$
χ^2 **Statistics**				
χ^2_{min}	2769		30570	
ΔAIC	0.58		3.60	
ΔBIC	16.66		20.32	

Table S10: The values of the JBP model using the two Planck data sets: PR3 or PR4.

Parameters	PR3 CC + SN+SH0ES		PR4 CC + SN+SH0ES	
	Best-fit	Mean	Best-fit	Mean
Sampled Parameters				
ω_b	0.02250	$0.02248^{+0.00014}_{-0.00015}$	0.02233	0.02232 ± 0.00012
ω_{cdm}	0.1192	$0.1191^{+0.0013}_{-0.0012}$	0.1182	0.1180 ± 0.0011
$100\theta_s$	1.04190	$1.04200^{+0.00028}_{-0.00031}$	1.04200	1.04191 ± 0.00025
$\ln(10^{10}A_s)$	3.049	$3.046^{+0.016}_{-0.018}$	3.025	3.040 ± 0.014
n_s	0.9653	0.9676 ± 0.0044	0.9670	0.9693 ± 0.0039
τ_{reio}	0.0550	$0.0558^{+0.0078}_{-0.0084}$	0.0540	0.0589 ± 0.0063
$w_{0,JBP}$	-0.706	$-0.790^{+0.090}_{-0.021}$	-0.802	$-0.865^{+0.066}_{-0.029}$
$w_{a,JBP}$	-2.37	$-1.84^{+0.31}_{-0.58}$	-1.63	$-1.29^{+0.25}_{-0.47}$
Derived Parameters				
H_0	70.10	$70.24^{+0.68}_{-0.69}$	69.81	70.16 ± 0.67
σ_8	0.834	0.833 ± 0.012	0.817	0.826 ± 0.011
χ^2 **Statistics**				
χ^2_{min}		4098		31900
ΔAIC		-11.36		-8.40
ΔBIC		4.72		8.32

Table S11: The values obtained from the JBP model when using PR3 and PR4 with CC and SN+SH0ES data.

the DESI data was taken. So, following the trend of the previous parametrisation models, for the rest of the JBP model, the DESI data will be taken for the BAO data. Also, following the trend of the constant model, the posteriors of when DESI data or BAO data was used are within the posteriors of when only CC and SN+SH0ES data was used. This shows that there are no tensions within the datasets. Similar to the previous model from the posteriors, correlations and anti-correlations are seen between parameters. Similar to the two previously discussed models, when BAO data or DESI data were added to the other late-time data, a correlation is seen between H_0 and Ω_m, between $w_{0,JBP}$ and Ω_m and a slight correlation between $w_{a,JBP}$ and H_0 which were also seen and discussed in the CPL parametrisation. Also, similar to the CPL parametrisation, an anti-correlation is seen between $w_{0,JBP}$ and $w_{a,JBP}$, and there is an anti-correlation between Ω_m and $w_{a,JBP}$ which is seen in all the three data combinations. However, when only CC and SN+SH0ES were used, a non-linear anti-correlation between $w_{a,JBP}$ and Ω_m is present showing that the two parameters are anticorrelated when Ω_m is larger than 0.2. If Ω_m is smaller than 0.2, $w_{a,JBP}$ and Ω_m are not correlated. Like in the previous models, the DESI data produced a higher value of Ω_m and a lower value of H_0 than the two data combinations.

Parameters	PR3 CC + SN+SH0ES + DESI		PR4 CC + SN+SH0ES + DESI	
	Best-fit	Mean	Best-fit	Mean
Sampled Parameters				
ω_b	0.02262	0.02247 ± 0.00014	0.02238	$0.02232^{+0.00012}_{-0.00011}$
ω_{cdm}	0.1188	0.1191 ± 0.0011	0.11825	$0.11808^{+0.00095}_{-0.00097}$
$100\theta_s$	1.04190	$1.04190^{+0.00029}_{-0.00030}$	1.04190	$1.04190^{+0.00024}_{-0.00023}$
$\ln(10^{10}A_s)$	3.044	3.046 ± 0.016	3.034	3.039 ± 0.014
n_s	0.9697	$0.9674^{+0.0041}_{-0.0040}$	0.9690	$0.9692^{+0.0037}_{-0.0036}$
τ_{reio}	0.0528	$0.0559^{+0.0076}_{-0.0081}$	0.0572	$0.0585^{+0.0060}_{-0.0064}$
$w_{0,JBP}$	-0.78	$-0.81^{+0.10}_{-0.04}$	-0.830	$-0.878^{+0.078}_{-0.022}$
$w_{a,JBP}$	-1.75	$-1.60^{+0.39}_{-0.58}$	-1.41	$-1.12^{+0.29}_{-0.47}$
Derived Parameters				
H_0	69.68	69.80 ± 0.59	69.67	$69.75^{+0.60}_{-0.63}$
σ_8	0.825	$0.830^{+0.012}_{-0.011}$	0.820	0.822 ± 0.010
χ^2 **Statistics**				
χ^2_{min}		4114		31910
ΔAIC		-9.48		-6.40
ΔBIC		6.60		10.32

Table S12: Values of the quadratic model obtained from PR3 + CC + SN+SH0ES + DESI and PR4 + CC + SN+SH0ES + DESI.

When looking at Table S9, the value of H_0 is within the expected range of past research. The JBP model limits to the ΛCDM model when CC + SN+SH0ES and CC + SN+SH0ES + BAO data combinations were taken, as both $w_{0,JBP}$ and $w_{a,JBP}$ are 1σ away from -1 and 0 respectively. However, when DESI was used the JBP model no longer limits to the standard model as $w_{0,JBP}$ was pushed to a higher value and the $w_{a,JBP}$ was pushed to a lower value. The JBP parameterisation is statistically better than the standard model when the AIC criteria was used as negative values are seen in both BAO data combinations. This is not the case when CC + SN+SH0ES was taken and when the BIC criteria was used as positive values are seen despite using different BAO data, meaning that for the BIC criteria, the ΛCDM is still statistically better. Comparing the AIC and BIC shows that the JBP fits the CC + SN+SH0ES + DESI data better when it comes to the AIC criteria while for the BIC criteria, the JBP parametrisation fits the CC + SN+SH0ES + BAO data better.

After the background data was analysed, the model was tested using only early-time data PR3 and PR4. This was done to see how the model behaves when it only has CMB data. Furthermore, Fig.4.8 was plotted so that the model could be

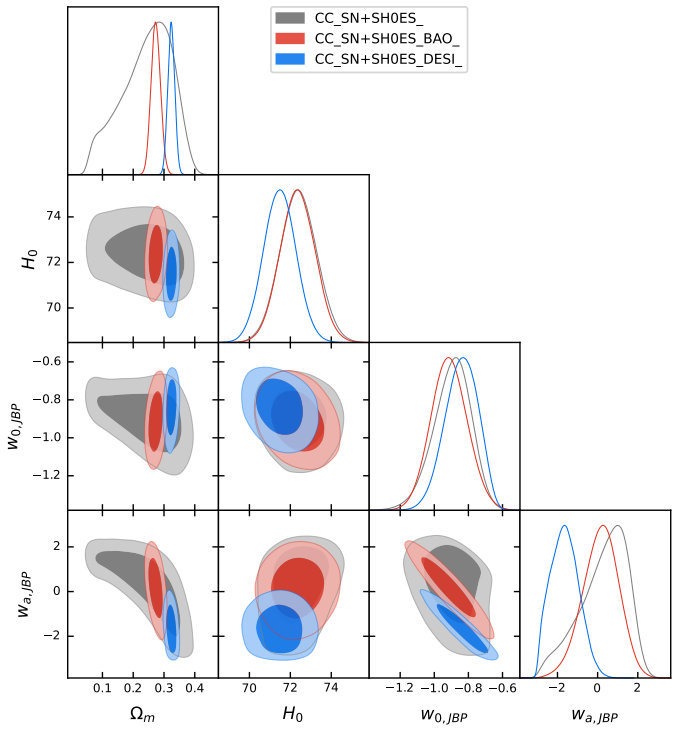

Figure 4.7: A graph showing the results obtained from the JBP model when only late-time data was taken into consideration. The grey corner plot shows the CC + SN+SH0ES data set combination, the red corner plot shows the CC + SN+SH0ES + BAO data combination and the blue corner plot shows the CC + SN+SH0ES + DESI data combination.

compared when different early-time data was used. The model was not able to be constrained by using the Gelman-Rubin criteria, which was expected, as the JBP parametrisation varies w quadratically only at the late Universe, while at early times w is constant. Thus, similarly to the linear model, it is not enough to have only early-time data to make the theoretical predictions on the JBP model. Subsequently, degeneracies are seen with the parameters $w_{0,JBP}$ and $w_{a,JBP}$ in both Planck data sets. However, when the recently released Planck data was used, degeneracies are also seen in the parameters H_0 and σ_8, while no degeneracies can be seen in these parameters when PR3 was used. When the newer Planck data was used, the model had lower values of ω_b, ω_{cdm} and $\ln(10^{10}A_s)$ while the values of $100\theta_s$, n_s and τ_{reio} stayed roughly the same. Following the trend of w_0CDM model, there is an anti-correlation between $w_{0,JBP}$ and H_0 as well as an anti-correlation between $w_{0,JBP}$ and σ_8. Subsequently, there is a correlation between H_0 and σ_8. The quadratic model achieved smaller posteriors in the six

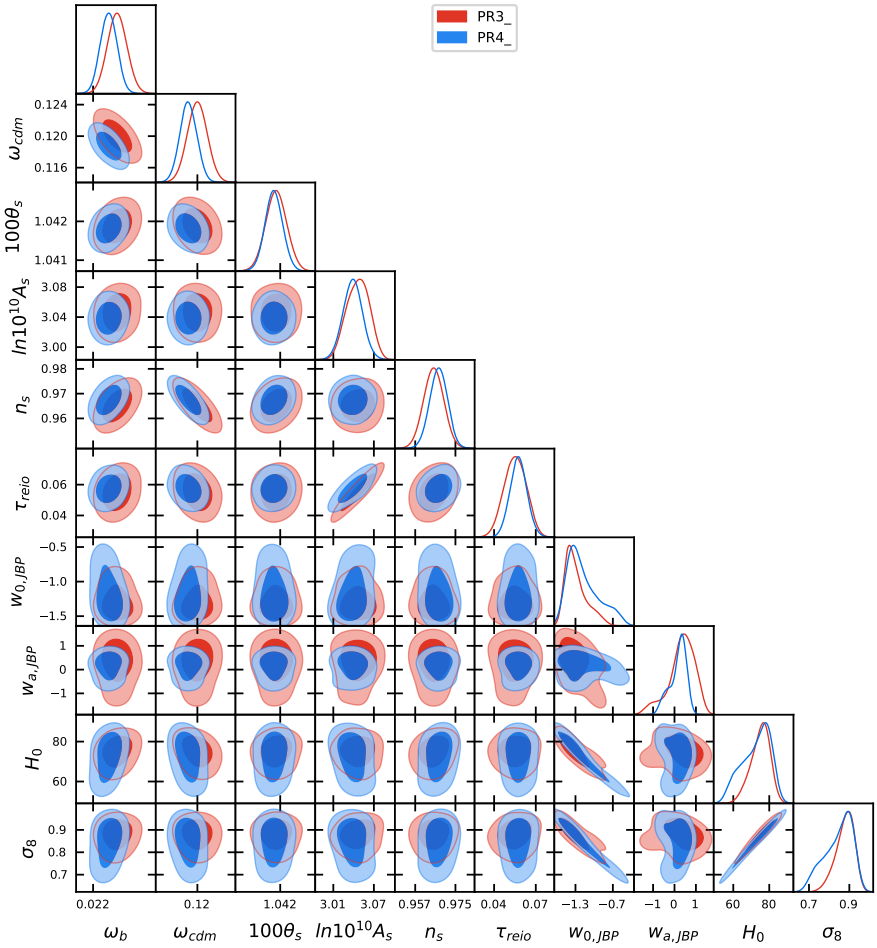

Figure 4.8: A graph of the JBP parametrisation when only having early-time data PR4 seen in blue or PR3 seen in red.

ΛCDM model and in the $w_{a,JBP}$ parameter when the recently released Planck data set was used, while smaller posteriors of $w_{0,JBP}$, H_0 and σ_8 were obtained when PR3 was used. This could be due to the quadratic model not converging with the Gelman-Rubin criteria. Similar to the previous models, the graph shows that there are no tensions between the Planck data as the posteriors either overlap or intersect each other.

From the values that were generated from this model shown in Table 4.8, they show that regardless of the chosen early-time data, $w_{a,JBP}$ is 1σ away from 0 but the parameter $w_{0,JBP}$ is not 1σ away from -1, so the JBP parametrisation does not limit to the ΛCDM model. The values of H_0 and σ_8 obtained from PR4 are within

the range of the expected value range while the value that was obtained from the previously released Planck data set is above the expected range. It can be noticed that the uncertainties of these values in both data sets are large which is a consequence of early-time data not being enough to constrain wCDM models. When comparing ΔAIC and ΔBIC, it seems like the standard model is statistically better than the JBP parametrisation, as positive values are seen in both Planck data sets regardless of whether AIC or BIC was chosen. From these values, it can also be concluded that the JBP model fits the PR3 data better than the PR4 data.

Following the trend of the previous two parametrisation models, the late-time data of CC and SN+SH0ES were added to the JBP model, shown in Fig. 4.9. As expected, the addition of the late-time data was enough to contain the JBP model as no degeneracies are seen with the parameters H_0 and σ_8. The late-time data constrained the H_0 parameter such that it removed any differences between the values that the two Planck data had previously, as the two 1D curves are now overlapping perfectly. When the PR3 was used the quadratic model did not produce any degeneracies with the $w_{0,JBP}$ and $w_{a,JBP}$ parameters. On the other hand, when the PR4 data was used, the quadratic model had small degeneracies with the wCDM parameters, showing that there is a small possibility that the value of $w_{0,JBP}$ would be around -1 and the value of $w_{a,JBP}$ would be 0. The addition decreased the differences between the values of $\ln(10^{10}A_s)$, n_s and τ_{reio} that the different data combinations obtained. When DESI data was added to the two data combinations, it can be seen in the corner plot that the addition of the newer BAO data did not affect the six ΛCDM parameters of the JBP parametrisation as it can be seen that the diagonal panels of when PR3 + CC + SN+SH0ES + DESI was used overlap the diagonal panels of when PR3 + CC + SN+SH0ES was used, and the same thing happened when PR4 was used instead of PR3.

The DESI data affected the quadratic model by slightly shifting the value of σ_8 to lower values. It also affected the parameters $w_{0,JBP}$ and $w_{a,JBP}$ by constraining them for when PR4 was used as no degeneracies can be seen. Additionally, instead of obtaining narrower curves, which was what was expected, the quadratic model widened the 1D curves of these two parameters. However, the posteriors that were obtained when DESI was included are smaller than when DESI was not included. Also, similarly to the previous graph, the newer Planck data produced smaller posteriors, showing that it is more well-defined than the older Planck data. Additionally, following the trend of the constant model, the graph shows no tensions between the four data combinations. From Fig. 4.7, it was concluded that the DESI data affected the quadratic model in a way that lowered the value of $w_{a,JBP}$ and H_0 and slightly increased the value of $w_{0,JBP}$. However, it can be seen in Fig. 4.9 that the $w_{0,JBP}$ parameter was not affected by this additional data. The

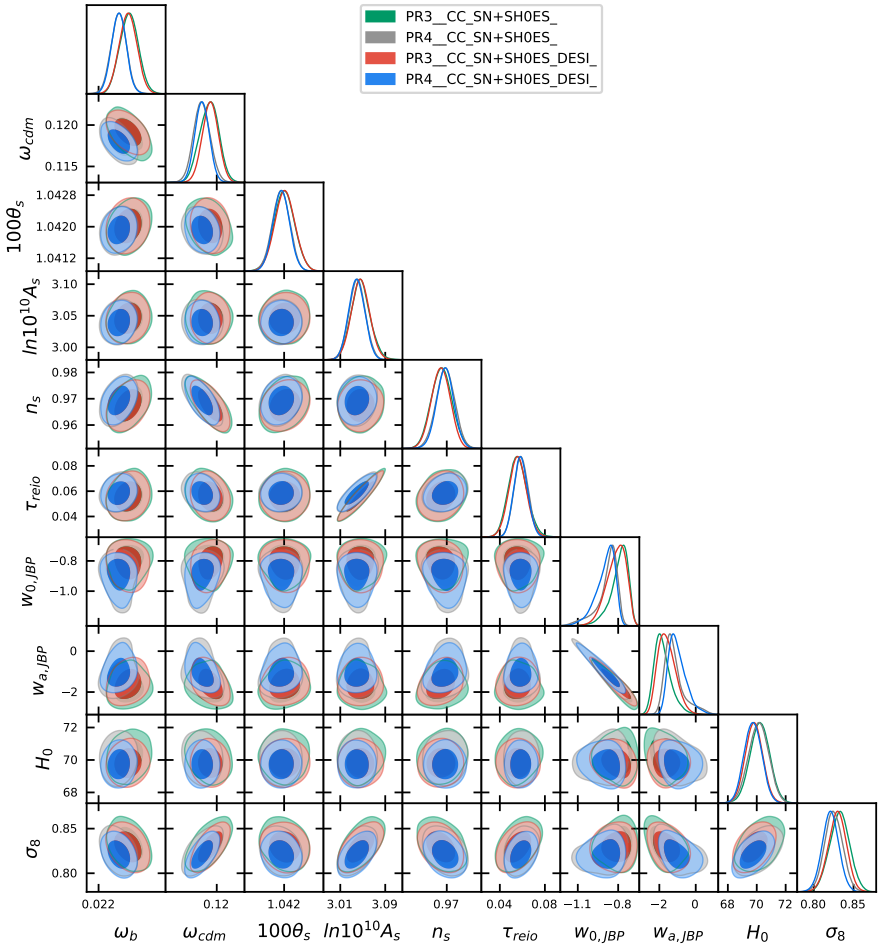

Figure 4.9: A graph generated with GetDist, showing the JBP model when PR3 with CC and SN+SH0ES data was used seen in the green corner plot, when PR4 with CC and SN+SH0ES data was used which is seen in the grey corner plot, when PR3 with CC, SN+SH0ES and DESI was used that can be seen in the red plot, and when PR4 with CC, SN+SH0ES and DESI was used seen in the blue plot.

$w_{a,JBP}$ parameter was only slightly affected as it was pushed slightly to higher values which is unlike what was seen in Fig. 4.7. The H_0 parameter was shifted to lower values like in Fig. 4.7.

In Fig. 4.9, correlations between parameters can be noticed. The anticorrelation between $w_{0,JBP}$ and H_0 that was seen when only early-time data was used is no longer visible when late-time data is added. However, similar to the previous two wCDM parameterisation models, an anticorrelation is seen between $w_{a,JBP}$ and $w_{0,JBP}$ that was not seen in the previous graph but was seen when only late-time data was used. A correlation between H_0 and σ_8 that was present in the previous graph, when only early-time was used, is still seen when late-time was added but it is less pronounced. Also, the JBP model reproduced the correlation between $w_{0,JBP}$ and σ_8 but it is also less defined than in the previous graph. The quadratic model procured another slight anticorrelation when late-time data was taken between $w_{a,JBP}$ and σ_8 that was not present when only Planck data was taken.

From Table S11 and Table S12, it can be noted that the JBP parametrisation does not limit to the standard model as $w_{0,JBP}$ and $w_{a,JBP}$ are not 1σ away from -1 and 0 respectively regardless of the chosen data combinations. CC and SN + SH0ES data lowered the value of H_0 and lessened the parameter's uncertainties and DESI data slightly lowered the value and uncertainties of H_0 even more. The addition of the late-time data also lowered the values and uncertainties of σ_8. The four values of H_0 and σ_8 that the JBP parametrisation obtained with the four data combinations are all within the expected range of past research. The JBP model achieved negative values of AIC and positive values of BIC regardless of whether the Planck data set was chosen and regardless of whether DESI was added or not, meaning that for the AIC, the JBP model fit the data better than the standard model while as for the BIC, the standard model fits the data better. When comparing the AIC and BIC for all data set combinations, it can be noticed that when DESI was included the JBP model achieved higher values of χ^2 and subsequently higher values of AIC and BIC. This shows that the quadratic model does not fit the DESI data well. From these values, it also seems that the JBP model fits the PR3 + CC + SN+SH0ES the best out of the four data combinations.

4.4 | Logarithmic Model

The logarithmic model (GE model) is taken where it explains the evolution of w as a logarithmic model. Table S13, Table S14, Table S15, and Table S16 show the results of the GE model that were achieved from MCMC chains that were run by

Parameters	CC + SN+SH0ES		CC + SN+SH0ES BAO		CC + SN+SH0ES DESI	
	Best-fit	Mean	Best-fit	Mean	Best-fit	Mean
Sampled Parameters						
Ω_m	0.269	$0.300^{+0.045}_{-0.059}$	0.274	$0.291^{+0.011}_{-0.033}$	0.437	$0.354^{+0.017}_{-0.052}$
$w_{0,GE}$	-0.88	$-0.91^{+0.11}_{-0.09}$	-0.888	$-0.876^{+0.046}_{-0.042}$	-1.023	$-1.033^{+0.037}_{-0.036}$
$w_{a,GE}$	-0.014	$-0.092^{+0.063}_{-0.055}$	-0.01507	$-0.12^{+0.13}_{-0.04}$	-0.183	$-0.118^{+0.023}_{-0.072}$
Derived Parameters						
H_0	72.34	$70.50^{+3.40}_{-1.10}$	72.25	$70.73^{+2.90}_{-4.03}$	61.15	$68.24^{+4.38}_{-1.83}$
χ^2 **Statistics**						
χ^2_{min}	1309		1322		1329	
ΔAIC	0.93		4.02		-1.86	
ΔBIC	13.84		14.95		9.06	

Table S13: The values of the GE model using only background data obtained from CLASS and MontePython simulations.

MontePython that used equations that were calculated by CLASS when the GE model was tested using different combinations of early-time and late-time data sets.

A graph was generated for the analysis of the logarithmic model when only using background data, shown in Fig. 4.10. Contrary to the previous models, late-time data on its own was not enough to constrain the logarithmic model as degeneracies are seen with the parameters of H_0 and $w_{a,GE}$ for all late-time data combinations while degeneracies are seen with Ω_m when CC + SN+SH0ES + DESI combination was used. The only parameter that does not have degeneracies and is well-defined in all the data combinations is the $w_{0,GE}$ parameter. Similarly to the other parameterizations, DESI data pushed the value of Ω_m to a higher value and pushed H_0 to a lower value. An anti-correlation is seen between Ω_m and $w_{a,GE}$ in all the late-time data combinations, the rate at which they are anti-correlated is constant regardless of the parameters' values. When CC + SN+SH0ES data was used an anti-correlation between $w_{0,GE}$ and Ω_m was produced but can not be seen when any of the BAO data were added. An anti-correlation is also seen between Ω_m and $w_{a,GE}$ and a correlation is seen between H_0 and $w_{a,GE}$. However, unlike in the previous models and in the anti-correlation of H_0 and Ω_m, the posteriors are curved. This means that the rate at which $w_{a,GE}$ and Ω_m are anti-correlated and $w_{a,GE}$ and H_0 are correlated depends on the values of the parameters and the rate depends on the chosen data set combination. When CC + SN+SH0ES + BAO was used, for values of $w_{a,GE}$ that are below -0.1, the rate of the anti-correlation and the correlation gradually decreases. On the other hand, when CC

Parameters	PR3		PR4	
	Best-fit	Mean	Best-fit	Mean
Sampled Parameters				
ω_b	0.02233	$0.02238^{+0.00015}_{-0.00016}$	0.02231	0.02223 ± 0.00013
ω_{cdm}	0.1203	0.1200 ± 0.0014	0.1179	0.1188 ± 0.0012
$100\theta_s$	1.0421	1.0419 ± 0.00030	1.0418	1.0418 ± 0.00025
$\ln(10^{10} A_s)$	3.052	3.045 ± 0.016	3.034	3.039 ± 0.014
n_s	0.9659	$0.9653^{+0.0045}_{-0.0046}$	0.9681	0.9673 ± 0.0040
τ_{reio}	0.0578	$0.0544^{+0.0076}_{-0.0081}$	0.0571	0.0577 ± 0.0062
$w_{0,GE}$	-1.14	$-1.03^{+0.05}_{-0.17}$	-1.09	-0.99 ± 0.12
$w_{a,GE}$	-0.07	$-0.18^{+0.07}_{-0.11}$	-0.014	-0.077 ± 0.043
Derived Parameters				
H_0	72.54	$70.77^{+5.02}_{-2.58}$	71.15	$67.62^{+5.02}_{-3.06}$
σ_8	0.864	$0.843^{+0.046}_{-0.022}$	0.829	$0.806^{+0.046}_{-0.026}$
χ^2 **Statistics**				
χ^2_{min}		2770		30570
ΔAIC		1.72		3.00
ΔBIC		17.80		19.61

Table S14: The values of the GE model when only early-time data were used.

+ SN+SH0ES + DESI or CC + SN+SH0ES was used, there is a noticeably sharper shift from the rate at which $w_{a,GE}$ and Ω_m are anti-correlated and $w_{a,GE}$ and H_0 are correlated from when $w_{a,GE}$ is higher than -0.1 to lower than -0.1. Thus, when comparing the two posteriors of the two data combinations, the change in rate when using DESI data or when not having any BAO data is less gradual than when the older BAO data was used. These curved posteriors occurred due to the logarithmic equation of w that the GE model has. Out of the two BAO data, DESI obtained the smallest posteriors showing that it constrains the GE model better than the older BAO data. Thus, the DESI data set will be used instead of the older BAO data for the rest of the results obtained from the GE model. The posteriors also show that there are no tensions between the datasets which is what was seen in the previous reparameterisation models.

When looking at Table S13, when CC + SN+SH0ES + BAO was used, $w_{a,GE}$ is 1σ away from 0 but $w_{0,GE}$ is not 1σ away from -1. The opposite occurred when CC + SN+SH0ES used and when DESI was added, as in both cases $w_{0,GE}$ is 1σ away from -1 but $w_{a,GE}$ is not 1σ away from 0. This means that the GE model does not limit to the ΛCDM model regardless of the chosen BAO data and regardless of whether any BAO data is included or not. In all three cases, H_0 agrees with past research as it is within the expected range. However, it can be noticed that

Parameters	PR3 CC + SN+SH0ES		PR4 CC + SN+SH0ES	
	Best-fit	Mean	Best-fit	Mean
Sampled Parameters				
ω_b	0.02248	0.02251 ± 0.00015	0.022426	0.02235 ± 0.00012
ω_{cdm}	0.1182	0.1186 ± 0.0013	0.11743	0.1176 ± 0.0011
$100\theta_s$	1.0419	1.04205 ± 0.00029	1.0420	1.04195 ± 0.00024
$\ln(10^{10}A_s)$	3.055	3.046 ± 0.016	3.0464	3.040 ± 0.014
n_s	0.9678	0.9688 ± 0.0043	0.9704	0.9704 ± 0.0039
τ_{reio}	0.0630	$0.0565^{+0.0074}_{-0.0082}$	0.0588	0.0593 ± 0.0063
$w_{0,GE}$	-0.932	$-0.960^{+0.034}_{-0.082}$	-0.978	$-1.004^{+0.029}_{-0.026}$
$w_{a,GE}$	-0.274	$-0.246^{+0.025}_{-0.056}$	-1.9132	$-0.149^{+0.024}_{-0.052}$
Derived Parameters				
H_0	69.83	70.22 ± 0.68	57.22	63.60 ± 4.80
σ_8	0.828	0.830 ± 0.012	0.713	$0.767^{+0.052}_{-0.040}$
χ^2 **Statistics**				
χ^2_{min}		4098		31900
ΔAIC		-11.54		-6.00
ΔBIC		4.54		10.72

Table S15: The values of the logarithmic model when using PR3 and PR4 with CC and SN+SH0ES data.

the uncertainties of H_0 are significantly higher than in the previous models this is probably due to the degeneracies with the parameter that occurred in this model that did not occur in the other models. From the AIC and BIC it is seen that only one negative value was achieved from the GE when the CC + SN+SH0ES + DESI data combination was taken and when the AIC criteria was calculated, meaning that only in that case was the GE model statistically better than the standard model. By comparing the AIC and BIC for the three data combinations, it can be concluded that the GE model fits the DESI data better than the other BAO data, and better than when only CC and SN+SH0ES data was used.

For the analysis of the two CMB data sets when using the GE parametrisation a graph was rendered, overlapping the two corner plots that were obtained from the results of the model. This graph can be seen in Fig. 4.11. By first focussing on the six ΛCDM parameters, the figure shows that for the parameter $100\theta_s$ the results of the 1D curves overlap each other for the two Planck data sets while for n_s and τ_{reio}, there are only slight shifts to higher values and a slight shift of the $\ln(10^{10}A_s)$ parameter to lower values in the PR4 results. For the ω_b and ω_{cdm} there are significant shifts towards lower values in the newer data set when

Parameters	PR3 CC + SN+SH0ES + DESI		PR4 CC + SN+SH0ES + DESI	
	Best-fit	Mean	Best-fit	Mean
Sampled Parameters				
ω_b	0.02248	$0.02251^{+0.00015}_{-0.00016}$	0.02237	0.02234 ± 0.00012
ω_{cdm}	0.1182	$0.1186^{+0.0013}_{-0.0014}$	0.11734	$0.11776^{+0.00091}_{-0.00096}$
$100\theta_s$	1.04190	1.04210 ± 0.00030	1.04210	1.04190 ± 0.00024
$\ln(10^{10}A_s)$	3.055	3.048 ± 0.016	3.025	$3.041^{+0.015}_{-0.014}$
n_s	0.9678	$0.9688^{+0.0044}_{-0.0045}$	0.9707	0.9700 ± 0.0035
τ_{reio}	0.0622	$0.0574^{+0.0078}_{-0.0081}$	0.0525	$0.0592^{+0.0059}_{-0.0069}$
$w_{0,GE}$	-0.932	$-0.970^{+0.034}_{-0.030}$	-0.979	$-1.000^{+0.028}_{-0.025}$
$w_{a,GE}$	-0.273	$-0.245^{+0.011}_{-0.055}$	-0.195	$-0.146^{+0.013}_{-0.054}$
Derived Parameters				
H_0	69.83	$70.20^{+0.66}_{-0.68}$	56.17	$64.10^{+5.80}_{-3.90}$
$_8$	0.828	0.830 ± 0.012	0.696	$0.773^{0.049}_{-0.032}$
χ^2 **Statistics**				
χ^2_{min}		4098		31910
ΔAIC		-25.52		-4.60
ΔBIC		-9.44		12.12

Table S16: Values of the GE model obtained from the two Planck data with CC, SN+SH0ES and DESI data.

compared to the older data set. Lowering ω_b reduces the amplitude of the CMB power spectrum peaks discussed in Chapter 2, weakening the imprint of baryon-photon interactions in the early Universe, and it also means that less baryonic material is available to form stars, galaxies, and other structures. A lower ω_{cdm} would slow down the growth of cosmic structures like galaxies, clusters, and superclusters thus, leading to weaker lensing effects observed in galaxy clusters and along lines of sight to distant objects. Dark matter drives the initial collapse of matter into gravitational wells, and with less dark matter, this process becomes less efficient.

On the other hand, the area of the 2D panels in the PR4 run is smaller than in the PR3 run. The smaller posteriors and confidence regions indicate that the probability mass is highly concentrated around a specific region, with little spread across the parameter space. This is a sign of high certainty in the newer Planck data set's predictions. For the two additional parameters of the GE parameterization, $w_{0,GE}$ the two data sets give a similar 1D curve. This is not the case for the $w_{a,GE}$ parameter, since PR4 shows a narrower curve and has a higher value than PR3. For the H_0 and the σ_8 parameters, the 1D curves are similar in shape

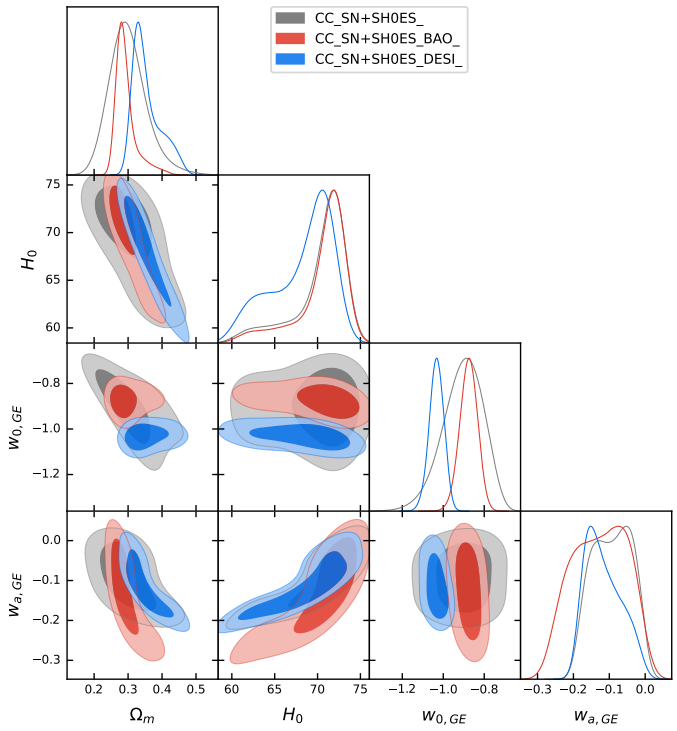

Figure 4.10: A graph of the GE model when using only late-time data; CC + SN+SH0ES shown in grey; CC + SN+SH0ES + BAO shown in red; and CC + SN+SH0ES + DESI shown in blue.

but for the PR3 data, the curve is narrower and shifted to higher values. Degeneracies are seen in the parameters $w_{0,GE}$ with the recently released Planck dataset and $w_{a,GE}$ with both Planck datasets showing that there are a range of equally likely values that the parameters can have. This indicates that the two Planck data sets are not able to constrain the model on their own and might need additional data. Following the trend of the w_0CDM model, a strong anti-correlation is seen between H_0 and $w_{0,GE}$ and between $w_{0,GE}$ and σ_8 in both of the Planck data. Subsequently, there is also a strong correlation between H_0 and σ_8 in the two data sets. The posteriors also indicate that there are no tensions between the two Planck datasets which was expected as it was seen in the previous models.

By analysing Table S14 it can be noted that in both Planck data sets, the value of $w_{0,GE}$ is 1σ away from the value of the standard model in cosmology while for the $w_{a,GE}$ parameter is not 1σ away. The PR4 data set obtained a lower value of 67.62 for H_0 than the expected possible values of H_0 while the value of H_0 achieved from PR3 is within the expected range of values. The GE model, like

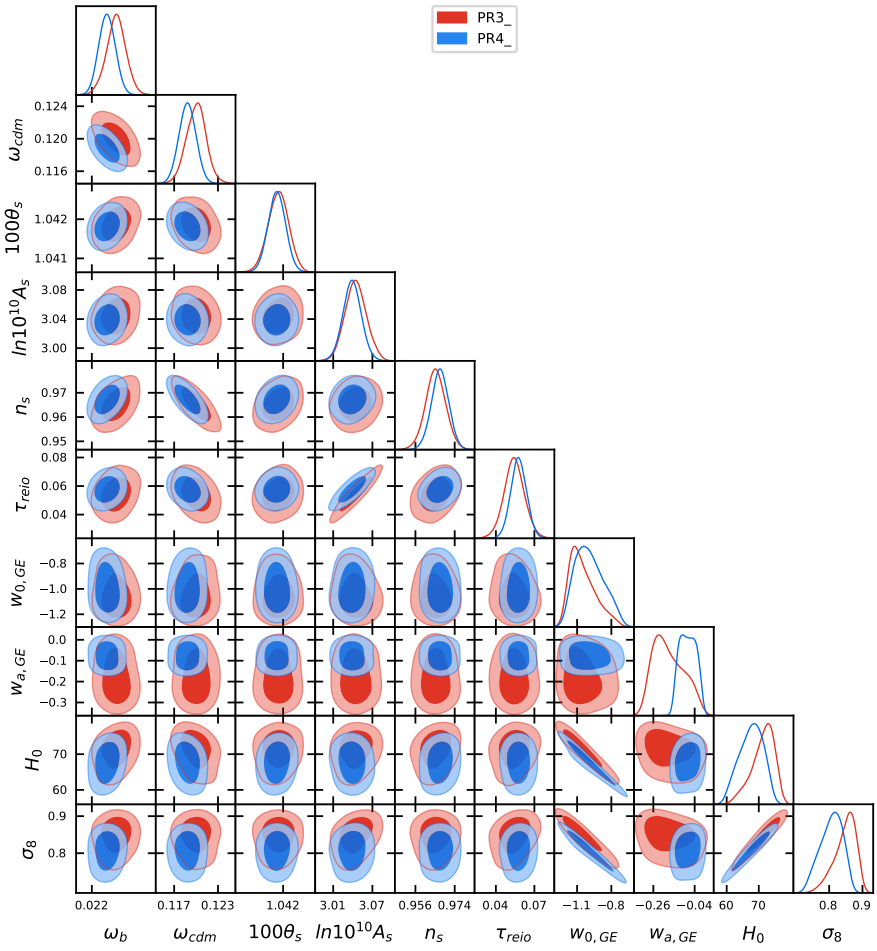

Figure 4.11: The GE parameterisation when taking the observational data of PR4 shown in the blue corner plot and PR3 shown in the red corner plot.

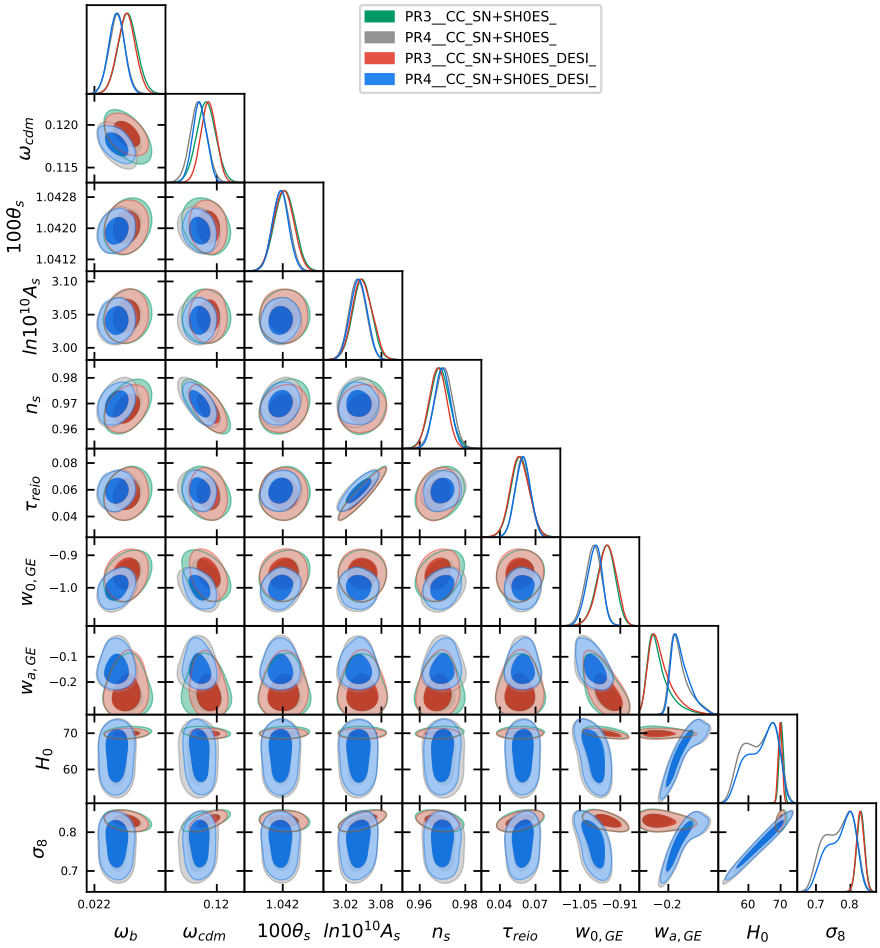

Figure 4.12: A graph showing the logarithmic model when the late-time data CC and SN+SH0ES are used with PR3 seen in green or PR4 seen in grey. Then DESI was added to the two data combinations; PR3 + CC + SN+SH0ES + DESI seen in the red corner plot and PR4 + CC + SN+SH0ES + DESI seen in the blue corner plot.

the previously discussed wCDM parameterisation models, varies w in the late Universe. Thus, CMB data is not enough to constrain the parameters of H_0 and σ_8 which results in high uncertainties with their values. The AIC for the PR3 is less than the AIC of the PR4, showing that PR3 is statistically better than the recently released data set. However, the opposite is true when looking at the BIC of the two runs, as they show that PR4 is statistically better.

For a better picture of the logarithmic model, the late-time of CC and SN+SH0ES

were added to the Planck data, and then DESI was added. The results were plotted in a corner plot seen in Fig. 4.12 so that the 1D curves and the posteriors between the parameters could be seen. From the graph, it can be seen that despite the addition of the late-time data, the recently released data set still does not manage to constrain the logarithmic model as degeneracies are still seen especially in the H_0 and the σ_8 parameters, showing a range of possible values that the logarithmic model has for H_0 and σ_8. However, it is easily noticeable that the late-time data has helped constrain the model, especially for the $w_{0,GE}$ and $w_{a,GE}$ parameter for both Planck data. The data combination that contains the PR4 data generated a correlation between H_0 and $w_{a,GE}$ in the PR4 + CC + SN+SH0ES data combination, which was not seen in the previous graph. Changes in $w_{a,GE}$ imply a different rate of evolution in dark energy, which then affects the current expansion rate and the inferred value of H_0. Unlike, what was seen in previous parameterisation models, this correlation is not linear as it is seen as curved. It is curved in a way that for values of H_0 that are roughly higher than 65 $\text{kms}^{-1}\text{Mpc}^{-1}$, $w_{a,GE}$ and H_0 are no longer correlated. This is due to the equation of w for this model being logarithmic. The same correlation is seen between $w_{a,GE}$ and σ_8 when PR4 data was used. The GE model exhibits an anti-correlation between the parameters $w_{a,GE}$ and $w_{0,GE}$ when the CC and SN+SH0ES were used regardless of the early-time data that was used. The posterior of these two parameters is also curved. This scenario shows that the rate at which $w_{0,GE}$ and $w_{a,GE}$ are anti-correlated is dependent on the parameters' values. For larger values of $w_{0,GE}$, and subsequently for smaller values of $w_{a,GE}$ the anti-correlation is more present. The anti-correlation between the H_0 and $w_{0,GE}$ in Fig. 4.12 is vaguely seen when the PR4 + CC + SN+SH0ES data was used which was also seen in the previous graph, but the anti-correlation is no longer there when the early-time data PR3 was used. This anti-correlation is also curved as it shows that the anti-correlation between H_0 and $w_{0,GE}$ is more pronounced for values of H_0 that are roughly higher than 65 $\text{kms}^{-1}\text{Mpc}^{-1}$. These curved posteriors are due to the logarithmic equation of w_{GE}. A linear correlation is seen between H_0 and σ_8 when the recently released CMB data was used. The addition of the late-time data, increased the differences between the values of $100\theta_s$ while decreasing the differences between the values of n_s.

When the DESI data was added, it did not affect the diagonal panels of the six ΛCDM parameters as the 1D curves of when PR3 + CC + SN+SH0ES + DESI overlap the 1D curves of when PR3 + CC + SN+SH0ES, was used while the results obtained from PR4 + CC + SN+SH0ES + DESI overlap the 1D curves obtained from PR4 + CC + SN+SH0ES. Degeneracies are seen in the logarithmic model when the PR4 + CC + SN+SH0ES + DESI, furthermore, this shows that the DESI was not enough to constrain the H_0 and σ_8 parameters. The DESI

data also did not affect the correlations that were obtained when only CC and SN+SH0ES were used for the late-time data. When looking at the parameters $w_{0,GE}$, $w_{a,GE}$ and H_0, Fig. 4.10 showed that the DESI data affected the model by lowering the values of H_0, $w_{0,GE}$ and $w_{a,GE}$. However, when DESI was added to the early-time data, it seemed to not have affected these three parameters and also did not affect σ_8. The DESI data helped constrain the logarithm model better as smaller posteriors were retrieved. Similarly, PR4 constrains the model better than the PR3 data as the posteriors that the GE model obtained with the recently released Planck data are smaller than the posteriors that the logarithm parameterisation obtained with the previously released Planck dataset. Subsequently, the GE model obtained the smallest posteriors when the PR4 + CC + SN+SH0ES + DESI data combination was used. Following the trend of the other models, the posteriors in Fig. 4.12 show that the logarithmic model has no tensions between the data combinations that were used.

From Table S15 and Table S16, it can be concluded that the GE model does not limit to the ΛCDM model even though four data combinations were tested, as $w_{0,GE}$ is 1σ away from -1 in all cases but $w_{a,GE}$ is not 1σ away from 0 for none of them. The model produced a lower value of H_0 than what past research show when the newer Planck data was used. The addition of the late-time data lowered the values of H_0 and σ_8 for the PR4 data combination and the uncertainty of this parameter is still large. On the other hand, the parameterization obtained values of H_0 and σ_8 of around 70.20 Km s^{-1}Mpc-1 and 0.830 when PR3 was used, which is within the range of past research and the uncertainties decreased as expected. The AIC criteria shows that the GE parameterisation is statistically better than the standard model as negative values are seen when two data combinations were used. However, when the BIC criteria was taken, only when PR3 + CC + SN+SH0ES + DESI data was used was the logarithmic model statistically better than the standard model. In the rest of the data combinations, the BIC criteria shows that the ΛCDM model fits the data better than the GE model. From the ΔAIC and ΔBIC values, it can also be concluded that the GE parameterisation fits the data combinations that have PR3 better than the data combinations that have PR4.

4.5 | Barboza and Alcaniz

The values for this model are shown in Table S17, Table S18, Table S19, and Table S20. The tables show the values of the samples and derived parameters as well as the values of the statistical criteria. From these values, plot were generated and conclusions were able to be made.

Parameters	CC + SN+SH0ES		CC + SN+SH0ES BAO		CC + SN+SH0ES DESI	
	Best-fit	Mean	Best-fit	Mean	Best-fit	Mean
Sampled Parameters						
Ω_m	0.17	$0.27^{+0.10}_{-0.06}$	0.271	$0.275^{+0.015}_{-0.016}$	0.325	0.326 ± 0.011
$w_{0,BA}$	-0.79	$-0.89^{+0.12}_{-0.09}$	-0.901	$-0.893^{+0.066}_{-0.067}$	-0.901	$-0.897^{+0.067}_{-0.069}$
$w_{a,BA}$	0.28	$-0.12^{+0.58}_{-0.29}$	0.04	$-0.02^{+0.30}_{-0.24}$	-0.56	$-0.59^{+0.25}_{-0.21}$
Derived Parameters						
H_0	72.36	72.28 ± 0.86	72.35	72.35 ± 0.87	71.65	$71.76^{+0.79}_{-0.81}$
χ^2 **Statistics**						
χ^2_{min}		1309		1322		1324
ΔAIC		0.68		-2.40		-6.33
ΔBIC		13.59		8.53		4.60

Table S17: The values of the parameters for the BA parameterisation using only late-time data.

Parameters	PR3		PR4	
	Best-fit	Mean	Best-fit	Mean
Sampled Parameters				
ω_b	0.02239	$0.02240^{+0.00015}_{-0.00016}$	0.022264	0.022240 ± 0.00013
ω_{cdm}	0.1195	0.1199 ± 0.0014	0.1190	0.1188 ± 0.0012
$100\theta_s$	1.0417	1.0419 ± 0.0030	1.0417	$1.0418^{+0.00025}_{-0.00024}$
$\ln(10^{10} A_s)$	3.048	$3.046^{+0.015}_{-0.019}$	3.031	3.042 ± 0.015
n_s	0.9682	$0.9656^{+0.0045}_{-0.0046}$	0.9695	0.9701 ± 0.0039
τ_{reio}	0.0555	$0.0549^{+0.0074}_{-0.0081}$	0.0578	0.0590 ± 0.0065
$w_{0,BA}$	-1.38	$-1.20^{+0.15}_{-0.30}$	-1.08	$-1.22^{+0.22}_{-0.28}$
$w_{a,BA}$	-0.46	$-0.44^{+0.60}_{-0.22}$	-0.13	$-0.11^{+0.37}_{-0.27}$
Derived Parameters				
H_0	85.12	$78.77^{+7.72}_{-7.87}$	71.73	$72.81^{+4.69}_{-6.47}$
σ_8	0.965	$0.911^{+0.067}_{-0.060}$	0.842	$0.850^{+0.047}_{-0.050}$
χ^2 **Statistics**				
χ^2_{min}		2768		30570
ΔAIC		-0.20		2.60
ΔBIC		15.88		19.21

Table S18: The values achieved from CLASS and MontePython when assuming the BA parametrisation using PR3 and PR4.

Parameters	PR3 CC + SN+SH0ES		PR4 CC + SN+SH0ES	
	Best-fit	Mean	Best-fit	Mean
Sampled Parameters				
ω_b	0.02252	$0.02245^{+0.00014}_{-0.00015}$	0.02242	$0.02232^{+0.00013}_{-0.00012}$
ω_{cdm}	0.1179	0.1191 ± 0.0013	0.1173	0.1180 ± 0.0011
$100\theta_s$	1.04200	1.04200 ± 0.00030	1.04180	$1.04190^{+0.00025}_{-0.00024}$
$\ln(10^{10} A_s)$	3.041	$3.045^{+0.016}_{-0.017}$	3.047	$3.039^{+0.014}_{-0.015}$
n_s	0.9726	$0.9674^{+0.0044}_{-0.0043}$	0.9750	$0.9695^{+0.0039}_{-0.0040}$
τ_{reio}	0.0523	$0.0553^{+0.0072}_{-0.0082}$	0.0634	$0.0585^{+0.0061}_{-0.0064}$
$w_{0,BA}$	-0.787	$-0.797^{+0.069}_{-0.066}$	-0.741	$-0.799^{+0.066}_{-0.067}$
$w_{a,BA}$	-0.71	$-0.73^{+0.19}_{-0.20}$	-0.81	$-0.70^{+0.20}_{-0.18}$
Derived Parameters				
H_0	71.05	$70.84^{+0.66}_{-0.71}$	70.90	$70.81^{+0.71}_{-0.72}$
σ_8	0.835	0.842 ± 0.012	0.836	0.835 ± 0.011
χ^2 **Statistics**				
χ^2_{min}		2046.21		31890
ΔAIC		-16.70		-14.20
ΔBIC		-0.62		2.52

Table S19: The values of the BA model when using only CC and SN+SH0ES for late-time data together with PR3 or PR4.

We first focus on the effect that the two BAO data have on the BA model, so a graph showcasing the results seen in Table S17, was rendered and can be seen in Fig. 4.13. Unlike in the logarithmic model, the late-time data on its own was enough to constrain the BA model such that no degeneracies are seen in any of the parameters. The 1D curve of the Ω_m parameter is wide enough to show that any BAO data was required for better constraints of that parameter. It is important to point out that the BA model produced the same 1D curve for $w_{0,BA}$ for the two different data set combinations that contain BAO. Similarly to the previously discussed wCDM parameterisations, when the DESI data was used the BA model achieved a higher value of Ω_m, and a lower value of H_0 and $w_{a,BA}$, while the BAO data achieved a lower value of Ω_m. Following the trend of the previous models, the BAO data did not affect the model with regards to the H_0 and $w_{a,BA}$ except for constraining the model better. Also, DESI produced smaller posteriors than when the older BAO data set was used, which was expected as this was seen in the other models. Therefore, the DESI data is better data, so DESI will be added to the early-time data instead of the older BAO data set. The posteriors show that there are no tensions between the data combinations which is in agreement with the other tested models. Like in the first three models, there is a correlation

Parameters	PR3 CC + SN+SH0ES + DESI		PR4 CC + SN+SH0ES + DESI	
	Best-fit	Mean	Best-fit	Mean
Sampled Parameters				
ω_b	0.02252	$0.0225^{+0.00014}_{-0.00015}$	0.02232	0.02228 ± 0.00012
ω_{cdm}	0.1179	0.1191 ± 0.0013	0.11901	0.11865 ± 0.00010
$100\theta_s$	1.0420	1.0420 ± 0.00030	1.04170	1.04170 ± 0.00024
$\ln(10^{10}A_s)$	3.041	$3.045^{+0.016}_{-0.017}$	3.041	$3.039^{+0.015}_{-0.014}$
n_s	0.9726	$0.9674^{+0.0044}_{-0.0043}$	0.9648	$0.9679^{+0.0038}_{-0.0035}$
τ_{reio}	0.0523	$0.0553^{+0.0072}_{-0.0082}$	0.0572	$0.0580^{+0.0062}_{-0.0065}$
$w_{0,BA}$	-0.787	$-0.797^{+0.069}_{-0.066}$	-0.869	$-0.890^{+0.045}_{-0.047}$
$w_{a,BA}$	-0.71	$-0.73^{+0.19}_{-0.20}$	-0.45	$-0.41^{+0.13}_{-0.09}$
Derived Parameters				
H_0	71.05	$70.84^{+0.66}_{-0.71}$	69.62	$69.86^{+0.61}_{-0.64}$
σ_8	0.835	0.842 ± 0.012	0.829	$0.829^{+0.010}_{-0.011}$
χ^2 **Statistics**				
χ^2_{min}		4109		31910
ΔAIC		-14.28		-9.40
ΔBIC		1.80		7.32

Table S20: Values of the BA model when the late-time data of CC, SN+SH0ES and DESI were used in conjunction with early-time data.

between Ω_m and H_0 and an anti-correlation between $w_{0,BA}$ and H_0 that is only seen when BAO or DESI data set were used. Also, similar to the CPL and JBP parameterisations, there is an anti-correlation between $w_{0,BA}$ and $w_{a,BA}$ with the two BAO data sets, another anti-correlation between Ω_m and $w_{a,BA}$ that is seen in the three data combinations, and the parameters $w_{0,BA}$ and Ω_m are correlated when DESI or BAO data was added. However, no correlations between H_0 and $w_{a,BA}$ can be seen.

Moving on to analysing Table S17, it can be noted that the BA parameterisation does not limit to the ΛCDM model regardless of using different BAO data, as only $w_{a,BA}$ is 1σ away from 0 when CC + SN+SH0ES + BAO and when CC + SN+SH0ES data were used. The value of H_0 is in the expected range of past research and unlike in the logarithmic model, the uncertainties of H_0 are small in the BA model. When looking at the ΔAIC and ΔBIC, the BA model is statistically better than the standard model when the AIC criteria was taken, as negative values were found in both BAO data combinations. However, for the case of the BIC criteria, the standard fits the data better than the BA parameterisation. As for when CC + SN+SH0ES was used, positive values of ΔAIC and ΔBIC are shown,

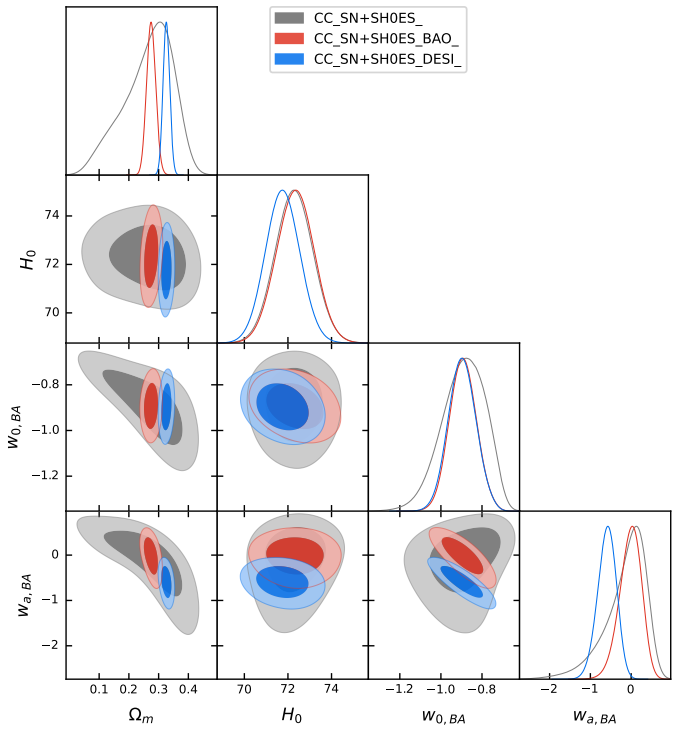

Figure 4.13: A graph of the BA model when using CC + SN+SH0ES shown in the grey corner plot, CC + SN+SH0ES + BAO shown in the red corner plot and CC + SN+SH0ES + DESI shown in the blue corner plot.

meaning that the ΛCDM model fits the CC and SN+SH0ES data better than the BA parameterisation. When comparing the data combinations it seems that the BA model fits the DESI data better than the other two late-time data combinations.

Moving on to the analysis of the two CMB data sets, Fig. 4.14 was plotted to show the two Planck data sets on their own when the BA model is taken. PR4 managed to obtain lower values of ω_b, ω_{cdm}, $100\theta_s$ and $\ln(10^{10}A_s)$ while obtaining higher values of n_s and τ_{reio} than PR3. Both the two corner plots were not able to converge with the Gelman-Rubin criteria and degeneracies are seen in the parameters of $w_{0,BA}$ and $w_{a,BA}$. Despite both of them not being able to converge, the newer Planck data set still manages to obtain smaller posteriors showing that it still constrains the model better than PR3, and from the posteriors it can be concluded that there are no tensions between the PR3 and PR4, which agrees with the previous models. The PR4 shifted the values of H_0 and σ_8 to lower values when compared to when PR3 was used. In both plots, there is an anti-correlation

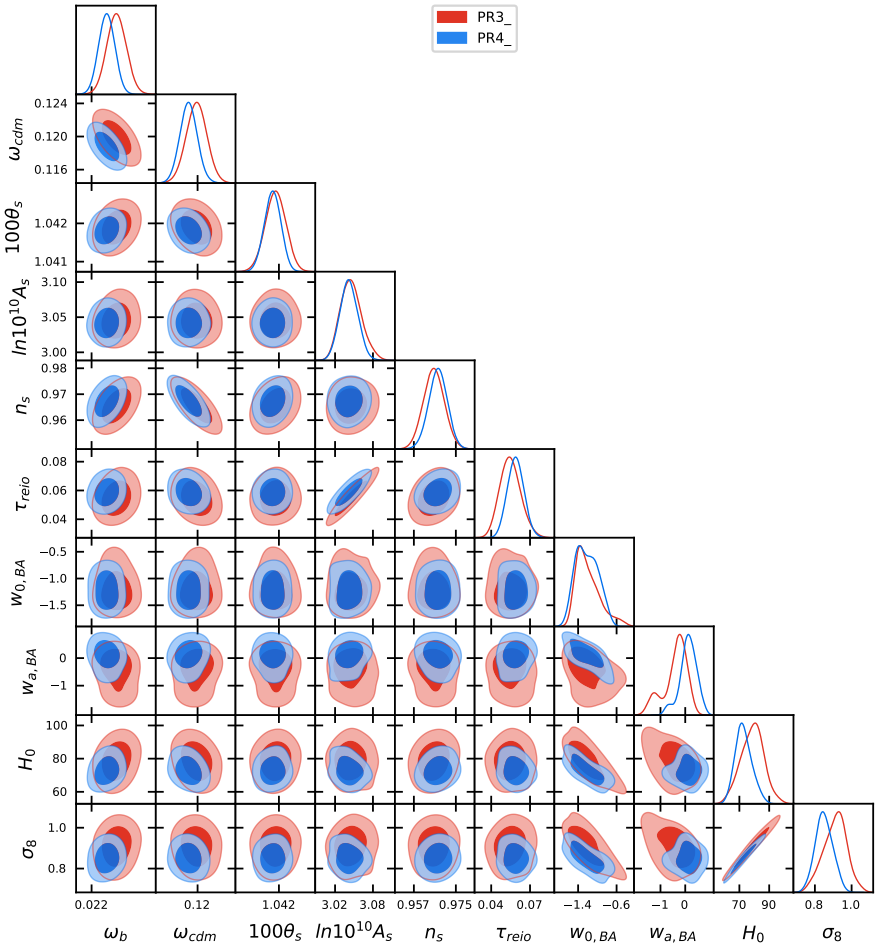

Figure 4.14: A graph showing the two early-time data sets when using the BA parametrisation without the influence of late-time data. The results obtained from the BA model when PR3 was used are depicted in the red corner plot, and the results when PR4 was used are depicted in the blue corner plot.

between H_0 and $w_{0,BA}$, and another one between $w_{0,BA}$ and σ_8. A strong correlation can be seen between H_0 and σ_8 in both data sets.

When looking at Table S18, the values of H_0 and σ_8 for the previously released data set are out of the expected range of possible values, while for the recently released data set, they are both within that range. The BA model limits to the standard model with the newer early-time data set but it does not with the older Planck data set as when PR4 is used both $w_{0,BA}$ and $w_{a,BA}$ are 1σ away from -1 and 0 respectively but this is not the case when PR3 was used. When the AIC statistic was taken a negative value was obtained when the PR3 was used, meaning that the BA model fit the PR3 data better than the ΛCDM model but not for the PR4 data. When the BIC statistic was taken it showed that the standard model fits the PR3 and the PR4 data better than the BA parameterisation. The ΔAIC and ΔBIC are lower for the older data set, showing that the BA model is statistically better with the PR3 data than for the newer Planck data set.

Late-time data, CC, SN+SH0ES were added to the early-time data, seen in Fig. 4.15. From the graph, it can be seen that the late-time data with the PR3 data was not enough to constrain the model, as degeneracies are seen with $w_{0,BA}$ and $w_{a,BA}$. When PR4 data was used no degeneracies in the two parameters were found in the blue corner plot, showing that the BA model was constrained when PR4 + CC + SN+SH0ES was used. That means that the BA model is more well-defined when PR4 is used. When CC and SN+SH0ES were added to the early-time data, they affected the results of the BA model in a way that the differences in results between the two data combinations, in the values of $100\theta_s$ and $\ln(10^{10}A_s)$ have increased while the differences in the n_s, τ_{reio} and H_0 parameters decreased. When looking at the two wCDM parameters, it can be seen that the additional data increased the differences between the two Planck data. The CC and SN+SH0ES data affected the BA model by pushing the values of $w_{0,BA}$ to higher values and $w_{a,BA}$ to lower values. The CC and SN+SH0ES data also shifted the values of H_0 and σ_8 that was produced when using PR3 to lower values and hence, decreasing the difference between the BA model's values of H_0 and σ_8.

Then DESI was added also seen in Fig. 4.15. The addition of the DESI data did not seem to affect the BA model when the recently released Planck data was used, with regards to the parameters $100\theta_s$, $\ln(10^{10}A_s)$ and τ_{reio}, as the 1D curves that were obtained from the PR4 + CC + SN+SH0ES data combination overlap the 1D curves that were obtained from PR4 + CC + SN+SH0ES + DESI. While when PR3 was used, the DESI data shifted these three parameters to slightly lower values For the rest of the six ΛCDM parameters, the DESI data affects the BA parameterisation by shifting the values of ω_b and n_s to lower values and shifting

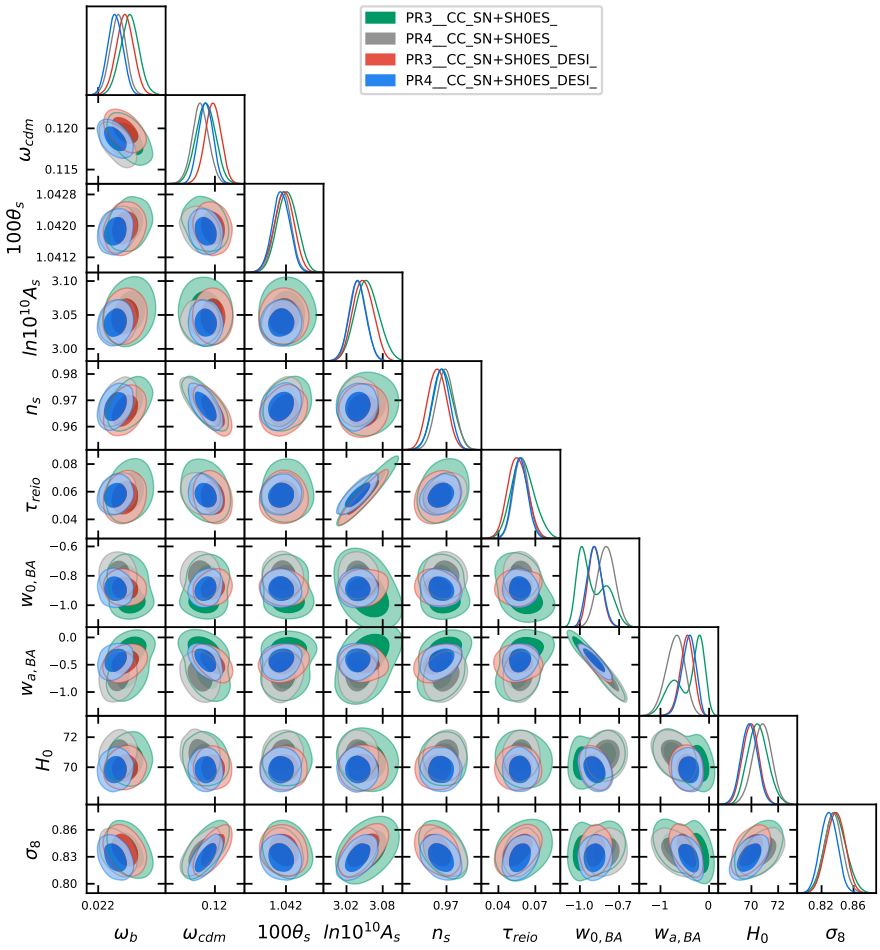

Figure 4.15: A graph of the BA model when using late-time data of CC and SN+SH0ES with PR3 seen in the green corner plot and with PR4 seen in the grey corner plot. Then the BA model was tested with the late-time data of CC, SN+SH0ES and DESI, with PR3 seen in the red corner plot and then with PR4 seen in the blue corner plot.

w_{cmd} to higher values. Fig. 4.13 showed that values of H_0 and $w_{a,BA}$ that were obtained from the BA model were lowered when DESI was used. On the other hand, the $w_{0,BA}$ was not affected by the DESI data. In Fig. 4.15, it can be seen that when DESI was added to the other late-time data and to the Planck data, the value of $w_{0,BA}$ was increased when PR3 was used and decreased when PR4 was used while the values of $w_{a,BA}$ was decreased when the previously released Planck data was used and increased when the recent CMB data was used. This decreased the discrepancies between the Planck data to the point that there is only a slight discrepancy with the $w_{a,BA}$ while there are no discrepancies with the $w_{0,BA}$ parameter as the two 1D curves overlap. As for the H_0 parameter, similar to Fig. 4.13, the DESI data shifted the parameter's value to lower values for both Planck data in a way that now the 1D curves overlap. Moving on to σ_8, the DESI data did not affect the BA model when the previously released CMB data was used but it did affect the model when PR4 was used, as the additional data pushed the parameter's value to lower values.

Correlations are seen in Fig. 4.15. A slight anti-correlation between $w_{0,BA}$ and H_0 is seen only when DESI was added to the Planck and CC + SN+SH0ES data, a strong anti-correlation is seen between $w_{a,BA}$ and $w_{0,BA}$ when late-time data combinations were added that was not present when only CMB data was used, and a slight anti-correlation is seen between H_0 and $w_{a,BA}$ when PR4 + CC + SN+SH0ES data combination was used that was not achieved when only early-time was used. The BA model also produced a correlation with all data combinations between H_0 and σ_8 which was also seen in the previous graph. However, it is not as strong as when the model was tested using only early-time data. There is another slight correlation between $w_{0,BA}$ and σ_8 that was caused by the addition of the DESI data. Also, a correlation is seen between the $w_{a,BA}$ and σ_8 parameters for all data combinations except for when PR3 + CC + SN+SH0ES was used. Following the trend of the previous plots and the previous models, the posteriors that were produced when using PR4 are smaller than the posteriors obtained from PR3, and when DESI was included it constrained the model more and produced even smaller posteriors. Subsequently, the smallest posteriors were obtained by the PR4 + CC + SN+SH0ES + DESI data combination. In addition, the posteriors show that there are no tensions between the data combinations when the BA model was used as they are all 1σ away from each other, which is like what was seen in the previous four graphs.

From Table S19 and Table S20, it is seen that the BA model does not limit to the standard model, as the values $w_{0,BA}$ and $w_{a,BA}$ are not 1σ away from -1 and 0 respectively regardless of the chosen data. The addition of the CC and SN+SH0ES was enough to constrain the H_0 and σ_8 such that their uncertainties were low-

Parameters	CC + SN+SH0ES		CC + SN+SH0ES BAO		CC + SN+SH0ES DESI	
	Best-fit	Mean	Best-fit	Mean	Best-fit	Mean
Sampled Parameters						
Ω_m	0.232	$0.278^{+0.083}_{-0.045}$	0.272	0.276 ± 0.016	0.326	0.327 ± 0.011
$w_{0,OSCILL}$	-0.85	-0.90 ± 0.11	-0.885	$-0.880^{+0.055}_{-0.062}$	-0.914	$-0.915^{+0.062}_{-0.057}$
$w_{a,OSCILL}$	-0.44	$0.50^{+0.86}_{-1.40}$	-0.07	$-0.28^{+0.57}_{-1.00}$	1.75	$1.79^{+0.67}_{-0.65}$
Derived Parameters						
H_0	72.44	72.28 ± 0.85	72.26	72.37 ± 0.88	71.78	$71.84^{+0.79}_{-0.80}$
χ^2 **Statistics**						
χ^2_{min}		1309		1322		1323
ΔAIC		0.89		-2.31		-7.48
ΔBIC		13.80		8.62		3.45

Table S21: The values of the oscillatory parameterisation when using only late-time data.

ered and the values that were obtained with PR3 are now within the expected range of past research. Thus, the four sets of values show that both H_0 and σ_8 are within the range of expected values. When looking at the ΔAIC and ΔBIC, negative values are seen when the AIC criteria was taken in the four data combinations, showing that the BA model is statistically better than the ΛCDM model. However, when the BIC criteria was taken, the BA model achieved a negative value when PR3 + CC + SN+SH0ES combination was taken but a positive value was found when PR4 was used instead of PR3. Therefore, the BA model fits the PR3 + CC + SN+SH0ES data better than the ΛCDM but the standard model fits the PR4 + CC + SN+SH0ES better than the BA parameterisation. When the DESI data was added it was found that no negative BIC values were retrieved. Also, lower values of AIC and BIC were obtained when PR3 with CC and SN+SH0ES was used meaning that the BA model fits that data better than the other data combinations.

4.6 | Oscillatory model

The oscillatory model, in short, OSCILL model, allows w to vary in an oscillatory manner. From CLASS and MontePython, the values of the six ΛCDM parameters with the additional two parameters for the reparameterisation are given and are shown in Table S21, Table S22, Table S23, and Table S24. The tables use different data set combinations to obtain a good understanding of the model and its effect on the parameters.

Parameters	PR3		PR4	
	Best-fit	Mean	Best-fit	Mean
Sampled Parameters				
ω_b	0.02249	$0.02240^{+0.00015}_{-0.00016}$	0.02222	0.02226 ± 0.00013
ω_{cdm}	0.1191	0.1198 ± 0.0014	0.1192	0.1186 ± 0.0012
$100\theta_s$	1.04170	1.04190 ± 0.00030	1.04180	1.04184 ± 0.00025
$\ln(10^{10}A_s)$	3.040	3.046 ± 0.018	3.036	3.038 ± 0.014
n_s	0.9678	$0.9658^{+0.0044}_{-0.0046}$	0.9694	0.9677 ± 0.0040
τ_{reio}	0.0520	$0.0552^{+0.0085}_{-0.0087}$	0.0580	0.0576 ± 0.0061
$w_{0,OSCILL}$	-1.39	$-1.17^{+0.07}_{-0.33}$	-0.83	$-1.30^{+0.34}_{-0.39}$
$w_{a,OSCILL}$	0.71	$1.25^{+0.08}_{-1.10}$	1.52	$0.18^{+1.30}_{-0.96}$
Derived Parameters				
H_0	83.41	$77.39^{+9.98}_{-8.03}$	69.09	79.00 ± 10.00
σ_8	0.942	$0.901^{+0.082}_{-0.067}$	0.83	$0.89^{+0.29}_{-0.27}$
χ^2 **Statistics**				
χ^2_{min}		2768		30570
ΔAIC		-0.96		2.67
ΔBIC		15.12		19.21

Table S22: The values obtained from CLASS and MontePython for the oscillatory reparametrisation model using either PR3 or PR4.

Three corner plots where each one shows pictorially the values obtained from the simulations; one when using late-time on its own; another when using early-time on its own; and lastly, when taking early-time with late-time data combinations. Starting with the late-time data, Fig. 4.16 shows the results that were obtained from the OSCILL parameterization using two different late-time data combinations. As seen in the logarithmic model, degeneracies are seen when the OSCILL parameterisation was taken specifically in the $w_{a,OSCILL}$ parameter when either DESI data or the older BAO data were used. This shows that any BAO data was required to constrain the model. The DESI data obtained a higher value of Ω_m and a lower value of H_0 when compared to the older BAO data, which is in agreement with the previously discussed models. The older BAO data did not make any changes to the H_0 parameter, as the 1D curve when the BAO data was used overlaps the 1D curve that the model produced when only CC and SN+SH0ES data was used. It can also be seen that the older BAO data also produced the same result as when CC + SN+SH0ES were used for the $w_{0,OSCILL}$ parameter. However, when the BAO data was added it made the $w_{0,OSCILL}$ more well-defined. This is also seen with the $w_{a,OSCILL}$ parameter. In this model, the DESI data obtained a higher value of $w_{a,OSCILL}$ which is the opposite of what occurred in the other wCDM models. In agreement with all the previous parameterisation mod-

Parameters	PR3 CC + SN+SH0ES		PR4 CC + SN+SH0ES	
	Best-fit	Mean	Best-fit	Mean
Sampled Parameters				
ω_b	0.02247	$0.02246^{+0.00014}_{-0.00015}$	0.02240	0.02234 ± 0.00012
ω_{cdm}	0.1187	$0.1193^{+0.0013}_{-0.0014}$	0.1173	0.1178 ± 0.0011
$100\theta_s$	1.04180	$1.04200^{+0.00029}_{-0.00030}$	1.04190	$1.04190^{+0.00025}_{-0.00026}$
$\ln(10^{10}A_s)$	3.050	$3.044^{+0.016}_{-0.017}$	3.050	3.039 ± 0.014
n_s	0.9688	$0.9672^{+0.0046}_{-0.0043}$	0.9721	$0.9700^{+0.0037}_{-0.0041}$
τ_{reio}	0.0556	$0.0549^{+0.0073}_{-0.0082}$	0.0642	$0.0588^{+0.0062}_{-0.0064}$
$w_{0,OSCILL}$	-0.812	$-0.811^{+0.064}_{-0.069}$	-0.836	$-0.863^{+0.039}_{-0.050}$
$w_{a,OSCILL}$	2.30	$2.18^{+0.52}_{-0.75}$	1.83	$1.51^{+0.43}_{-0.20}$
Derived Parameters				
H_0	71.76	$71.01^{+0.72}_{-0.73}$	71.45	$70.80^{+0.70}_{-0.71}$
σ_8	0.851	$0.845^{+0.012}_{-0.013}$	0.841	0.833 ± 0.010
χ^2 **Statistics**				
χ^2_{min}	4090		31890	
ΔAIC	-18.68		-18.00	
ΔBIC	-2.60		-2.04	

Table S23: The values that were achieved from CLASS and MonetePython when taking the OSCILL model when using CC and SN+SH0ES either with PR3 or PR4 for the observational data.

els, the DESI data has smaller posteriors than the older BAO data, showing that the DESI data is a better data set than the older BAO data set, meaning that for the rest of the results of the OSCILL model, the DESI data will be used instead of the older BAO data. Following the trend of the previous five wCDM models, there are no tensions between the datasets as the posterior of CC + SN+SH0ES + DESI were within the posteriors of CC + SN+SH0ES. From the posteriors, it can be concluded that there is an anti-correlation between $w_{0,OSCILL}$ and H_0 and a correlation when any of the two BAO data were added while an anti-correlation is seen when BAO or DESI were not used. A correlation is seen between H_0 and Ω_m when DESI or BAO data were added to the other late-time data which was seen in the w_0CDM, CPL, JBP and BA models. However, unlike what was seen in the other wCDM parameterisations, a correlation between $w_{0,OSCILL}$ and $w_{a,OSCILL}$ is seen with the two BAO data combinations and another correlation between $w_{a,OSCILL}$ and Ω_m are seen for all the data combinations. This difference is due to the equation of w that was chosen for the OSCILL model.

Moving on to analysing Table S21, the OSCILL model only limits to the standard

Parameters	PR3 CC + SN+SH0ES + DESI		PR4 CC + SN+SH0ES + DESI	
	Best-fit	Mean	Best-fit	Mean
Sampled Parameters				
ω_b	0.02251	0.02250 ± 0.00014	0.02219	0.02226 ± 0.00013
ω_{cdm}	0.1185	$0.1187^{+0.0010}_{-0.0011}$	0.11888	$0.11895^{+0.00094}_{-0.00099}$
$100\theta_s$	1.04180	1.04200 ± 0.00029	1.04190	1.04180 ± 0.00025
$\ln(10^{10}A_s)$	3.046	$3.046^{+0.015}_{-0.017}$	3.055	3.037 ± 0.014
n_s	0.9686	$0.9685^{+0.0040}_{-0.0038}$	0.9667	0.9669 ± 0.0035
τ_{reio}	0.0563	$0.0563^{+0.0075}_{-0.0085}$	0.0600	$0.0568^{+0.0059}_{-0.0061}$
$w_{0,OSCILL}$	-0.980	$-0.997^{+0.030}_{-0.027}$	-0.938	$-0.910^{+0.042}_{-0.043}$
$w_{a,OSCILL}$	-0.48	$-0.38^{+0.12}_{-0.02}$	0.92	$1.08^{+0.28}_{-0.33}$
Derived Parameters				
H_0	69.92	$69.87^{+0.61}_{-0.62}$	70.07	$69.85^{+0.60}_{-0.59}$
σ_8	0.826	$0.827^{+0.011}_{-0.012}$	0.836	0.831 ± 0.010
χ^2 **Statistics**				
χ^2_{min}		4112		31910
ΔAIC		-10.62		-8.80
ΔBIC		5.46		7.92

Table S24: The oscillatory model's values when using each Planck data with CC, SN+SH0ES and DESI data.

model when no BAO data was used, as it can be seen from the table that both $w_{0,OSCILL}$ and $w_{a,OSCILL}$ are 1σ away from 0 and -1 respectively. Once BAO or DESI data is added, the oscillatory parameterisation model no longer limits to the standard model, as only $w_{a,OSCILL}$ is 1σ away from 0. In all data combinations, the OSCILL model achieved a value of H_0 that is in the expected range of past research and its uncertainties are small. Moving on to analysing the ΔAIC and ΔBIC of the OSCILL model, it is seen that negative values of AIC were found in both data combinations that contain any BAO data. This means that the OSCILL model fits the DESI and the BAO data better than the standard model. Subsequently, a positive value of ΔAIC is seen when no type of BAO data was included showing that the standard model fits the CC + SN+SH0ES data better than the OSCILL model. When the BIC criteria was taken, the standard model fit the data better than the OSCILL model, as positive values are seen when three late-time data combinations were taken. It can also be noted that the CC + SN+SH0ES + DESI data combination obtained lower values of AIC and BIC than the CC + SN+SH0ES + BAO data combination, meaning that the OSCILL model fit the DESI data better than the other BAO data.

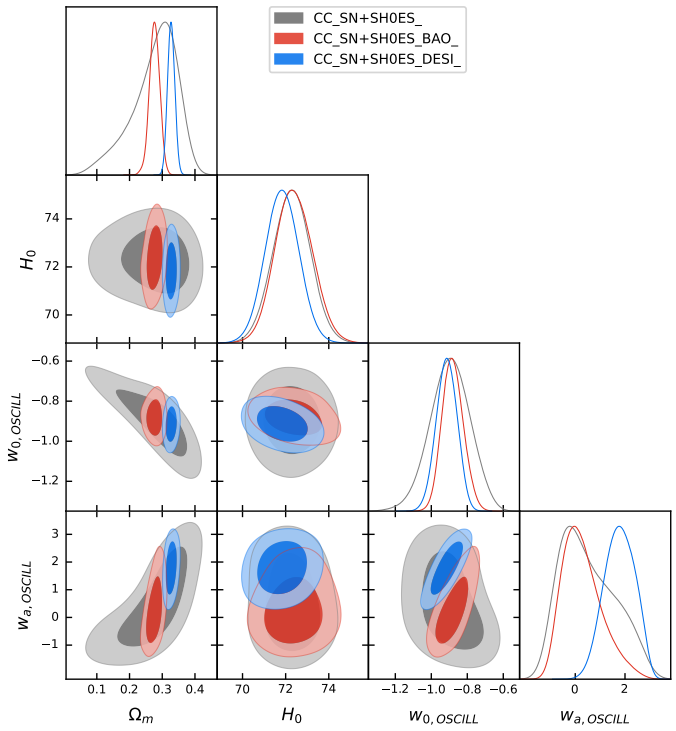

Figure 4.16: A corner plot showing the OSCILL parameterisation when using CC + SN+SH0ES, seen in the grey corner plot, then when using CC + SN+SH0ES + BAO data, seen in the red plot, and when using CC + SN+SH0ES + DESI data, seen in the blue plot.

To be able to compare the two Planck data sets without the influence of the late-time data, a plot was made, and can be seen in Fig. 4.17. For both CMB data sets, there are degeneracies in the $w_{0,OSCILL}$ and $w_{a,OSCILL}$ in both data sets. However, when the newer Planck data set was used, a complete degeneracy can be seen in the parameter of σ_8 showing that the OSCILL model did not manage to constrain the parameter at all with PR4, showing that all possible values of σ_8 are as equally likely to be true. However, when the previously released data set was used, the OSCILL model managed to constrain σ_8, showing clearly what is the most possible value of the parameter.

The complete degeneracy in σ_8 could be due to the degeneracies found in $w_{a,OSCILL}$ and due to σ_8 being defined as a derived parameter. Since this model has an oscillatory w_{OSCILL}, where $w_{a,OSCILL}$ exhibits periodic variations over time, this adds additional complexity to the evolution of dark energy. Instead of a smooth or more predictible transition like in the previous models, oscillations introduce

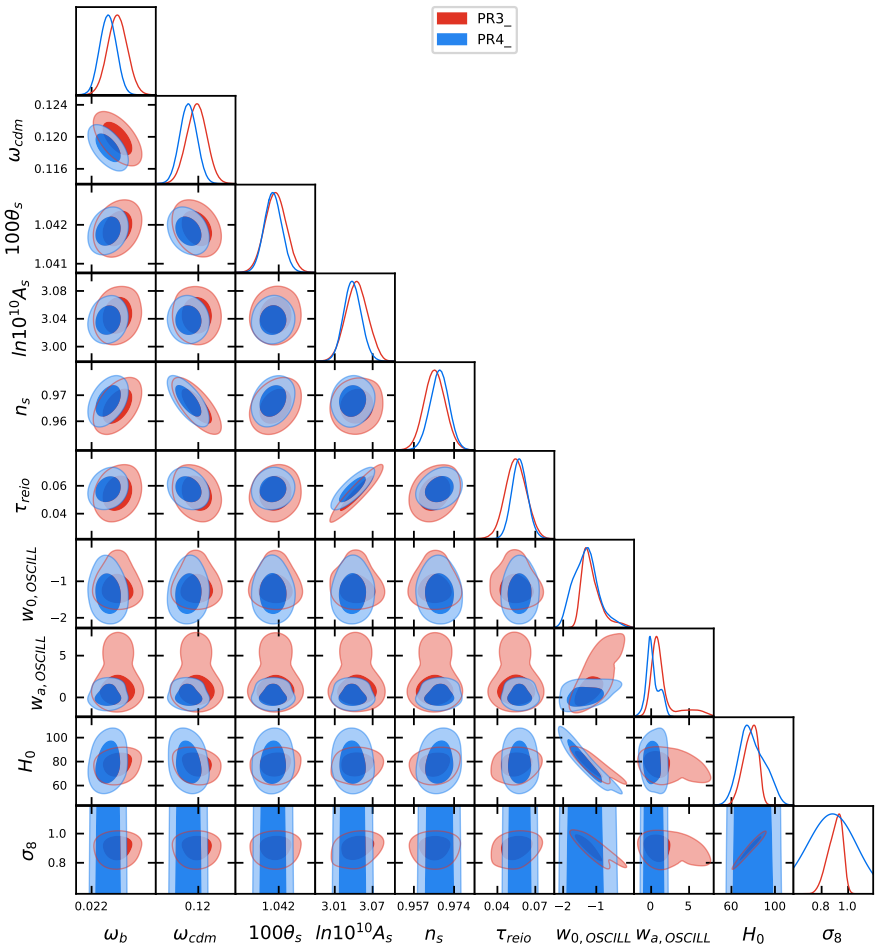

Figure 4.17: A graph showing the two CMB data sets without the influence of late-time data. The red plot shows when PR3 was used, and the blue plot shows when PR4 was used.

multiple phases of acceleration and deceleration in Universe's expansion. The oscillatory nature of the w directly affects the growth of matter perturbations, which σ_8 measures. The amplitude of matter fluctuations depends on the rate of expansion and the interplay between dark energy and matter. Therefore, degeneracies in $w_{0,OSCILL}$ and $w_{a,OSCILL}$ become even more pronounced, as they can lead to degeneracies in structure growth. There is another reason why σ_8 was completely degenerate, which is due to the data itself. The oscillatory EoS can amplify the correlation between $w_{0,OSCILL}$ and $w_{a,OSCILL}$ effectively "washing out" their individual contributions to the derived σ_8. This results in a situation where σ_8 becomes completely degenerate, not because it is inherently ill-defined, but because the data cannot constrain it uniquely within the oscillatory parameterisation framework.

There are visible differences between the values of ω_b, ω_{cdm}, $\ln(10^{10}A_s)$, n_s and τ_{reio} as PR4 has lower values of ω_b, ω_{cdm}, $100\theta_s$ and $\ln(10^{10}A_s)$, while it has higher value of n_s and τ_{reio} than PR3. The OSCILL model produced lower values of $w_{a,OSCILL}$ and H_0 when the recently released data set was used, while both Planck data sets seem to roughly agree on the most probable value of $w_{0,OSCILL}$ despite the degeneracies. Following the trend of the other models, the posteriors and the 1D curves that were obtained when using the recently released data set are smaller than the posteriors that were obtained for the previously released data set except for $w_{0,OSCILL}$, H_0 and σ_8. This shows that the older data set only constrained the model better than the newer data set for the parameters of $w_{0,OSCILL}$, H_0 and σ_8; for the rest of the parameters, PR4 constrained the OSCILL better. From the posteriors, it can also be concluded that there are no tensions between the Planck datasets as the posteriors are overlapping or intersecting each other, this was seen in all the other previously discussed wCDM models. An anti-correlation is seen in both data sets between the parameters of H_0 and $w_{0,OSCILL}$. On the contrary, the OSCILL parametrisation produced an anti-correlation between σ_8 and $w_{0,OSCILL}$ and a strong correlation between H_0 and σ_8 when PR3 was taken.

From Table S22 it can be concluded that despite the large degeneracies seen when PR4 was used, the OSCILL model limits to the ΛCDM model only when the recently released Planck data was used, as $w_{0,OSCILL}$ and $w_{a,OSCILL}$ are 1σ away from -1 and 0 respectively. This is not the case when the previously released Planck data was used, as the OSCILL parameterisation does not limit to the standard model since both parameters are not 1σ away from the values of the standard model. It can also be noted that both values of H_0 are higher than the expected range of possible values that H_0 can have. Also, large uncertainties are seen for H_0 and σ_8, especially when PR4 was used. This correlates to the degen-

eracies that were seen when the PR4 data set was used. When looking at the values of σ_8 that were obtained from the two CMB data sets, it seems like when using PR3 the OSCILL model achieved a high value which was outside the expected range of past research. On the other hand, when using PR4 the OSCILL model obtained a value of σ_8 that was within the expected range, despite the model not being able to constrain the parameter when the PR4 data was used. Shifting the focus to ΔAIC and ΔBIC, it can be concluded that only when PR3 data was used and the AIC criteria was taken, a negative value was retrieved. This means that only in that case was the OSCILL model statistically better than the standard model. For the rest of the cases, the standard model fits the data better than the OSCILL parameterisation. Similar to the previous models, the OSCILL model fits the PR3 data better than the PR4 data.

The late-time data was added to the OSCILL model with the Planck early-time datasets. The first thing that can be noticed is that with the addition of the CC and SN+SH0ES data, the OSCILL managed to constrain the σ_8 parameter with PR4 unlike what was seen in the previous graph when only PR4 was used. It can also be seen that with the addition of the late-time data, there are no longer any degeneracies with $w_{a,OSCILL}$. However, degeneracies are still seen with this parameter when PR4 was used. When looking at the six ΛCDM parameters it can be seen that following the trend of the previous graph, with the newer Planck data, the OSCILL model achieved lower values of ω_b, ω_{cdm}, $100\theta_s$ and $\ln(10^{10}A_s)$ while higher values of n_s and τ_{reio} than PR3. Moving on to the analysis of the two wCDM parameters, it can be found that the OSCILL parameterisation achieved lower values of $w_{0,OSCILL}$ and $w_{a,OSCILL}$ when PR4 was used than when the older CMB data was used. A similar thing happened for the H_0 and σ_8 parameters.

Then DESI data was added with the late-time data of CC and SN+SH0ES, for the analysis of the effect of the DESI data when the OSCILL model. It can be noted that the DESI data affected the six ΛCDM parameters by lowering the value of ω_b, $100\theta_s$ and n_s when PR4 was used but increased when PR3 was used, which resulted in the difference in the values achieved from the two Planck data sets to increase for ω_b and $100\theta_s$ while decreasing the difference for the n_s parameter. The addition of the DESI data also affected the ω_{cdm} parameter by increasing the value that was produced by the recently released Planck data and decreasing slightly the value that was obtained when the other Planck data was used. The τ_{reio} parameter was also affected by pushing the parameter to lower values only when PR4 was used as the DESI data did not seem to have affected the parameter when the previously released data set was used. The additional late-time data also did not have any effects on the $\ln(10^{10}A_s)$ parameter as the 1D curve of PR4 + CC + SN+SH0ES + DESI overlaps the 1D curve of PR4 + CC + SN+SH0ES

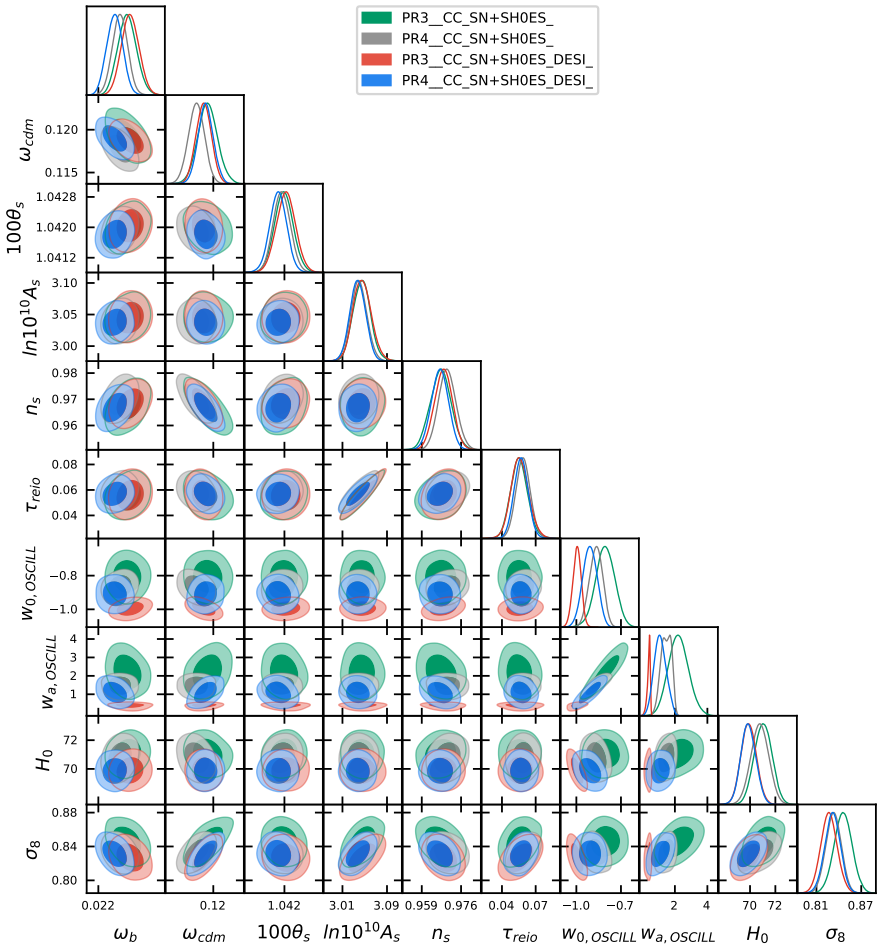

Figure 4.18: The graph shows four overlapping corner plots of the OSCILL model using the two Planck data sets with combinations of late-time data. PR3 + CC + SN+SH0ES is depicted in the green, PR4 + CC + SN+SH0ES is seen in the grey corner plot, PR3 + CC + SN+SH0ES + DESI is seen in the red corner plot, and PR4 + CC + SN+SH0ES + DESI is seen in the blue corner plot.

and the same occurred for when PR3 was used instead of PR4. When the OSCILL model was tested with only late-time data seen in Fig. 4.16, the DESI data had affected the OSCILL model as it lowered the value of H_0 and increased the value of $w_{a,OSCILL}$, while keeping the parameter $w_{0,OSCILL}$ the same. When DESI was used with early-time data it resulted in the OSCILL model achieving lower values of $w_{0,OSCILL}$, $w_{a,OSCILL}$, H_0 and σ_8 where the two Planck data sets obtained the same 1D curve for H_0. It can also be seen that the DESI data constrained the $w_{a,OSCILL}$ parameter more such that no degeneracies were obtained by the OSCILL model when PR4 was used.

Correlations and anti-correlations are seen in Fig. 4.18. When only late-time data was used, in Fig. 4.16, an anti-correlation between $w_{0,OSCILL}$ and H_0 and a correlation between $w_{0,OSCILL}$ and $w_{a,OSCILL}$ were found. Following the trend of the previous models, when late-time was added to the early-time data, the OSCILL model produced a strong correlation between $w_{a,OSCILL}$ and $w_{0,OSCILL}$ and a slight correlation between H_0 and σ_8 in all late-time data combinations. This correlation was also seen in the previous graph but when only early-time data was used, this correlation was stronger. A slight anti-correlation can be seen between H_0 and $w_{0,OSCILL}$ when PR4 was used. However, a stronger anti-correlation is present when the PR3 + CC + SN+SH0ES + DESI data combination was used even though this anti-correlation is not seen when only PR3 + CC + SN+SH0ES data combination was used. The anti-correlation that can be seen between $w_{0,OSCILL}$ and σ_8 is only visible when PR3 + CC + SN+SH0ES + DESI and PR4 + CC + SN+SH0ES data combinations were used. The OSCILL model also produced a slight correlation between $w_{a,OSCILL}$ and σ_8 only when PR4 + CC + SN+SH0ES + DESI and PR3 + CC + SN+SH0ES data sets were used. Following the trend of all the previously discussed models, the OSCILL parameterisation produced smaller posteriors when the DESI data was used. However, this model obtained the smallest posteriors for the parameters of $w_{a,OSCILL}$ and $w_{0,OSCILL}$ when the previously released Planck data was used with DESI while for the rest of the parameters, the OSCILL model obtained smaller posteriors when the PR4 + CC + SN+SH0ES + DESI data combination was used. Thus, the PR3 + CC + SN+SH0ES + DESI constrained the $w_{0,OSCILL}$ and $w_{a,OSCILL}$ parameters better than when PR4 data set was used instead of the older data set, while the PR4 + CC + SN+SH0ES + DESI constrained the six ΛCDM model parameters, H_0 and σ_8 better than the previously released early-time data. Like in the previous models, no tensions with the data combinations when the OSCILL model was used can be seen in Fig. 4.18.

From Table S23 and Table S24 it can be seen that when late-time data was added to the OSCILL model, the model no longer limits to the standard model when PR4

was used as $w_{0,OSCILL}$ is only 1σ away from -1 when PR3 + CC + SN+SH0ES + DESI was used. In the case of the other data combinations, $w_{0,OSCILL}$ is not 1σ away from -1. For all the data combinations $w_{a,OSCILL}$ is not 1σ away from 0. This means that the OSCILL model did not manage to limit to the standard model in any of the data combinations. The addition of the late-time data helped lower the values of H_0 and σ_8 to be within the expected range of past research. Also, the addition of the late-time data did lessen the uncertainties of these four parameters, which was expected. When the AIC and BIC criteria were calculated it was found that the OSCILL model fits the PR3 + CC + SN+SH0ES + DESI and the PR4 + CC + SN+SH0ES + DESI data better than the ΛCDM model as both ΔAIC and ΔBIC were negative. On the other hand, when the OSCILL was tested with PR3 + CC + SN+SH0ES and PR4 + CC + SN+SH0ES, the ΔAIC was found to be negative, while the ΔBIC was found to be positive. This means that the OSCILL model was statistically better than the standard model with the AIC criteria, while for the BIC criteria, the ΛCDM model was statistically better than the OSCILL parameterisation. Out of all the four data combinations, the OSCILL model fit the PR3 + CC + SN+SH0ES data combination the best, as it obtained the lowest AIC and BIC values.

4.6.1 | Conclusion

In conclusion, CLASS and MontePython were used to generate results and corner plots which represent the results of the wCDM parameterization models: the constant model (w_0CDM), the linear model (CPL), the quadratic model (JBP), the logarithmic model (GE), the factorial model (BA) and the oscillatory model (OSCILL). Three tables were made, showcasing the values of the models when using different dataset combinations. Two corner plots were made for the analysis of each model and two corner plots were generated for the analysis of the two different Planck data sets.

From these tables and graphs, the posteriors showed anti-correlations as well as a correlation. The effect of the addition of the late-time data on the early-time data on the parameters was analysed. From the tables, it was determined if a model limits to the ΛCDM model when a particular data set was used. The ΔAIC and ΔBIC were analysed and for particular data, negative values were found, showing that for that data combination, the model fits the data better. The AIC and BIC for the two Planck data were compared to see if the model fit the recently released data set better than the previously released data.

In this chapter, it was seen how the models do not constrain well when only early-time was used, in fact some of them did not manage to converge with the

Gelman-Rubin statistics. As discussed, this was expected as the wCDM models only affect the late Universe, and also the same was seen in the paper the models were taken from [123, 78]. Out of the six models, the model that took the longest to obtain all the results was the OSCILL model, this was to be expected as it varies more than the other models. The first model to get all the results, apart from the ΛCDM was the logarithmic model. This could be due to it having narrow priors, much more than the other models, since positive values were not taken due to stability reasons [123]. Also, when comparing the results that were achieved from the six wCDM models, the constant model obtained the least degeneracies as the model only had degeneracies with the $w_{0,w0CDM}$, H_0 and σ_8 when the PR4 data was used by itself. The models will be compared further, the final conclusions will be made in the following, final chapter.

5

Conclusion

In this project, the tensions within the ΛCDM model were explored, specifically focussing on the discrepancies in the values of the H_0 parameter and the σ_8 parameter. To address these tensions, the wCDM model, a dynamic extension of reparametrisation of the standard model, was investigated using six different parametrisations of w. These models allow for variations in the dark energy equation of state parameter, w, offering a potential solution to the inconsistencies between early-time and late-time data. Table S1 shows the wCDM parametrisation models that were considered in this project and their respective equations of state of dark energy.

Observational datasets were used which include CMB Planck data for the early-time data, while CC and SN+SH0ES data were used as well as BAO transverse data for the late-time data. The opportunity was taken to test the recently released Planck data set of PR4 with the previously released one of PR3. During this project, the DESI data was also compared to the previously released BAO

Name of wCDM parametrisation model	Equation of state of dark energy w
Constant model	$w_{w0CDM}(a) = w_{0,w0CDM}$
Linear model	$w_{CPL}(a) = w_{0,CPL} + w_{a,CPL}(1-a)$
Quadratic model	$w_{JBP}(a) = w_{0,JBP} + w_{a,JBP}\, a(1-a)$
Logarithmic model	$w_{GE}(a) = w_{0_{GE}} - w_{a_{GE}} \ln(a)$
Barboza and Alcaniz model	$w_{BA}(a) = w_{0_{BA}} + w_{a_{BA}} \left[\frac{1-a}{2a^2-2a+1}\right]$
Oscillatory model	$w_{OSCILL}(a) = w_{0,OSCILL} + w_{a,OSCILL} \left[a \sin\left(\frac{1}{a}\right) - \sin(1)\right]$

Table S1: A table showing the list of models that were considered and their respective equation of state of dark energy w.

data, and conclusions were made about the data. The theoretical predictions for the tested models were computed using the CLASS software, MontePython was utilized for Bayesian statistical analysis and GetDist was used for the plotting of the corner plots. CLASS and MontePython had to be modified for the implementation of the six models and the implementation of the data sets that were not inbuilt. This approach ensured robust testing of the wCDM models with the use of the observational data.

Despite the models being left for months even to converge, there were some models that did not converge when only early-time data was taken. The Barboza and Alcaniz model and the quadratic model did not manage to converge when only early-time data were given, as neither PR4 nor PR3 were able to converge the model with the Gelman-Rubin statistics. Similarly, the linear model also did not manage to constrain all the parameters when PR4 was taken by itself. However, it was constrained when the previously released CMB data was used. On the contrary, even though the oscillatory model managed to converge with the Gelman-Rubin statistics when PR4 on its own was used, the σ_8 parameter was completely degenerate, showing that despite converging, the oscillatory model did not manage to constrain the parameter at all. It was discussed that this complete degeneracy could have been due to the degeneracies that the oscillatory model had in the $w_{a,OSCILL}$ parameter and due to the fact that σ_8 was taken to be a derived parameter, or, it could be due to the data itself and the oscillatory behaviour of w, making it harder to predict certain parameters. This complete degeneracy was not produced when only PR3 was used. For the rest of the data combinations and models, there were no complete degeneracies with any of the parameters.

However, degeneracies were still seen with w_0, w_0, H_0 and σ_8 with particular data combinations. For instance, other degeneracies were seen with the oscillatory model with the parameter $w_{a,OSCILL}$ when CC + SN+SH0ES was used, when PR4 + CC + SN+SH0ES was used and when PR4 or PR3 were used. When the oscillatory model was tested with the PR4 data set, degeneracies were also seen in the $w_{0,OSCILL}$ parameter. The Barboza and Alcaniz had degeneracies with the $w_{0,BA}$ and $w_{a,BA}$ parameters when PR4, PR3 and PR3 + CC + SN+SH0ES were used. The logarithmic model obtained degeneracies with the parameters H_0 and σ_8 when PR4 + CC + SN+SH0ES was used and when DESI was added to that data combination.

The logarithmic parameterisation had degeneracies with the $w_{a,GE}$ parameter when only combinations of late-time were taken and when only early-time data was used. When combinations of late-time data were taken the logarithmic model

also depicted degeneracies in the H_0 parameter. When PR4 was used with the quadratic model, degeneracies were seen in all of the four parameters of $w_{0,JBP}$, $w_{a,JBP}$, H_0 and σ_8 while when the late-time data of CC and SN+SH0ES with PR4, the quadratic model managed to constrain H_0 and σ_8 but degeneracies were still seen with $w_{0,JBP}$ and $w_{a,JBP}$. Degeneracies with these parameters were also seen when the quadratic model was tested with PR3 by itself but not when late-time data was used with PR3. Degeneracies with these two parameters were also present with the linear model when only Planck data was used as the observational data. When CC and SN+SH0ES were added to the Planck data, the linear model managed to constrain the $w_{a,CPL}$ parameter, but PR3 still did not manage to constrain $w_{0,CPL}$, while PR4 did. In the case of the constant model, degeneracies were only seen when only the recently released Planck data was used with the parameters of $w_{0,w0CDM}$, H_0 and σ_8, while the model constrained all the parameters with the other data combinations.

This research also aimed to test the newer Planck dataset as well as the newer BAO transverse data this being the DESI data. In all the models, regardless of the data combinations that were tested, it was consistently seen that the DESI dataset obtained smaller posteriors were obtained, showing that it is more precise than the older BAO data. The same was seen with PR4, as it had obtained smaller posteriors than when PR3 was used, showing that the recently released Planck data is more precise than the previously released one. However, the oscillatory model and the quadratic model did not follow this with the w_0, H_0 and σ_8, parameters as for those particular parameters the PR3 had smaller posteriors than PR4. The quadratic model had not converged with the Gelman-Rubin criteria, when only early-time data was used, so it could be the case that PR3 obtained smaller posteriors for these three parameters because it had not reached the state of convergence. In fact, the smallest posteriors were obtained when PR4 + CC + SN+SH0ES + DESI data combination was used. The only exception to this was for the oscillatory model, as for that particular model, the smallest posteriors for the $w_{0,OSCILL}$ and $w_{a,OSCILL}$ were obtained with the PR3 + CC + SN+SH0ES + DESI data combination, for the rest of the parameters, the oscillatory model had the smallest posteriors with the PR4 + CC + SN+SH0ES + DESI. Therefore, in general, PR4 and DESI both seemed to constrain the models better, as tighter constraints were seen when compared to their predecessor. This shows that the newer datasets had less systematic errors and less noise. In Chapter 4, it was seen that there were no tensions between the datasets of SN+SH0ES with SN+SH0ES + DESI and SN+SH0ES + BAO, and no tensions between the Planck datasets, as the posteriors intersect each other.

Since the newer Planck dataset was tested, the six ΛCDM parameters were dis-

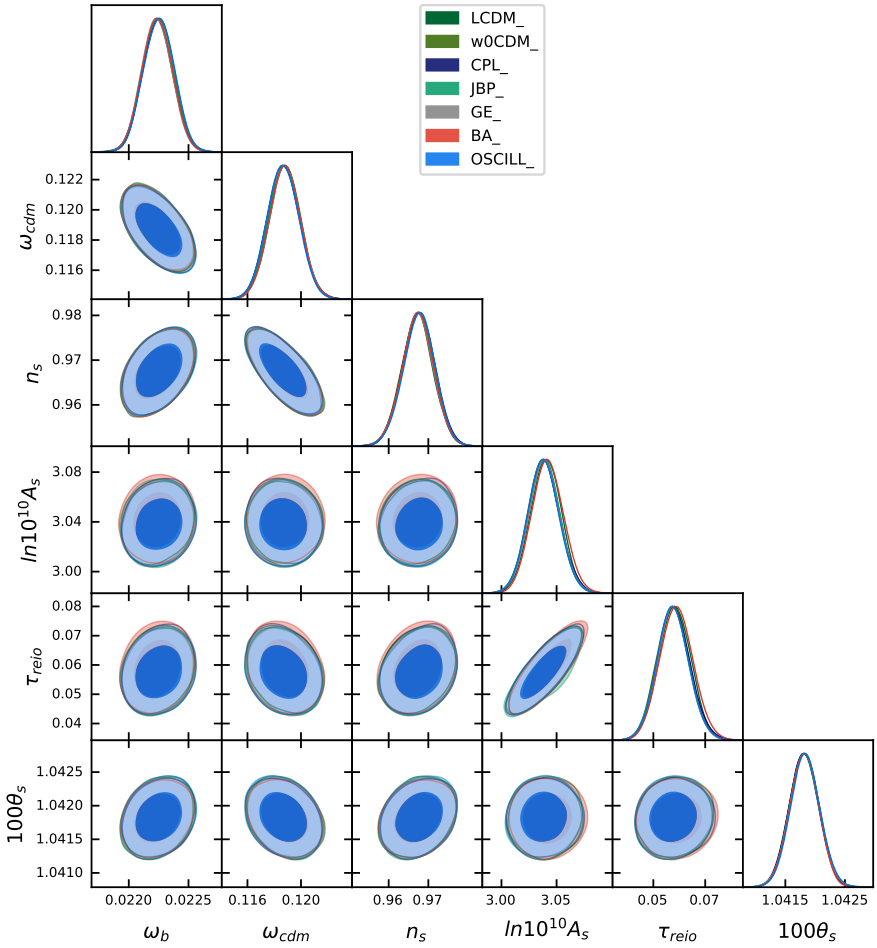

Figure 5.1: A graph showing seven overlapping corner plots, showcasing the six ΛCDM parameters that were retrieved from the standard model and the six wCDM models.

cussed. To showcase the results that were achieved from the different models, two corner plot were generated. The first corner plot shows the six ΛCDM parameters that were retrieved from the ΛCDM model and the six wCDM models when the newer Planck dataset was used, seen in Fig. 5.1. The second corner plot shows the six parameters of the standard model and of the tested models when PR4 + CC + SN+SH0ES + DESI data combination was used, seen in Fig. 5.2.

Fig. 5.1 shows that when only early-time data was used, none of the wCDM models affected the six ΛCDM parameters as the 1D curves of all the wCDM reparameterisation models overlap perfectly the 1D curves of the standard model, and the

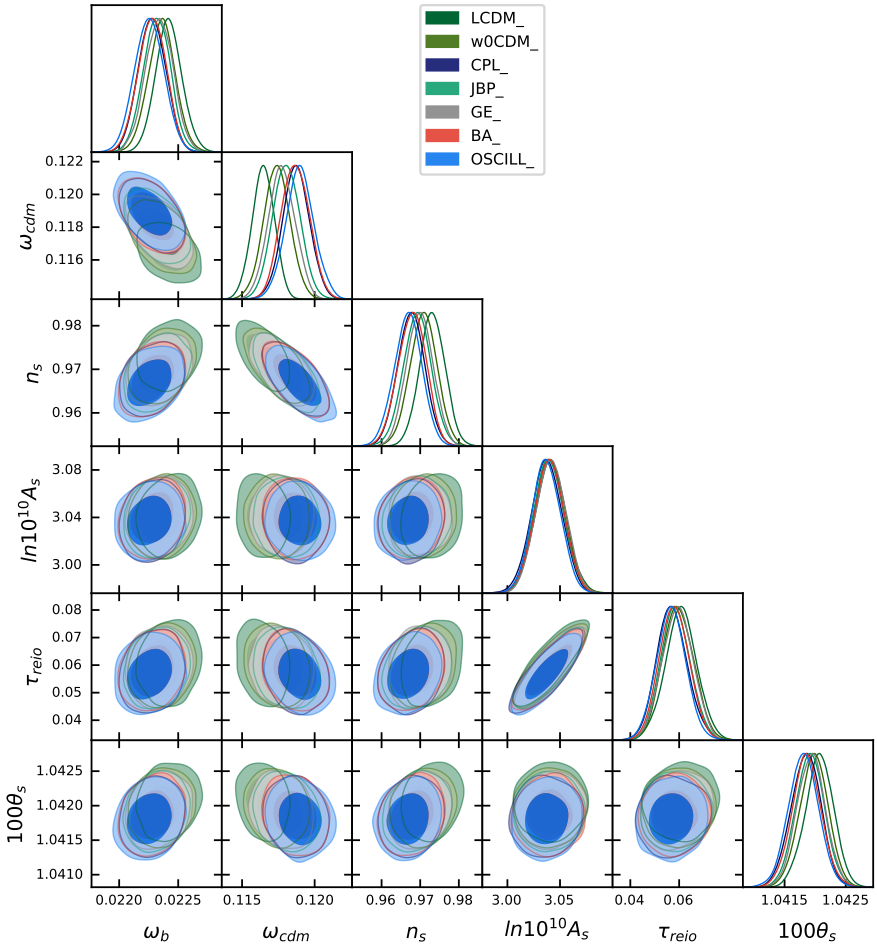

Figure 5.2: A graph overlapping seven corner plots, showing the six ΛCDM parameters that were achieved from the standard model and the six wCDM models that were tested in this project.

posteriors that were calculated from the tested models overlap almost perfectly the posteriors obtained from the ΛCDM model. This was also seen in the paper the models were taken from, as the paper also showed that when early-time data PR3 was used, the wCDM models did not impact the six ΛCDM parameters in any way.

When late-time data of CC, SN+SH0ES and DESI was added to the models, seen in Fig. 5.2, the models produced different values of the ΛCDM parameter than the ΛCDM model. The only parameter that was not affected was the $\ln(10^{10}A_s)$ parameter as the 1D curves overlap each other almost perfectly. The correlations

and anti-correlations that were present in the previous graph were not affected by the additional data. Despite the models achieving different values, from the posteriors of the parameters it can be seen that the values of the different models, seem to be 1σ away from each other. This means that the tested models, with respect to the six ΛCDM parameters, are 1σ away from each other, and, subsequently, 1σ away from the standard model. Comparing Fig. 5.1 to Fig. 5.2, it can be seen that when early-time and late-time data were used, the wCDM models were 1σ away from when only early-time was taken.

Two whisker plots were made so that the results that were obtained when only using background data were grouped together and the results that were achieved when using early-time and early-time with combinations of late-time were grouped together to make it easier to compare the reparametrisation models. The code of the whisker plot is public [1]. However, the code had to be changed to accommodate the results and the format of this project. The two whisker plots can be seen in Fig. 5.3 which shows the whisker plot of the wCDM parametrisation models when only late-time data was used and Fig. 5.4 shows the whisker plot of the reparameterisation models when only early-time data was used and combinations of early-time with late-time.

Fig. 5.3 shows that when only late-time data was used, the wCDM models consistently constrained w_0 such that very low uncertainties were obtained except for the w_0CDM model when DESI was included. When looking at the w_a parameter, the logarithmic model obtained the lowest uncertainties and was to closest to the value of the standard model. The CPL and OSCILL models produced the highest uncertainty range. For H_0, the reparameterisation models except for the BA model, roughly obtained the same uncertainty range as the ΛCDM model.

Fig. 5.4 shows that, in general, when only early-time data was used, the wCDM parameterisation model had larger uncertainties than when combinations of late-time data were added. This shows how the wCDM models need late-time data to constrain these four parameters. Also, in the paper the models were taken from [123, 78], degeneracies were seen with the parameters w_0, w_a, H_0 and σ_8, thus, it was expected that degeneracies would show up in this project too. The parameters, w_0, H_0 and σ_8 vary less from model to model when late-time data was added to the CMB data. When late-time was added with the Planck data, the values of w_0 seem to vary around -1, H_0 seems to vary around 70, and σ_8 seems to vary between 0.8 and 0.9. The logarithmic model (GE) obtained larger uncertainties and achieved lower values of H_0 and σ_8 than the other models when the PR4 was used. The largest uncertainties that were obtained were from the CPL

[1] Link to the public whisker plot code: https://github.com/lucavisinelli/H0TensionRealm

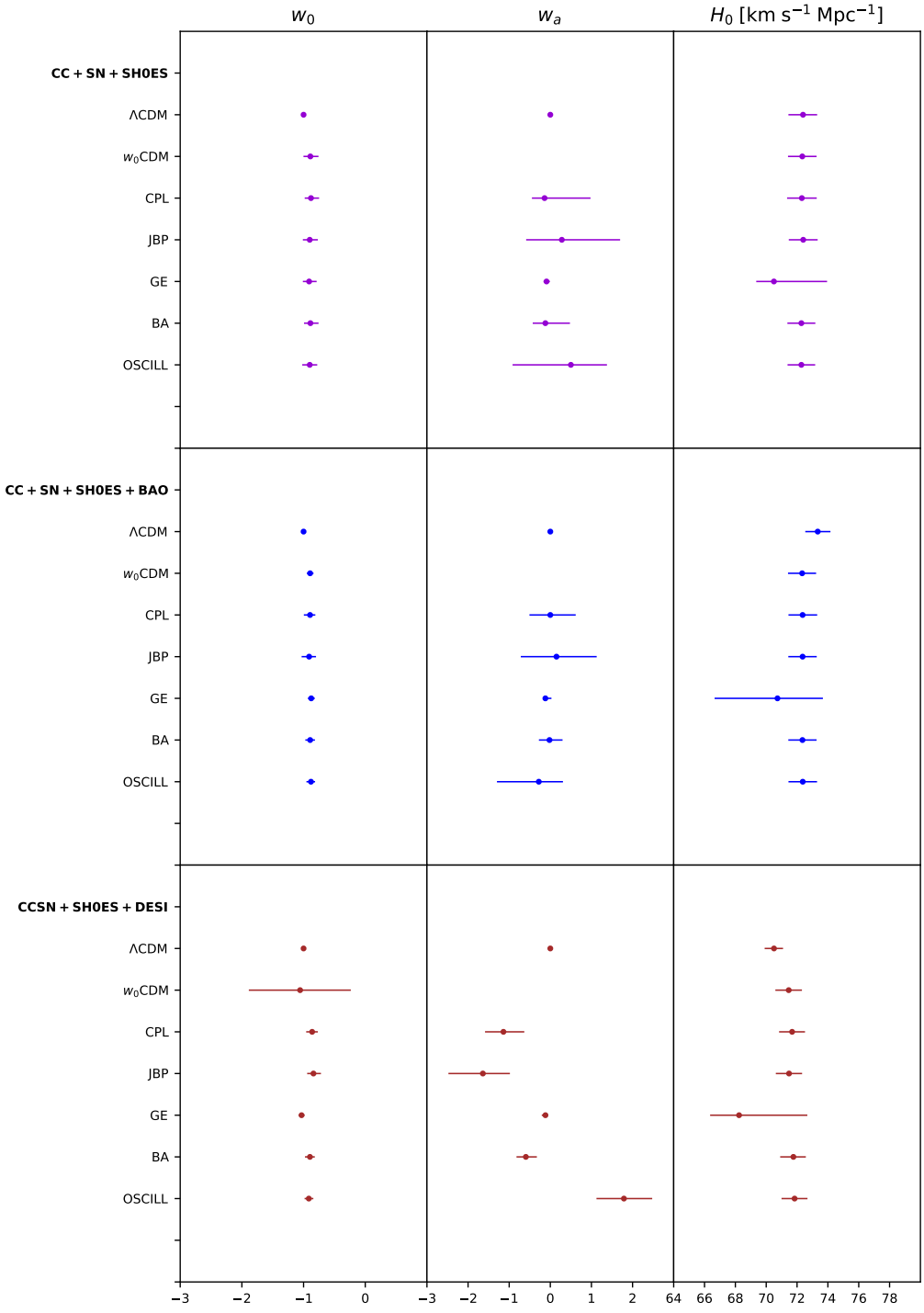

Figure 5.3: A whisker plot [35] showing the results that were obtained from the different wCDM models as well as the ΛCDM models only different combinations of late-time data were used.

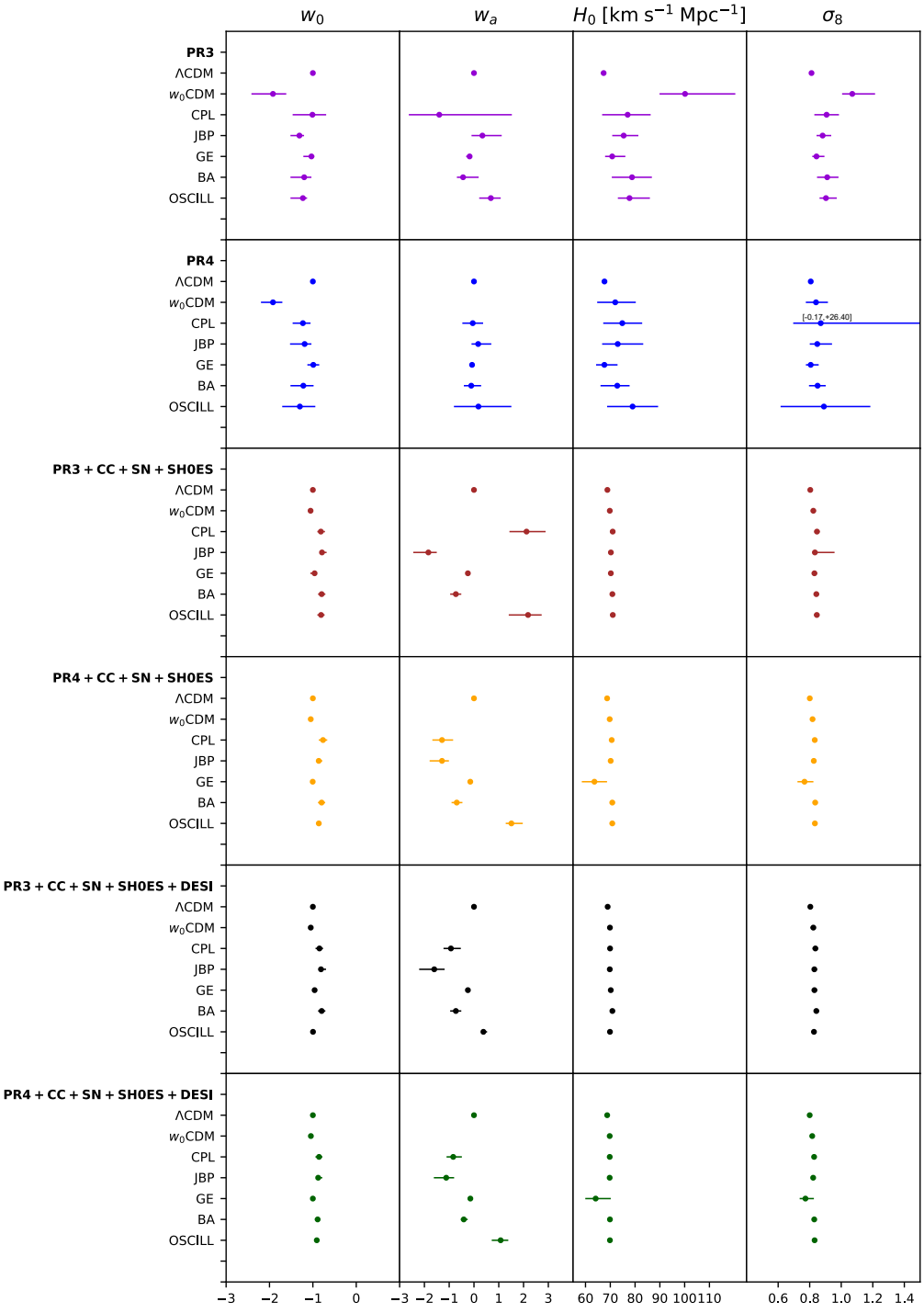

Figure 5.4: A whisker plot [35] showing all the values that were achieved with the wCDM reparametrisation models and the standard model when using early-time and early-time with late-time combinations.

wCDM models	CCSN	CCSNBAO	ALL	PR3	PR4	PR3/CCSN	PR4/CCSN	PR3/ALL	PR4/ALL
Constant	0.91	-4.38	-0.65	-4.40	1.80	-4.44	-1.40	-3.24	-1.00
Linear	0.63	-2.39	-5.69	-3.08	2.80	-20.16	-14.40	-12.08	-8.20
Quadratic	0.61	-0.38	-3.71	0.58	3.60	-11.36	-8.40	-9.48	-6.40
Logarithmic	0.93	4.02	-1.86	1.72	3.00	-11.54	-6.00	-25.52	-4.60
Barboza & Alcaniz	0.68	-2.40	-6.33	-0.20	2.60	-16.70	-14.20	-14.28	-9.40
Oscillatory	0.89	-2.31	-7.48	-0.96	2.67	-18.68	-18.00	-10.62	-8.80

Table S2: The table shows the values of the ΔAIC that were obtained from the six wCDM parametrisation model for each data combination.

model, which is the linear model when only Planck data was used, especially in the parameter of σ_8 when the PR4 was used and w_a when PR3 was used. It can be seen in Fig. 5.4, that w_a varies significantly depending on the model and the data combination that was taken.

Since the results of the w_0 and w_a for all the models generally had small uncertainty bars, only a few managed to be 1σ away from -1 and 0 respectively to limit to the ΛCDM model. The constant model, the linear model, the quadratic model and the oscillatory model all limited to the standard model when only the late-time data of CC + SN+SH0ES was used without any early-time data. The constant model and the oscillatory model also limited to the standard model when only early-time data of PR4 was used, the quadratic model limited to the standard model when CC + SN+SH0ES + BAO was used, while the linear model limited again to the ΛCDM model when only the early-time data of PR3 was used. The Barboza and Alcaniz model was able to limit to the ΛCDM model when the latest Planck dataset was taken on its own. On the other hand, the logarithmic model did not manage to limit to the standard model with any of the data combinations that were taken.

Two tables were made for a better comparison of the ΔAIC and ΔBIC that were calculated for each model for each data set combination that were taken. The first column of both tables shows the list of wCDM models that were taken in this project, while the first row shows the data combinations that were taken for each model. Fig. S2 shows the values of ΔAIC and Fig. S3 shows the values of ΔBIC where CCSN is short for CC + SN+SH0ES, CCSNBAO is short for CC + SN+SH0ES + BAO, ALL is short for CC + SN+SH0ES + DESI, PR3/CCSN is short for PR3 + CC + SN+SH0ES, PR4/CCSN is short for PR4 + CC + SN+SH0ES, PR4/ALL refers to PR4 + CC + SN+SH0ES + DESI and PR3/ALL refers to PR3 + CC + SN+SH0ES + DESI.

wCDM models	CCSN	CCSNBAO	ALL	PR3	PR4	PR3/CCSN	PR4/CCSN	PR3/ALL	PR4/ALL
Constant	6.37	1.09	4.81	10.04	9.90	3.60	6.96	4.80	7.36
Linear	13.55	8.54	5.24	13.00	19.41	-4.08	2.32	4.00	8.52
Quadratic	13.52	1.09	7.22	16.66	20.32	4.72	8.32	6.60	10.32
Logarithmic	13.84	14.95	9.06	17.80	19.61	4.54	10.72	-9.44	12.12
Barboza & Alcaniz	13.59	8.53	4.60	15.88	19.21	-0.62	2.52	1.80	7.32
Oscillatory	13.80	8.62	3.45	15.12	19.21	-2.60	-2.04	5.46	7.92

Table S3: A table showing the values of the ΔBIC that were obtained for each data combination of each wCDM model.

Table S2, shows that when each model was tested with CC and SN+SH0ES, the models had higher values of AIC than the standard model meaning that the ΛCDM model fits the CC and SN+SH0ES data better than any of the reparametrisation models. The standard model also fits the PR4 data better than the tested models as the standard model. On the other hand, positive values of ΔAIC are seen in all the models when CC + SN+SH0ES + DESI, PR3 + CC + SN+SH0ES, PR4 + CC + SN+SH0ES, PR3 + CC + SN+SH0ES + DESI and PR4 + CC + SN+SH0ES + DESI data combinations were used. Thus, when DESI was used and when late-time data was added to the Planck data, the wCDM models fit those data combinations better than the standard model. When CC + SN+SH0ES + BAO was taken only the logarithmic model had a higher value of AIC than the standard model. The rest of the models fit the CC + SN+SH0ES + BAO better than the standard model. When comparing the models' values of ΔAIC that took CC + SN+SH0ES + BAO as the observational data with when the models took CC + SN+SH0ES + DESI as the data, it can be concluded that for all the models except for the constant model, lower values of AIC were achieved meaning that except for the constant model, the models fit the DESI data better than the older BAO data and better than when only CC and SN+SH0ES data was used. When analysing the values when PR3 was used, it can be seen that the constant model, the linear model, the Barboza & Alcaniz model, and the oscillatory model are statistically better than the ΛCDM model. The models seem to fit the PR3 data better than the PR4, as when PR3 was used the models obtained lower values of AIC than when PR4 was used. This is also seen when late-time data was added to the Planck data, as the wCDM models achieved lower values of AIC when combinations of PR3 were taken than when combinations of PR4 were taken.

When looking at Table S3, it can be seen that the wCDM models had more positive values than when the AIC criteria was taken. All the models retrieved a positive value of ΔBIC when only combinations of late-time data were used, when only

early-time data was taken and when PR4 + CC + SN+SH0ES + DESI was taken. This means that none of the tested models fit those data combinations better than the standard model. When the reparameterisation models were tested with PR3 + CC + SN+SH0ES as the observational data, three models achieved a negative ΔBIC: the linear model, the Barboza & Alcaniz and the oscillatory model. These models also obtained a negative value of ΔAIC, meaning that both the BIC and AIC criteria agree that the linear model, the Barboza & Alcaniz and the oscillatory model are statistically better with the PR3 + CC + SN+SH0ES data combination. When the PR4 + CC + SN+SH0ES data combination was taken, only the oscillatory model produced a negative value of ΔBIC, meaning that for both AIC and BIC criteria, the oscillatory model is more consistent with the PR4 + CC + SN+SH0ES than the ΛCDM model. Similarly, only the logarithmic model had a negative ΔBIC when the PR4 + CC + SN+SH0ES + DESI data combination was taken. Subsequently, the logarithmic model is statistically better than the standard model in the case of when the PR4 + CC + SN+SH0ES + DESI data combination is taken. It can be noted that when the BIC criteria was taken, the models achieved higher values than when the AIC criteria was used. This was to be expected, as the BIC criteria penalises the models more, as it takes into consideration the number of data points that were taken.

Each model with each data combination produced its own value of χ^2. By comparing the χ^2 with each data combination for each model it was concluded that when the PR3 data was used the wCDM models obtained a lower of χ^2 than when the recently released Planck data was used. On the other hand, when the PR4 data was used, the ΛCDM model produced a lower value of χ^2. This resulted in the wCDM model obtaining lower values of ΔAIC and ΔBIC when the PR3 was used. It could be that since PR4 is more constrained and has lower uncertainties than PR3, it is less lenient than the PR3 data. Therefore, the standard model, being more accurate, would fit the newer data set better, while the wCDM models fit the PR3 data better as it has more uncertainties, is less constrained, and is more lenient. Since DESI came out in the middle of this research the older BAO data was used and the results were retrieved when using the older BAO instead of DESI for all the models. Therefore, the χ^2 was calculated and it turned out that the χ^2 of the ΛCDM model was significantly smaller when Planck data was used with CC + SN+SH0ES + DESI than when the older BAO was used instead of DESI. In fact, the wCDM models had lower values of ΔAIC and ΔBIC when the older BAO was used than when DESI was used. Hence, similar to PR4, DESI seems to be more accurate and the standard model favours it more than the older BAO data, which was expected.

During this project, multiple challenges and changes occurred. At the start of

this research, the recently released Planck data was not implemented into MontePython; it was only implemented for Cobaya which is another simulation that handles the production of the MCMC chains. So, the first step was to change both Hillipop and Lollipop from Cobaya to MontePython. Halfway through the implementation, the implementation of Planck 2020 to MontePython was made public and therefore, the public version of Planck 2020 was used.

Since the implementation of the OSCILL model required the implementation of a numerical integral of the Ci function, a new file had to be added to CLASS. Consequently, the make file of the simulator also had to be adjusted to include the new file so that when CLASS is compiled, it also compiles the new file of the numerical integral. Thus, the Ci function was included in the make file by an object file for the function. When CLASS is compiled, the source code is translated into object files. This object file is a compiled version of the source code but still cannot be run on its own [62]. Object files are intermediate files that the linker will later combine into an executable.

The DESI data was released in April 2024. Therefore, before that, the BAO that was previously released was used and all of the models were tested using Planck data and CC, SN+SH0ES and BAO data. Conclusions for the models were made using the previous BAO data. Later on, the decision was made to redo these runs but use the DESI data instead. This resulted in the implementation of the DESI data, as the previous BAO data was already inbuilt while DESI was not. Since DESI was not inbuilt, testing of this implemented DESI was required to ensure that the implementation was done correctly. Subsequently, runs were made using only DESi data with the ΛCDM model, the w_0CDM model and the CPL model so that they would be compared to the values obtained from the paper [2]. After the results obtained agreed with the paper, more testing was made to be fully certain that the data was implemented correctly. Since DESI on its own does not manage to constrain H_0, the paper uses priors of BBN and $100\theta_s$. The paper defines BBN as $\omega_b = 0.02218 \pm 0.00055$ and $100\theta_s = 1.04109 \pm 0.00030$ [2] so the same values were implemented as priors and used in conjunction with the DESI data. Thus, the three models were run using DESI and these two priors and the results that were achieved were also compared and found to agree.

Despite the results and conclusions that were retrieved from this project, more work can be done to ensure that the wCDM models are fully explored as it could help with the H_0 and σ_8 tensions. Some of these include:

- An updated covariance matrix of the CC dataset was recently released[2]. Since the updated CC dataset is not inbuilt into MontePython it would need to be implemented. An updated dataset would give more accurate and precise results.

- Since wCDM affects only the late Universe, more late-time data would help get better results as there would be more information where the simulations could be able to make better results. Union 3 was released at the end of 2023 and updated at the end of 2024 [92] and it is a compilation of Type Ia supernovae. This data set has 2087 data points consisting of SNe Ia from 24 different datasets which is more than SN+ [86]. Therefore, Union 3 could be used instead of SN+ as it contains more late-time data points and it has been recently updated.

- The SH0ES prior was included in the late-time runs where the prior biases the value of H_0 to a specific value. Therefore, more results could be obtained by testing the models without using the SH0ES prior to see if the prior made any significant changes, or if the differences between the results obtained by the wCDM models and the ΛCDM model increase or decrease. Also, the possibility of using a different prior could be explored, such as Carnegie Supernova Project prior [48] which obtained the Hubble constant from the tip of the red giant branch which is reported as $H_0 = 69.8 \pm 1.7$ km s^{-1}Mpc^{-1}. This prior is not inbuilt into MontePython so the implementation of it would be required.

- There is lensing data which has information on gravitational lensing and it provides valuable information about the matter distribution in the universe, including both dark matter and baryonic matter. No lensing data was included in the research so that the two Planck data would be fairly compared. Therefore, another way of improving this project is by adding lensing data. The lensing data of Planck 2018 is already inbuilt. On the other hand, the lensing data of Planck 2020 is not inbuilt into MontePython but it is for Cobaya. Therefore, its implementation can be done for MontePython. Other lensing data can be used such as ACT data [87] which was published in late 2023 and also contains CMB lensing. ACT data is also inbuilt into Cobaya and not in MontePython so the implementation to MontePython could be done. Otherwise, Cobaya [108] can be used instead of MontePython so that the updated dataset would be readily inbuilt.

[2]The link to the updated CC covariance matrix can be found in the link: https://gitlab.com/mmoresco/CCcovariance

- In past research, discrepancies were found between PR3 and ACTDR4 [54]. Therefore, possible work can be done in looking into the full data of ACTDR6 which will be released in the future, by replacing Planck data and comparing the results to see if there is any discrepancies between the newer ACTDR6 data and the recently released Planck data PR4.

- For this project, all the models only affected the late Universe. Hence, models that affect the early Universe, such as the Early Dark Energy (EDE) model [104] can be explored. This model proposes that a small fraction of dark energy was present in the early Universe, typically around the epoch of matter-radiation equality, which contributed to the Hubble rate in the pre-recombination era, which in turn decreased the sound horizon [85]. The EDE model is only half inbuilt in CLASS, so the rest of the implementation would need to be done.

- In this project the chosen wCDM models all had the equation of state which defines the model. However, there are wCDM parameterisations that use Friedmann equations instead of EoS [122] and as a result would make the computational side more complex. This means more researched models can be tested such as Generalized Chaplygin gas model, New generalized Chaplygin gas model, New agegraphic dark energy model, and the Holographic dark energy model [125]. There is research that shows that these models could be possible solutions to the H_0 tension [98].

- In this project, a more traditional method of machine learning was taken due to it being less computationally complex. However, modern and more popular techniques, such as neural networks [113, 124] can be used for the estimation of the parameters and possibly improve the results of the tested models, especially the ones that could not converge or had completely degenerate parameters. This could open the possibility of comparing traditional techniques to modern ones.

The wCDM model explores the nature of dark energy, which constitutes about 70% of the Universe. By studying its dynamic equation of state, researchers can investigate whether dark energy is a cosmological constant or something more complex, potentially reshaping our understanding of the Universe's expansion. This research demonstrated that while ΛCDM remains the better model for understanding the Universe's evolution, specific wCDM models fit certain dataset combinations better than the standard model. This could suggest that a dynamical dark energy component could possibly play a role in resolving these tensions. This research also revealed certain issues some of the popular models

such as CPL and OSCILL have with constraining the σ_8 parameter. The comparison of the six wCDM parameterizations revealed varying degrees of consistency with observational data, underscoring the model's flexibility in addressing unresolved issues. Notably, the inclusion of the latest Planck dataset alongside late-time data provided more insights into these models, while also enabling a direct comparison to the previous Planck data and previous BAO data and identifying the impact of newer datasets as well as the impact that the combinations of the early with late-time data brought to the constraints of the parameters. Therefore, while wCDM shows promise, further work is needed to explore its implications, including experimenting with more popular models that involve the Friedmann equation directly instead of the equation of state, using different datasets and also the possibility of introducing lensing data, to further the understanding of the wCDM models. Future advancements in observational precision and theoretical modelling will undoubtedly shed more light on the H_0 and σ_8 tensions, and would hopefully bring us closer to a better understanding of the Universe. The skills and knowledge gained from studying these wCDM models, such as the data analysis, and computational adjustments that were made to CLASS and MontePython, can be adjusted and applied to other popular models such as quintessence [11, 80].

A

Appendix

In order to test the six wCDM parametrisation models; w_0CDM, CPL, JBP, GE, BA and OSCILL, results needed to be produced using the standard model in cosmology, the ΛCDM model, so that it can be compared to the parameterisation models and conclusions be made. Similar to how results were achieved in the six models, CLASS and MontePython were used for the results of the ΛCDM model.

The values that were obtained are shown in Table S1, Table S2, and Table S3. The tables are split into three sections: sampled parameters, derived parameters and χ^2 statistics. For the first two sections the values of the best-fit, mean, and the 1σ uncertainty are noted for each parameter. In the first table, Table. S1, the sampled parameters section only has the Ω_m parameter. While in the other two tables, the section of sampled parameters includes the parameters, ω_b, ω_{cdm}, $100\theta_s$, $\ln(10^{10}A_s)$, n_s and τ_{reio}. In all of the tables, H_0 is the only derived parameter and the section of χ^2 statistics only includes the value of χ^2_{min}. From this value, the AIC and BIC were calculated and these values were compared to each of the six wCDM models to see if any of the reparametrisation models fit the data better than the standard model.

Three corner plots were made using GetDist so that they can be compared to the corner plots that were obtained for the different wCDM parameterisation models. Fig. A.1 was generated for the analysis of the DESI data set with the older BAO data and to analyse the effect BAO data has on the standard model. The figure shows that when the DESI data was added to the CC + SN+SH0ES it did not affect the value of Ω_m. This was expected as the DESI data does not have constraints on the Ω_m parameter. The older BAO data pushed Ω_m to lower values. On the other hand, when looking at the H_0 parameter, it can be seen that the addition of the DESI data lowered the parameter's value while the older BAO data

Parameters	CC + SN+SH0ES		CC + SN+SH0ES BAO		CC + SN+SH0ES DESI	
	Best-fit	Mean	Best-fit	Mean	Best-fit	Mean
Sampled Parameters						
Ω_m	0.311	0.312 ± 0.016	0.29032	$0.291^{+0.012}_{-0.013}$	0.314	0.314 ± 0.011
Derived Parameters						
H_0	72.38	$72.39^{+0.87}_{-0.90}$	73.35	$73.34^{+0.78}_{-0.76}$	70.49	$70.51^{+0.54}_{-0.56}$
χ^2 **Statistics**						
χ^2_{min}	1310		1329		1334	

Table S1: The ΛCDM values achieved from using only late-time data, one using the older BAO data and the other using the new BAO data.

Parameters	PR3		PR4	
	Best-fit	Mean	Best-fit	Mean
Sampled Parameters				
ω_b	0.02237	0.02236 ± 0.00015	0.02224	$0.02223^{+0.00013}_{-0.00014}$
ω_{cdm}	0.1205	0.1202 ± 0.0014	0.1187	$0.1188^{+0.0012}_{-0.0011}$
$100\theta_s$	1.04220	1.04190 ± 0.00030	1.04180	1.04180 ± 0.00026
$\ln(10^{10} A_s)$	3.045	3.046 ± 0.016	3.039	$3.041^{+0.014}_{-0.015}$
n_s	0.9646	$0.9648^{+0.0044}_{-0.0045}$	0.9679	$0.9673^{+0.0040}_{-0.0042}$
τ_{reio}	0.0567	$0.0546^{+0.0078}_{-0.0081}$	0.0572	$0.0586^{+0.0061}_{-0.0062}$
Derived Parameters				
H_0	67.32	$67.31^{+0.61}_{-0.62}$	67.67	$67.65^{+0.51}_{-0.54}$
σ_8	0.8125	0.8115 ± 0.0076	0.8058	$0.8067^{+0.0065}_{-0.0066}$
χ^2 **Statistics**				
χ^2_{min}	2773		30570	

Table S2: The values of the ΛCDM model obtained from CLASS and MontePython using only early-time data: PR3 and PR4.

Parameters	PR3 CC + SN+SH0ES		PR4 CC + SN+SH0ES	
	Best-fit	Mean	Best-fit	Mean
Sampled Parameters				
ω_b	0.02262	0.02264 ± 0.00014	0.02243	$0.02243^{+0.00011}_{-0.00013}$
ω_{cdm}	0.1170	0.1170 ± 0.0011	0.11682	0.11655 ± 0.00099
$100\theta_s$	1.04220	1.04223 ± 0.00028	1.04200	$1.04205^{+0.00024}_{-0.00022}$
$\ln(10^{10}A_s)$	3.0310	$3.049^{+0.016}_{-0.018}$	3.0402	3.042 ± 0.014
n_s	0.9743	0.9729 ± 0.0041	0.9725	0.9730 ± 0.0036
τ_{reio}	0.0488	$0.0597^{+0.0075}_{-0.0086}$	0.0636	$0.0614^{+0.0059}_{-0.0067}$
Derived Parameters				
H_0	68.79	68.83 ± 0.50	68.60	68.72 ± 0.44
σ_8	0.7967	$0.8037^{+0.0077}_{-0.0079}$	0.8005	$0.8006^{+0.0064}_{-0.0069}$
χ^2 **Statistics**				
χ^2_{min}		4113		31910

Parameters	PR3 CC + SN+SH0ES + DESI		PR4 CC + SN+SH0ES + DESI	
	Best-fit	Mean	Best-fit	Mean
Sampled Parameters				
ω_b	0.02272	0.02266 ± 0.00013	0.02246	0.02242 ± 0.00011
ω_{cdm}	0.11659	$0.11671^{+0.00086}_{-0.00087}$	0.11678	$0.11648^{+0.00082}_{-0.00074}$
$100\theta_s$	1.04200	$1.04220^{+0.00029}_{-0.00028}$	1.04200	$1.04210^{+0.00025}_{-0.00022}$
$\ln(10^{10}A_s)$	3.064	3.052 ± 0.019	3.039	$3.041^{+0.014}_{-0.015}$
n_s	0.9741	$0.9737^{+0.0037}_{-0.0039}$	0.9753	$0.9732^{+0.0035}_{-0.0024}$
τ_{reio}	0.0653	$0.0617^{+0.0093}_{-0.0090}$	0.0601	$0.0607^{+0.0065}_{-0.0066}$
Derived Parameters				
H_0	68.98	$68.94^{+0.38}_{-0.39}$	68.65	$68.75^{+0.34}_{-0.36}$
σ_8	0.8079	$0.8040^{+0.0078}_{-0.0079}$	0.8005	$0.7999^{+0.0064}_{-0.0062}$
χ^2 **Statistics**				
χ^2_{min}		4127		31920

Table S3: The values of the ΛCDM model when using the two Planck data sets: PR3 and PR4, both using CC and SN+SH0ES data, and then adding DESI to them.

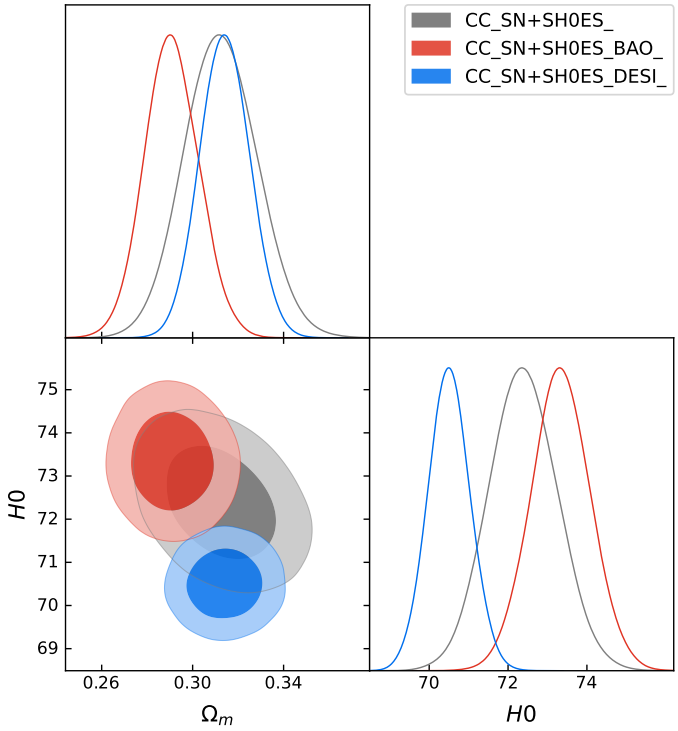

Figure A.1: The graph showing the ΛCDM model when only late-time data was used. The blue corner plot shows the standard model when using DESI BAO data, the red corner plot depicts the model when using the previously released BAO data, and the grey corner plot shows when any BAO data were not used.

had increased the value. Also, it can be noticed that the posteriors are smaller when DESI was used than when only CC and SN+SH0ES were used or when CC and SN+SH0ES were used with the older BAO data. This shows that DESI constrained the data better than the older BAO data showing that DESI is a better BAO data. This trend was expected to be seen when these data combinations were used in the wCDM parameterisation models.

Then, Fig. A.2 was rendered for the comparison of the two early-time data. The figure shows that the PR4 data set has smaller posteriors than when PR3 was used. This indicates that the newer Planck data constrains the standard model better than the previously released Planck data. Since the Planck data sets were tested with the standard model without any late-time data, it will be expected that PR4 will have smaller posteriors even in wCDM parameterisation models. Both CMB data sets constrained all the parameters as anticipated. The PR4 data set produced lower values of ω_b, ω_{cdm} and σ_8 and higher values of n_s, τ_{reio} and H_0

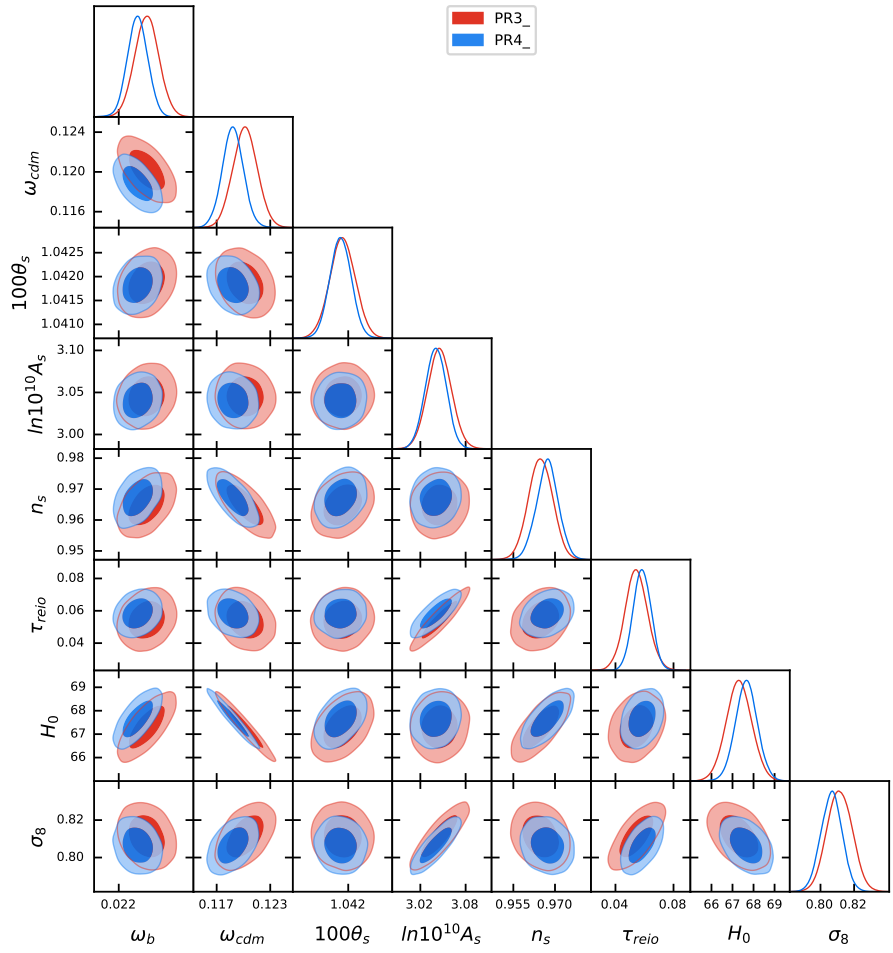

Figure A.2: A graph of the ΛCDM model: one using PR3 data seen in the red corner plot and the other using PR4 seen in the blue corner plot.

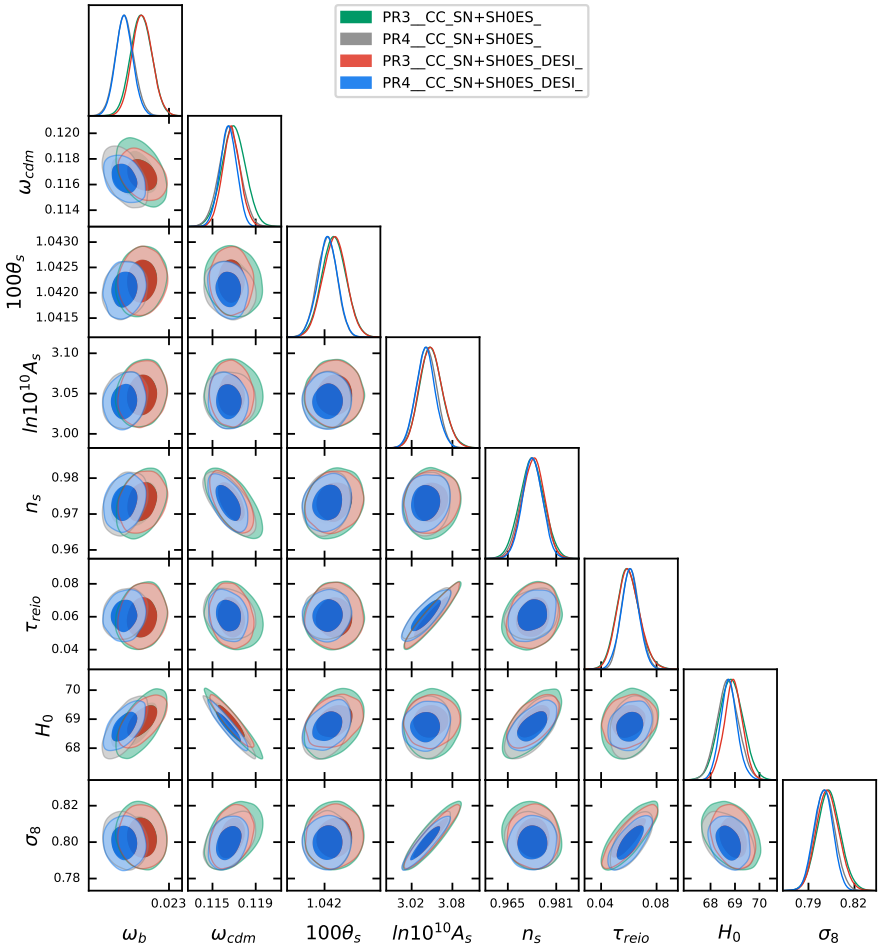

Figure A.3: A graph showing two corner plots of the ΛCDM model when using the two early-time data with CC and SH0ES, and with DESI added to the two data combinations. The green corner plot represents the standard model when PR3 + CC + SN+SH0ES was used, the grey corner plot shows when the PR4 + CC + SN+SH0ES was used, the red corner plot shows when PR3 + CC + SN+SH0ES + DESI was used, while the blue corner plot shows when PR4 + CC + SN+SH0ES + DESI data combination was used.

than the PR3 data set. The two Planck data sets produced similar 1D curves for two parameters, $100\theta_s$ and $\ln(10^{10}A_s)$. The Planck data is expected to affect the parameters in the same way when wCDM parameterisation models are tested.

Then, another graph, Fig. A.3, was generated for the comparison of the two early-time data when the late-time data of CC and SN+SH0ES were added to them, and

then when DESI was added. The addition of the two late-time data sets of CC and SN+SH0ES decreases the difference of ω_{cdm}, τ_{reio} H_0 and n_s between the two Planck data. In fact, the parameter of n_s for the two early-time data seem to overlap each other perfectly. However, the addition of these two late-time data sets increased the differences in the parameters of ω_b and $100\theta_s$. The DESI data did not affect the ω_m, $100\theta_s$, $\ln(10^{10}A_s)$, τ_{reio} and σ_8 parameters, while the four data combinations obtained the same 1D curve for the n_s parameter. For the H_0 parameter it can be seen that the DESI data constrained the standard model better, as tighter 1D curves were achieved with the DESI data. Also, the data combinations that contain DESI data achieved smaller posteriors. The smallest posteriors out of the four data combinations were obtained from PR4 + CC + SN+SH0ES + DESI. Similar behaviour is expected to be seen in the wCDM parameterisation models when these data set combinations are used.

References

[1] T. Abbott et al. The Dark Energy Survey: more than dark energy – an overview. *Mon. Not. Roy. Astron. Soc.*, 460(2):1270–1299, 2016. doi: 10.1093/mnras/stw641.

[2] A. G. Adame et al. DESI 2024 VI: Cosmological Constraints from the Measurements of Baryon Acoustic Oscillations. 4 2024.

[3] P. A. R. Ade et al. Planck 2013 results. I. Overview of products and scientific results. *Astron. Astrophys.*, 571:A1, 2014. doi: 10.1051/0004-6361/201321529.

[4] Arsalan Adil, Andreas Albrecht, and Lloyd Knox. Quintessential cosmological tensions. *Phys. Rev. D*, 107(6):063521, 2023. doi: 10.1103/PhysRevD.107.063521.

[5] N. Aghanim et al. Planck 2018 results. VI. Cosmological parameters. *Astron. Astrophys.*, 641: A6, 2020. doi: 10.1051/0004-6361/201833910. [Erratum: Astron.Astrophys. 652, C4 (2021)].

[6] H Akaike. A new look at the statistical model identification. *IEEE Transactions on Automatic Control*, 19(6):716–723, 1974.

[7] Shadab Alam et al. Completed SDSS-IV extended Baryon Oscillation Spectroscopic Survey: Cosmological implications from two decades of spectroscopic surveys at the Apache Point Observatory. *Phys. Rev. D*, 103(8):083533, 2021. doi: 10.1103/PhysRevD.103.083533.

[8] Jailson S. Alcaniz, Gabriela C. Carvalho, Armando Bernui, Joel C. Carvalho, and Micol Benetti. Measuring baryon acoustic oscillations with angular two-point correlation function. *Fundam. Theor. Phys.*, 187:11–19, 2017. doi: 10.1007/978-3-319-51700-1_2.

[9] Artur Alho, Claes Uggla, and John Wainwright. Perturbations of the Lambda-CDM model in a dynamical systems perspective. *JCAP*, 09:045, 2019. doi: 10.1088/1475-7516/2019/09/045.

[10] S. Amendola, L. Tsujikawa. *Dark Energy*. Cambridge University Press, 2010.

[11] David Andriot. Quintessence: an analytical study, with theoretical and observational applications, 2024. URL `https://arxiv.org/abs/2410.17182`.

[12] Katsuki Aoki, Mohammad Ali Gorji, Takashi Hiramatsu, Shinji Mukohyama, Masroor C. Pookkillath, and Kazufumi Takahashi. CMB spectrum in unified EFT of dark energy: scalar-tensor and vector-tensor theories. 5 2024.

[13] Sebastian Bahamonde, Konstantinos F. Dialektopoulos, Celia Escamilla-Rivera, Gabriel Farrugia, Viktor Gakis, Martin Hendry, Manuel Hohmann, Jackson Levi Said, Jurgen Mifsud, and Eleonora Di Valentino. Teleparallel gravity: from theory to cosmology. *Rept. Prog. Phys.*, 86(2):026901, 2023. doi: 10.1088/1361-6633/ac9cef.

[14] E. M. Barboza, Jr. and J. S. Alcaniz. A parametric model for dark energy. *Phys. Lett. B*, 666: 415–419, 2008. doi: 10.1016/j.physletb.2008.08.012.

[15] V. Barger, Y. Gao, and D. Marfatia. Accelerating cosmologies tested by distance measures. *Phys. Lett. B*, 648:127–132, 2007. doi: 10.1016/j.physletb.2007.03.021.

[16] Atılım Güneş Baydin et al. Efficient Probabilistic Inference in the Quest for Physics Beyond the Standard Model. 7 2018.

[17] C. L. Bennett et al. Nine-Year Wilkinson Microwave Anisotropy Probe (WMAP) Observations: Final Maps and Results. *Astrophys. J. Suppl.*, 208:20, 2013. doi: 10.1088/0067-0049/208/2/20.

[18] Jose Luis Bernal, Licia Verde, and Adam G. Riess. The trouble with H_0. *JCAP*, 10:019, 2016. doi: 10.1088/1475-7516/2016/10/019.

[19] Gianfranco Bertone, Dan Hooper, and Joseph Silk. Particle dark matter: Evidence, candidates and constraints. *Phys. Rept.*, 405:279–390, 2005. doi: 10.1016/j.physrep.2004.08.031.

[20] A. Bhardwaj, V. Ripepi, V. Testa, R. Molinaro, M. Marconi, G. De Somma, E. Trentin, I. Musella, J. Storm, T. Sicignano, and G. Catanzaro. Cepheid metallicity in the leavitt law (c-metall) survey. v. new multiband (grizjhks) cepheid light curves and period-luminosity relations, 2024. URL `https://arxiv.org/abs/2401.03584`.

[21] Shriya Bhatija, Paul-David Zuercher, Jakob Thumm, and Thomas Bohné. Multi-objective causal bayesian optimization, 2025. URL `https://arxiv.org/abs/2502.14755`.

[22] Thejs Brinckmann and Julien Lesgourgues. MontePython 3: boosted MCMC sampler and other features. *Phys. Dark Univ.*, 24:100260, 2019. doi: 10.1016/j.dark.2018.100260.

[23] Dillon Brout et al. The Pantheon+ Analysis: Cosmological Constraints. *Astrophys. J.*, 938 (2):110, 2022. doi: 10.3847/1538-4357/ac8e04.

[24] R. R. Caldwell, Rahul Dave, and Paul J. Steinhardt. Cosmological imprint of an energy component with general equation of state. *Phys. Rev. Lett.*, 80:1582–1585, 1998. doi: 10.1103/PhysRevLett.80.1582.

[25] S. C. Carroll. *An Introduction to General Relativity Spacetime and Geometry*. Addison Wesley, 2004.

[26] Julien Carron, Mark Mirmelstein, and Antony Lewis. CMB lensing from Planck PR4 maps. *JCAP*, 09:039, 2022. doi: 10.1088/1475-7516/2022/09/039.

[27] G. C. Carvalho, A. Bernui, M. Benetti, J. C. Carvalho, and J. S. Alcaniz. Baryon Acoustic Oscillations from the SDSS DR10 galaxies angular correlation function. *Phys. Rev. D*, 93(2): 023530, 2016. doi: 10.1103/PhysRevD.93.023530.

[28] G. C. Carvalho, A. Bernui, M. Benetti, J. C. Carvalho, E. de Carvalho, and J. S. Alcaniz. The transverse baryonic acoustic scale from the SDSS DR11 galaxies. *Astropart. Phys.*, 119: 102432, 2020. doi: 10.1016/j.astropartphys.2020.102432.

[29] Anthony Challinor. CMB anisotropy science: a review. *IAU Symp.*, 288:42, 2013. doi: 10.1017/S1743921312016663.

[30] Clifford Cheung and Grant N. Remmen. Hidden Simplicity of the Gravity Action. *JHEP*, 09:002, 2017. doi: 10.1007/JHEP09(2017)002.

[31] David L Clements. An Introduction to the Planck Mission. *Contemp. Phys.*, 58(4):331–348, 2017. doi: 10.1080/00107514.2017.1362139.

[32] Edmund J. Copeland, M. Sami, and Shinji Tsujikawa. Dynamics of dark energy. *Int. J. Mod. Phys. D*, 15:1753–1936, 2006. doi: 10.1142/S021827180600942X.

[33] Javier de Cruz Perez, Chan-Gyung Park, and Bharat Ratra. Updated observational constraints on spatially flat and nonflat ΛCDM and XCDM cosmological models. *Phys. Rev. D*, 110(2):023506, 2024. doi: 10.1103/PhysRevD.110.023506.

[34] Antonino Del Popolo and Morgan Le Delliou. Small scale problems of the ΛCDM model: a short review. *Galaxies*, 5(1):17, 2017. doi: 10.3390/galaxies5010017.

[35] Eleonora Di Valentino, Olga Mena, Supriya Pan, Luca Visinelli, Weiqiang Yang, Alessandro Melchiorri, David F. Mota, Adam G. Riess, and Joseph Silk. In the realm of the Hubble tension—a review of solutions. *Class. Quant. Grav.*, 38(15):153001, 2021. doi: 10.1088/1361-6382/ac086d.

[36] N. Dimakis, A. Paliathanasis, M. Roumeliotis, and T. Christodoulakis. FLRW solutions in f(Q) theory: The effect of using different connections. *Phys. Rev. D*, 106(4):043509, 2022. doi: 10.1103/PhysRevD.106.043509.

[37] F. Dodelson, S. Schmidt. *Modern cosmology*. London: Academic Press, 2021.

[38] Fuyu Dong, Changbom Park, Sungwook E. Hong, Juhan Kim, Ho Seong Hwang, Hyunbae Park, and Stephen Appleby. Tomographic Alcock–Paczyński Test with Redshift-space Correlation Function: Evidence for the Dark Energy Equation-of-state Parameter $w > -1$. *Astrophys. J.*, 953(1):98, 2023. doi: 10.3847/1538-4357/acd185.

[39] Luke Duttweiler, Jonathan Klus, Brent Coull, and Sally W. Thurston. The traceplot thickens: Mcmc diagnostics for non-euclidean spaces, 2024. URL `https://arxiv.org/abs/2408.15392`.

[40] Cora Dvorkin, Siddharth Mishra-Sharma, Brian Nord, V. Ashley Villar, Camille Avestruz, Keith Bechtol, Aleksandra Ćiprijanović, Andrew J. Connolly, Lehman H. Garrison, Gautham Narayan, and Francisco Villaescusa-Navarro. Machine learning and cosmology, 2022. URL `https://arxiv.org/abs/2203.08056`.

[41] George Efstathiou. Challenges to the Lambda CDM Cosmology. 6 2024.

[42] Celia Escamilla-Rivera and Antonio Nájera. Dynamical dark energy models in the light of gravitational-wave transient catalogues. *JCAP*, 03(03):060, 2022. doi: 10.1088/1475-7516/2022/03/060.

[43] Arianna Favale, Adrià Gómez-Valent, and Marina Migliaccio. Cosmic chronometers to calibrate the ladders and measure the curvature of the Universe. A model-independent study. *Mon. Not. Roy. Astron. Soc.*, 523(3):3406–3422, 2023. doi: 10.1093/mnras/stad1621.

[44] Elena Fernández-García, Juan E. Betancort-Rijo, Francisco Prada, Tomoaki Ishiyama, and Anatoly Klypin. Constraining cosmological parameters using void statistics from the SDSS survey. 6 2024.

[45] James M. Flegal and Rebecca P. Kurtz-Garcia. Implementing mcmc: Multivariate estimation with confidence, 2024. URL `https://arxiv.org/abs/2408.15396`.

[46] Guillermo Franco Abellán, Guadalupe Cañas Herrera, Matteo Martinelli, Oleg Savchenko, Davide Sciotti, and Christoph Weniger. Fast likelihood-free inference in the LSS Stage IV era. 3 2024.

[47] Wendy L. Freedman. Measurements of the hubble constant: Tensions in perspective*. *The Astrophysical Journal*, 919(1):16, September 2021. ISSN 1538-4357. doi: 10.3847/1538-4357/ac0e95.

[48] Wendy L. Freedman et al. The Carnegie-Chicago Hubble Program. VIII. An Independent Determination of the Hubble Constant Based on the Tip of the Red Giant Branch. *Astrophys. J.*, 882:34, 2019. doi: 10.3847/1538-4357/ab2f73.

[49] Raghuveer Garani, Michele Redi, and Andrea Tesi. Particle production from inhomogeneities: general metric perturbations. 2 2025.

[50] Basundhara Ghosh and Carlos Bengaly. Consistency tests between SDSS and DESI BAO measurements. 8 2024.

[51] Giovanni Gallavotti. *Perturbation Theory*. Springer, 2022.

[52] Elena Giusarma, Roland de Putter, Shirley Ho, and Olga Mena. Constraints on neutrino masses from Planck and Galaxy Clustering data. *Phys. Rev. D*, 88(6):063515, 2013. doi: 10.1103/PhysRevD.88.063515.

[53] Balakrishna S. Haridasu, Vladimir V. Luković, and Nicola Vittorio. Isotropic vs. Anisotropic components of BAO data: a tool for model selection. *JCAP*, 05:033, 2018. doi: 10.1088/1475-7516/2018/05/033.

[54] Dhiraj Kumar Hazra, Benjamin Beringue, Josquin Errard, Arman Shafieloo, and George F. Smoot. Exploring the discrepancy between Planck PR3 and ACT DR4. *JCAP*, 12:038, 2024. doi: 10.1088/1475-7516/2024/12/038.

[55] Eistathiom G. Hobson, M. P. and A. N. Lasenby. *General Relativity and introduction for physicists*.

[56] Alejandro Ibarra, Patrick Strobl, and Takashi Toma. Neutrino masses from Planck-scale lepton number breaking. *Phys. Rev. Lett.*, 122(8):081803, 2019. doi: 10.1103/PhysRevLett.122.081803.

[57] J. Jasche and F. S. Kitaura. Fast Hamiltonian sampling for large scale structure inference. *Mon. Not. Roy. Astron. Soc.*, 407:29, 2010. doi: 10.1111/j.1365-2966.2010.16897.x.

[58] J. Jasche, F. S. Kitaura, C. Li, and T. A. Ensslin. Bayesian non-linear large scale structure inference of the Sloan Digital Sky Survey data release 7. *Mon. Not. Roy. Astron. Soc.*, 409:355, 2010. doi: 10.1111/j.1365-2966.2010.17313.x.

[59] Donghui Jeong and Fabian Schmidt. Cosmic Clocks. *Phys. Rev. D*, 89(4):043519, 2014. doi: 10.1103/PhysRevD.89.043519.

[60] Claus Kiefer and Hermann Nicolai. The impact of Friedmann's work on cosmology. 5 2021.

[61] Ofer Lahav. Deep machine learning in cosmology: Evolution or revolution?, 2023. URL `https://arxiv.org/abs/2302.04324`.

[62] Julien Lesgourgues. The Cosmic Linear Anisotropy Solving System (CLASS) I: Overview. 4 2011.

[63] Julien Lesgourgues. The Cosmic Linear Anisotropy Solving System (CLASS) III: Comparision with CAMB for LambdaCDM. 4 2011.

[64] Julien Lesgourgues and Thomas Tram. The Cosmic Linear Anisotropy Solving System (CLASS) IV: efficient implementation of non-cold relics. *JCAP*, 09:032, 2011. doi: 10.1088/1475-7516/2011/09/032.

[65] Antony Lewis. GetDist: a Python package for analysing Monte Carlo samples. 10 2019.

[66] Sebastian Linden and Jean-Marc Virey. A test of the CPL parameterization for rapid dark energy equation of state transitions. *Phys. Rev. D*, 78:023526, 2008. doi: 10.1103/PhysRevD.78.023526.

[67] Anto I. Lonappan, Sumit Kumar, Ruchika, Bikash R. Dinda, and Anjan A. Sen. Bayesian evidences for dark energy models in light of current observational data. *Phys. Rev. D*, 97(4):043524, 2018. doi: 10.1103/PhysRevD.97.043524.

[68] Thomas J. Loredo and Robert L. Wolpert. Bayesian inference: More than bayes's theorem, 2024. URL `https://arxiv.org/abs/2406.18905`.

[69] Chung-Pei Ma and Edmund Bertschinger. Cosmological perturbation theory in the synchronous and conformal Newtonian gauges. *Astrophys. J.*, 455:7–25, 1995. doi: 10.1086/176550.

[70] Joao Magueijo and John Webb. John D Barrow (1952–2020). *Astron. Geophys.*, 61(6):6.11–6.12, 2020. doi: 10.1093/astrogeo/ataa081.

[71] Michele Moresco, Lucia Pozzetti, Andrea Cimatti, Raul Jimenez, Claudia Maraston, Licia Verde, Daniel Thomas, Annalisa Citro, Rita Tojeiro, and David Wilkinson. A 6% measurement of the Hubble parameter at $z \sim 0.45$: direct evidence of the epoch of cosmic re-acceleration. *JCAP*, 05:014, 2016. doi: 10.1088/1475-7516/2016/05/014.

[72] Kana Moriwaki, Takahiro Nishimichi, and Naoki Yoshida. Machine learning for observational cosmology. *Reports on Progress in Physics*, 86(7):076901, May 2023. ISSN 1361-6633. doi: 10.1088/1361-6633/acd2ea.

[73] David F. Mota and John D. Barrow. Local and global variations of the fine structure constant. *Mon. Not. Roy. Astron. Soc.*, 349:291, 2004. doi: 10.1111/j.1365-2966.2004.07505.x.

[74] Savvas Nesseris. The Effective Fluid approach for Modified Gravity and its applications. *Universe*, 9:2022, 2023. doi: 10.3390/universe9010013.

[75] Shulei Ni, Yichao Li, and Xin Zhang. CMB delensing with deep learning. 10 2023.

[76] Victor Nijimbere. Evaluation of some non-elementary integrals involving sine, cosine, exponential and logarithmic integrals: Part i. *Ural mathematical journal*, 4(1):24–42, 2018. ISSN 2414-3952. doi: 10.15826/umj.2018.1.003.

[77] Shin'ichi Nojiri and Sergei D. Odintsov. The Oscillating dark energy: Future singularity and coincidence problem. *Phys. Lett. B*, 637:139–148, 2006. doi: 10.1016/j.physletb.2006.04.026.

[78] Supriya Pan, Emmanuel N. Saridakis, and Weiqiang Yang. Observational Constraints on Oscillating Dark-Energy Parametrizations. *Phys. Rev. D*, 98(6):063510, 2018. doi: 10.1103/PhysRevD.98.063510.

[79] Chan-Gyung Park and Bharat Ratra. Observational constraints on the tilted spatially-flat and the untilted nonflat ϕCDM dynamical dark energy inflation models. *Astrophys. J.*, 868 (2):83, 2018. doi: 10.3847/1538-4357/aae82d.

[80] Guillaume Payeur, Evan McDonough, and Robert Brandenberger. Do observations prefer thawing quintessence?, 2024. URL `https://arxiv.org/abs/2411.13637`.

[81] Davide Pedrotti, Jun-Qian Jiang, Luis A. Escamilla, Simony Santos da Costa, and Sunny Vagnozzi. Multidimensionality of the hubble tension: the roles of ω_m and ω_c, 2024. URL `https://arxiv.org/abs/2408.04530`.

[82] Leandros Perivolaropoulos and Foteini Skara. Challenges for ΛCDM: An update. *New Astron. Rev.*, 95:101659, 2022. doi: 10.1016/j.newar.2022.101659.

[83] S. Perlmutter et al. Measurements of Ω and Λ from 42 high redshift supernovae. *Astrophys. J.*, 517:565–586, 1999. doi: 10.1086/307221.

[84] Vivian Poulin, José Luis Bernal, Ely D. Kovetz, and Marc Kamionkowski. Sigma-8 tension is a drag. *Phys. Rev. D*, 107(12):123538, 2023. doi: 10.1103/PhysRevD.107.123538.

[85] Vivian Poulin, Tristan L. Smith, and Tanvi Karwal. The ups and downs of early dark energy solutions to the hubble tension: a review of models, hints and constraints circa 2023, 2023. URL `https://arxiv.org/abs/2302.09032`.

[86] S. Pourojaghi, M. Malekjani, and Z. Davari. Cosmological constraints on dark energy parametrizations after DESI 2024: Persistent deviation from standard ΛCDM cosmology. 7 2024.

[87] Frank J. Qu et al. The Atacama Cosmology Telescope: A Measurement of the DR6 CMB Lensing Power Spectrum and Its Implications for Structure Growth. *Astrophys. J.*, 962(2): 112, 2024. doi: 10.3847/1538-4357/acfe06.

[88] Robert Reischke et al. KiDS-Legacy: Covariance validation and the unified OneCovariance framework for projected large-scale structure observables. 10 2024.

[89] Adam G. Riess et al. Observational evidence from supernovae for an accelerating universe and a cosmological constant. *Astron. J.*, 116:1009–1038, 1998. doi: 10.1086/300499.

[90] Adam G. Riess et al. A Comprehensive Measurement of the Local Value of the Hubble Constant with 1 km s^1 Mpc^1 Uncertainty from the Hubble Space Telescope and the SH0ES Team. *Astrophys. J. Lett.*, 934(1):L7, 2022. doi: 10.3847/2041-8213/ac5c5b.

[91] Christian P. Robert. The metropolis-hastings algorithm, 2016. URL `https://arxiv.org/abs/1504.01896`.

[92] David Rubin, Greg Aldering, Marc Betoule, Andy Fruchter, Xiaosheng Huang, Alex G. Kim, Chris Lidman, Eric Linder, Saul Perlmutter, Pilar Ruiz-Lapuente, and Nao Suzuki. Union through unity: Cosmology with 2,000 sne using a unified bayesian framework, 2024. URL `https://arxiv.org/abs/2311.12098`.

[93] Ehsan Sadri. An analogy between four parametrizations of the dark energy equation of state onto Physical DE Models. 1 2017.

[94] Robert J. Scherrer. Mapping the Chevallier-Polarski-Linder parametrization onto Physical Dark Energy Models. *Phys. Rev. D*, 92(4):043001, 2015. doi: 10.1103/PhysRevD.92.043001.

[95] Tiziano Schiavone. *Large-scale structure of the Universe in General Relativity and beyond*. PhD thesis, Pisa U., 9 2023.

[96] Jürgen Schmidhuber. Deep learning in neural networks: An overview. *Neural Networks*, 61: 85–117, January 2015. ISSN 0893-6080. doi: 10.1016/j.neunet.2014.09.003.

[97] G. Schwarz. Estimating the Dimension of a Model Ann. Statist . *The Annals of Statistics*, 6 (2):461–464, 1978.

[98] Nils Schöneberg, Guillermo Franco Abellán, Andrea Pérez Sánchez, Samuel J. Witte, Vivian Poulin, and Julien Lesgourgues. The h0 olympics: A fair ranking of proposed models. *Physics Reports*, 984:1–55, October 2022. ISSN 0370-1573. doi: 10.1016/j.physrep.2022.07.001.

[99] Dan Scolnic et al. The Pantheon+ Analysis: The Full Data Set and Light-curve Release. *Astrophys. J.*, 938(2):113, 2022. doi: 10.3847/1538-4357/ac8b7a.

[100] E. Sellentin, A. Loureiro, L. Whiteway, J. S. Lafaurie, S. T. Balan, M. Olamaie, A. H. Jaffe, and A. F. Heavens. Almanac: MCMC-based signal extraction of power spectra and maps on the sphere. 5 2023. doi: 10.21105/astro.2305.16134.

[101] German S. Sharov and Vasily E. Myachin. Modified Equations of State for Dark Energy and Observational Limitations. *Universe*, 8(4):201, 2022. doi: 10.3390/universe8040201.

[102] Maria Shubina. Some exact solutions of Friedmann cosmological equation. *Annals Phys.*, 462:169613, 2024. doi: 10.1016/j.aop.2024.169613.

[103] Ramanpreet Singh, Athul C. N, and H. K. Jassal. A Critical Reanalysis of Supernova Type Ia Data. 1 2025.

[104] Tristan L. Smith, Vivian Poulin, José Luis Bernal, Kimberly K. Boddy, Marc Kamionkowski, and Riccardo Murgia. Early dark energy is not excluded by current large-scale structure data. *Phys. Rev. D*, 103:123542, Jun 2021. doi: 10.1103/PhysRevD.103.123542.

[105] George F. Smoot. COBE observations and results. *AIP Conf. Proc.*, 476(1):1–10, 1999. doi: 10.1063/1.59326.

[106] Camilla T. G. Sørensen, Steen Hannestad, Andreas Nygaard, and Thomas Tram. Calculating Bayesian evidence for inflationary models using CONNECT. 6 2024.

[107] Joshua S. Speagle. A Conceptual Introduction to Markov Chain Monte Carlo Methods. 9 2019.

[108] Jesús Torrado and Antony Lewis. Cobaya: code for bayesian analysis of hierarchical physical models. *Journal of Cosmology and Astroparticle Physics*, 2021(05):057, May 2021. ISSN 1475-7516. doi: 10.1088/1475-7516/2021/05/057.

[109] Cynthia Trendafilova, Selim C. Hotinli, and Joel Meyers. Improving Constraints on Inflation with CMB Delensing. 12 2023.

[110] M. Tristram et al. Cosmological parameters derived from the final Planck data release (PR4). *Astron. Astrophys.*, 682:A37, 2024. doi: 10.1051/0004-6361/202348015.

[111] Jussi Väliviita and Elina Palmgren. Distinguishing interacting dark energy from wCDM with CMB, lensing, and baryon acoustic oscillation data. *JCAP*, 07:015, 2015. doi: 10.1088/1475-7516/2015/07/015.

[112] Dootika Vats and Christina Knudson. Revisiting the gelman-rubin diagnostic, 2020. URL `https://arxiv.org/abs/1812.09384`.

[113] Théo Vincent, Tim Faust, Yogesh Tripathi, Jan Peters, and Carlo D'Eramo. Eau de q-network: Adaptive distillation of neural networks in deep reinforcement learning, 2025. URL `https://arxiv.org/abs/2503.01437`.

[114] W. T. Vetterling B. P. Flannery W. H. Press, S. A. Teukolsky. *Numerical Recipes in C*. CAMBRIDGE UNIVERSITY PRESS, 2002.

[115] Yue Wang, Wenhui Chang, Tongwei Deng, Yanzhen Zou, and Bing Xie. Decomposing god header file via multi-view graph clustering, 2024. URL `https://arxiv.org/abs/2406.16487`.

[116] Liliya L. R. Williams. Measuring the Hubble constant H0 from gravitational lensing. In *16th Marcel Grossmann Meeting on Recent Developments in Theoretical and Experimental General Relativity, Astrophysics and Relativistic Field Theories*, 2023. doi: 10.1142/9789811269776_0132.

[117] Kenneth C. Wong et al. H0LiCOW – XIII. A 2.4 per cent measurement of H0 from lensed quasars: 5.3σ tension between early- and late-Universe probes. *Mon. Not. Roy. Astron. Soc.*, 498(1):1420–1439, 2020. doi: 10.1093/mnras/stz3094.

[118] Kenneth C. Wong et al. TDCOSMO. XVII. Measurement of the Hubble Constant from the Lensed Quasar WGD 2038−4008. 6 2024.

[119] Yvonne Y. Y. Wong. Neutrino mass in cosmology: status and prospects. *Ann. Rev. Nucl. Part. Sci.*, 61:69–98, 2011. doi: 10.1146/annurev-nucl-102010-130252.

[120] Lixin Xu. Unified Dark Fluid with Constant Adiabatic Sound Speed: Including Entropic Perturbations. *Phys. Rev. D*, 87(4):043503, 2013. doi: 10.1103/PhysRevD.87.043503.

[121] Tengpeng Xu, Yun Chen, Lixin Xu, and Shuo Cao. Comparing the scalar-field dark energy models with recent observations. *Phys. Dark Univ.*, 36:101023, 2022. doi: 10.1016/j.dark.2022.101023.

[122] Yue-Yao Xu and Xin Zhang. Comparison of dark energy models after planck 2015. *The European Physical Journal C*, 76(11), October 2016. ISSN 1434-6052. doi: 10.1140/epjc/s10052-016-4446-5.

[123] Weiqiang Yang, Eleonora Di Valentino, Supriya Pan, Yabo Wu, and Jianbo Lu. Dynamical dark energy after Planck CMB final release and H_0 tension. *Mon. Not. Roy. Astron. Soc.*, 501 (4):5845–5858, 2021. doi: 10.1093/mnras/staa3914.

[124] Dehao Zhang, Shuai Wang, Yichen Xiao, Wenjie Wei, Yimeng Shan, Malu Zhang, and Yang Yang. Memory-free and parallel computation for quantized spiking neural networks, 2025. URL `https://arxiv.org/abs/2503.00040`.

[125] Jing-Fei Zhang, Li-Yang Gao, Dong-Ze He, and Xin Zhang. Improving cosmological parameter estimation with the future 21 cm observation from ska. *Physics Letters B*, 799:135064, December 2019. ISSN 0370-2693. doi: 10.1016/j.physletb.2019.135064.

[126] Gong-Bo Zhao, Jun-Qing Xia, Hong Li, Charling Tao, Jean-Marc Virey, Zong-Hong Zhu, and Xinmin Zhang. Probing for dynamics of dark energy and curvature of universe with latest cosmological observations. *Phys. Lett. B*, 648:8–13, 2007. doi: 10.1016/j.physletb.2007.02.070.